RICE UNIVERSITY

Carbon Sequestration through Biochar Soil Amendment: Experimental studies and mathematical modeling

by

Hao Sun

A THESIS SUBMITTED
IN PARTIAL FULLFILMENT OF THE
REQUIREMENTS FOR THE DEGREE

Doctor of Philosophy

APPROVED, THESIS COMMITTEE:

Kyriacos Zygourakis
A. J. Hartsook Professor and Department Chair
Chemical and Biomolecular Engineering

Caroline A. Masiello
Assistant Professor
Earth Science

Walter G. Chapman
William W. Akers Professor
Chemical and Biomolecular Engineering

William C. Hockaday
Assistant Professor
Geology, Baylor University

HOUSTON, TEXAS
MAY 2012

RICE UNIVERSITY

Carbon Sequestration through Biochar Soil Amendment: Experimental studies and mathematical modeling

by

Hao Sun

A THESIS SUBMITTED
IN PARTIAL FULLFILMENT OF THE
REQUIREMENTS FOR THE DEGREE

Doctor of Philosophy

APPROVED, THESIS COMMITTEE:

_____
Kyriacos Zygourakis
A. J. Hartsook Professor and Department Chair
Chemical and Biomolecular Engineering

_____
Caroline A. Masiello
Assistant Professor
Earth Science

_____
Walter G. Chapman
William W. Akers Professor
Chemical and Biomolecular Engineering

_____
William C. Hockaday
Assistant Professor
Geology, Baylor University

HOUSTON, TEXAS
MAY 2012

Abstract

Intentional amendment of soil with charcoal (called biochar) is a promising new approach to sequester atmospheric carbon dioxide and increase soil fertility. However, the environmental properties of biochars can vary with production conditions, making it challenging to engineer biochars that are simultaneously optimized for carbon sequestration, nutrient storage, and water-holding capacity.

For this reason, I have undertaken a systematic study to (a) determine the pyrolysis conditions that lead to biochars with desired chemical and physical properties, and (b) find how these properties affect the water-holding capacity and nutrient adsorption in biochar-soil mixtures.

First, a library of biochars was produced in a custom-built pyrolysis reactor under precisely controlled conditions. The chemical and physical structures of the produced biochars were characterized with various analytical techniques including ^{13}C NMR, XPS, EA and BET pore surface analysis. My results suggest that the chemical composition and pore structure of biochars are determined not just by the maximum heat treatment temperature, but also by several other factors that include the pyrolysis heating rate, treatment time at the maximum temperature and particle size.

I also tested a new approach that combines thermogravimetric reactivity measurements, diffusion-reaction theory and structural models to achieve a better characterization of the complicated multi-scale pore structure of biochars. The structural models treat biochars as porous solids having micro- and macropores of different shapes and exhibiting widely ranging pore-size distributions. Simulations results are then compared to experimental data to identify

the presence of ordered or random pore networks and test their size distributions and connectivity.

I then developed a multi-solid one-dimensional model that can use experimentally determined biochar properties to predict their field performance in beds packed with soil/biochar mixtures. The model used a system of coupled partial differential equations to describe the dynamic adsorption/elution of ammonium nitrate, a model fertilizer, in columns packed with biochar/soil mixtures and perfused with aqueous solutions of the fertilizer. The PDE system was solved using orthogonal collocation on finite elements. My chromatographic model accounted for all the important processes occurring in this system, including external mass transfer between the fluid phase and the solid particles, as well as intraparticle diffusion and adsorption of the solute on the pore surface area of the sorbents. To our knowledge, this is the first chromatographic model that accounted explicitly for the presence of two solid phases with widely different pore structures and adsorption capacities. A systematic parametric study was carried out to determine the importance of each system parameter. The adsorption equilibrium parameters and the intraparticle effective diffusivity of ammonium had the most significant effect on environmental performance.

To complete the theoretical analysis, I also developed a model to describe the saturation and drainage of water from the packed column. The model accounted for all the important processes occurring in this system: (a) water exchange between the interstitial pore region and two different smaller pore regions and (b) water flow inside the larger pore region and the two different smaller pore regions. The transient mass balances led to a system of partial differential equations that was solved using block centered finite difference.

Acknowledgments

I would like to thank Dr. Kyriacos Zygourakis and Dr. Caroline A. Masiello for their guidance and support. I appreciate their rigorous requirement, parent-like guidance and the freedom they offer to me to try my new ideas. I appreciate this thesis project they offered to me which shapes me up in different aspects, such as: reactor design and building up, experiments and mathematical models. I would like to thank Dr. William C. Hockaday for processing the NMR data, guiding my research and serving on my committee. I would also like to thank Dr. Walter G. Chapman for serving on my committee.

I want to appreciate Dr. George J. Hirasaki, Dr. Clarence A. Miller and Dr. Beatrice Riviere for their splendid classes, which broaden my knowledge of fluid mechanics, mass/heat transfer and numerical solutions to PDEs and help me to start my thesis work at a higher level.

I also want to appreciate my good friends Xin Wang, Jose Lopez-Salinas, Yue Huang, Changhao Wang, Bradley Lambeth, Yu Pu, Yao Zhao and Chaojun Huang in Rice University. All of you make the past five years an invaluable memory in my deep heart.

I also thank Richard (Dick) Chronister for helping with the construction and maintenance of the reactor used for this study, Dr. M.S.Wong for graciously providing access to his gas adsorption analyzer, and Dr. Larry Alemany and Dr. Bo Chen for their assistance with NMR and XPS measurements.

I also gratefully acknowledge the financial support from the Rice Shell Center for Sustainability, the National Science Foundation (EAR 0911685), and the U.S. Department of Energy (SUN grant No. DE-FG36-08GO88073).

Finally, I deeply appreciate my family members for their constant support, encouragement, understanding and patience.

Table of Contents

List of Figures

Figure 3.8 Mass of unreacted residues/intermediate solid/ volatiles/ biochar for the two runs of Figure 3.7.....56

Figure 3.9 ^{13}C direct polarization spectra (DP – solid line) and direct polarization with dipolar dephasing spectra (DP+DD – dash line) for an apple wood biochar. The sample was ground to 1.5 mm, heated at 0.1°C/s to 600°C and held at 600°C for 1 hour.. 61

Figure 3.10 ^{13}C direct polarization spectra (DP – solid line) and direct polarization with dipolar dephasing spectra (DP+DD – dash line) for a corn stover biochar. The sample was ground to 1.5 mm, heated at 0.1°C/s to 600°C and held at 600°C for 1 hour.. 62

List of Tables

CHAPTER 1

INTRODUCTION

1.1 General

Global warming and the resulting climate changes are perhaps the most important technological challenges facing the modern world. The most important anthropogenic driver of the greenhouse effect is CO_2 released through burning of fossil fuels. As shown in Figure 1.1, there has been a 33% rise in CO_2 atmospheric concentration since 1880, when pre-industrial values were 290 ppm to 385 ppm in 2008, which has caused an average increase of 1.0 °C in land and ocean temperature compared to 1880 values [1].

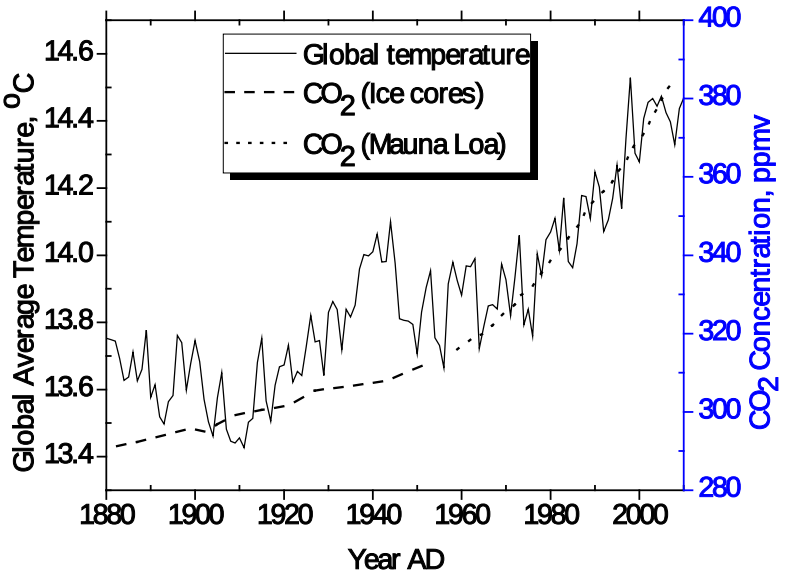

Figure 1.1 Rising Levels of Atmospheric CO_2 [1]

Successful mitigation of atmospheric CO_2 will require not one, but many different approaches to

carbon sequestration[2]. Traditional views of terrestrial sequestration involve reforestation, stopping deforestation and improved agricultural practices like conservation tillage and CH_4 and N_2O management. These approaches are stop gap measures, however, because the residence time of carbon in these pools is on the order of 5-50 years [3]. Plants grow by absorbing CO_2 (sequestering carbon) from the atmosphere to photosynthesize sugars and form biomass. However, most of the CO_2 fixed by plants (99%) returns to the atmosphere through respiration and decomposition (degradation) on the time scale of a human lifetime, making the whole process carbon neutral. Similarly, soil C sequestration by conservation tillage adds C to the fastest-cycling soil carbon pool, creating a relatively small stop-gap C sink which cannot be relied on for long-term storage[4]. While forest expansion and conservation tillage have hydrologic and ecologic co-benefits that last much longer than 50 years, they cannot solve the CO_2 problem by themselves[5]. Doubts also exist about the feasibility of carbon sequestration in oceans, oil or natural gas wells or deep aquifers. CO_2 sequestration via deep aquifer injection may become part of a long-term CO_2 mitigation portfolio. However, there aren't enough deep oil and natural gas wells in the US to hold all the CO_2 we will produce in the next 10-15 years. A lot of work remains to be done before any large-scale application of this approach [3].

Whatever our final CO_2 mitigation portfolio becomes, it is clear that effective carbon sequestration must be based on sustainable processes that provide safe, stable carbon sinks with enough capacity to sequester a substantial fraction of anthropogenic CO_2 emissions. In contrast to these above-mentioned approaches, one promising approach is biochar soil amendment, the intentional addition of charcoal to soil [4, 5]. Using both regulatory and market approaches at countrial and global levels, carbon sequestration through biochar production and soil amendment can be deployed widely, rapidly and cheaply within decades[5].

To create a longer-term carbon sink, biomass can be pyrolyzed to turn a portion of the carbon into a highly recalcitrant charcoal. When this charcoal is produced for intensional soil amendment, it is called biochar. Biochar added to soil is stable for 500 to 2000 years [6, 7], creating a carbon sink (Figure 1.2).

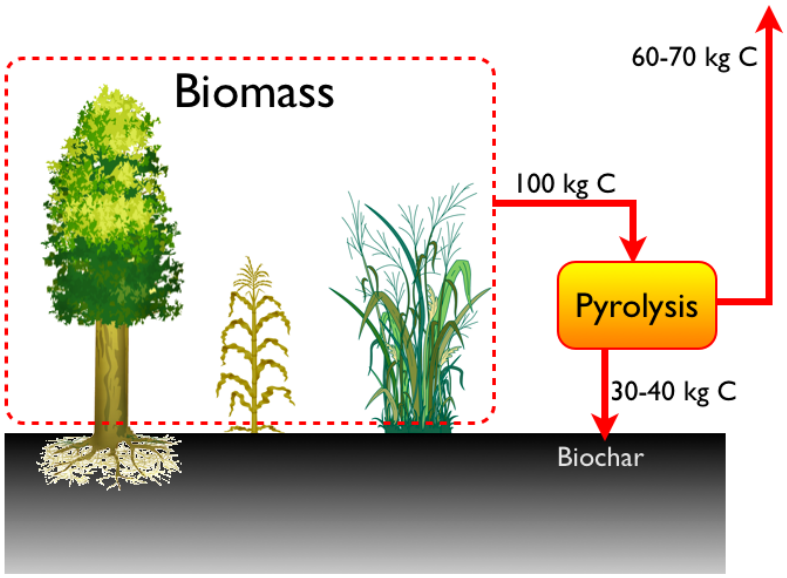

Figure 1.2 – Biochar for Carbon Sequestration

Generated and deposited by wildfires, charcoal is already an important component of most soils and currently makes up between 1-15% of the total organic carbon in soil [8]. Soil carbon storage by biochar soil amendment can add carbon to extremely stable carbon reservoirs. This type of soil management was practiced by Amerindians in the pre-Columbian Amazon[4]. Evidence suggests that the carbon sequestration effect of Amerindian biochar addition to soils has persisted for at least 500 years[9]. A class of Amazonian soils called Dark Earths or "terra preta" contain 70 times more carbon than the surrounding soils[10]. These soils most likely resulted from pre-Columbian Amerindian disposal of charcoal and fish remains by soil burial[11].

A recent study by Molina et al.[5] placed sequestration by biochar high on the list of strategies for reducing carbon emissions, because it can be deployed rapidly and relatively cheaply. A detailed analysis by Woolf et al.[12] estimated that if biochar is deployed globally as a carbon sequestration strategy, its maximum sequestration potential might be as large as 1.8 Gt of carbon per year and up to 130 Gt over a century. Thus, biochar has the potential to mitigate a significant fraction of the 15 Gt/yr of total global anthropogenic emissions[13].

The direct addition of biochar to soils increases the size of the stable soil carbon pool. Biochar also provides indirect benefits: the addition of biochar helps soil retain nutrients, creating a positive feedback on carbon sequestration. Biochar added to soil behaves as a sponge, soaking up other forms of organic matter as well as water and nutrients [14]. Biochar generally increases the water holding capacity of soils, improving the ability of plants to survive under drought conditions[15]. Biochar also increases the cation exchange capacity (CEC) of soils. CEC describes a soil's ability to hold onto positively charged particles via weak chemical bonds, including important plant nutrients like NH_4^+, Ca^{2+}, and Mg^{2+}[14]. High CEC soils transform freshly input nutrients into slow-release fertilizer, preventing their washout into watersheds. Two processes are assumed to happen: (1) nutrients are adsorbed on the surface of amorphous carbonized materials; (2) slow biological oxidation produces carboxylic units on the edges of the condensed aromatic backbone of the biochar which increases the CEC [14]. These properties act in concert to create a fertility/carbon sequestration positive feedback loop: more biochar means more water and nutrients, which increases the organic matter input to the soil, which can then be absorbed onto the biochar surface or stored in deeper soil carbon reservoirs [16].

The fertility of biochar-amended soils is greatly improved [14]. For example, recent field trials in the central Amazon (near Manaus, Brazil) [17] and Alfisol soil (Australia) [18, 19], soil

biochar amendments improved the plant available N from fertilizer [20]. Higher cation exchange capacities, organic carbon, and microbial activity, as well as higher retention of applied fertilizer, were observed for higher biochar application, leading to higher crop yields [18, 19, 21]. Biochar has also been effective in significantly decreasing Cu, As and Cd in pore water and reducing phytotoxicity in contaminated soil [22].

However, not all biochars are identical, and while the majority of biochar studies report positive responses, unintended outcomes have also been observed. For example, some biochars stimulated the short-term release of CO_2 from soils [23-25], while other biochars had unintented effects on soil biota [26, 27]. In some cases, biochar has been documented to change the ecosystem dissolved organic carbon flux[28]. In other cases, overall crop yield responses to biochar, either positive or negative, were smaller than expected based on previous studies [29]. All these outcomes are driven in part by the physical and chemical structure of biochars that vary widely with production conditions, making it important to understand how to engineer specific characteristics into biochars. In view of the considerable environmental potential of biochar soil amendment, I made fundamental measurements and conducted modeling studies to better understand the engineerable properties of biochar.

This chapter is divided into two sections. The first section will review and pose problems in pyrolysis and biochar characterization, characterization the pore structure of biochar and biochar adsorption. The second section will highlight my objectives and significance of this study.

1.2 Pyrolysis and biochar characterization

Biochar is the solid residue of biomass pyrolysis or incomplete combustion and differs from charcoal only in that biochar is produced for intentional soil amendment[4]. The reaction mechanisms of biomass pyrolysis are complex but proceed in the following three main steps:

$$\text{Biomass} \rightarrow \text{Water} + \text{Unreacted residue} \quad (1.1)$$

$$\text{Unreacted residue} \rightarrow (\text{Volatile+Gases})_1 + (\text{Char})_1 \quad (1.2)$$

$$(\text{Char})_1 \rightarrow (\text{Volatile+Gases})_2 + (\text{Char})_2 \quad (1.3)$$

In the initial step moisture and some volatiles are lost (equation 1.1). Biochar is produced mainly in the second step (equation 1.2). This is an endothermic step, releasing volatiles, including tars and gases [30]. This fast step (equation 1.2) is followed by a slower step (equation 1.3) that involves chemical rearrangement of the biochar. During the third step, the biochar decomposes at a very slow rate, forming a carbon-rich solid residue[31]. This is an exothermic step, releasing volatiles, gases and heat[30]. This secondary charring (equation 1.3) makes the char less reactive[32].

Biochar is richer in carbon than its parent biomass[33]. The gas produced during the pyrolysis process (obtained with a yield around 30–40%) is mostly composed of N_2 and CO_2 [34]. Although the heating value of the gas is quite low, pyrolysis gas, in general, can be burned to provide process heat[35]. The chars generated from pyrolysis have a higher heating value between 4600 and 6000 kcal/kg and low sulfur content can be used to produce briquettes[34] or for soil amendment. In addition to energy, certain valuable co-products can be obtained, including wood preservative, food flavoring, adhesives, or specific chemical compounds[30]. Various pyrolysis processes such as fast pyrolysis, slow pyrolysis, high temperature and low temperature pyrolysis can be used.

Depending on the heating rate, the biomass pyrolysis process can be divided into two classes: fast (or flash) pyrolysis and conventional (or slow) pyrolysis. Flash pyrolysis and flash hydropyrolysis (pyrolysis in a hydrogen atmosphere) are terms used to describe pyrolysis with reaction times of only a few seconds or less[36]. The main goal of fast pyrolysis is to convert the maximum amount of biomass into liquid. In practice, about 40–75% of the biomass (on dry basis) is converted into pyrolytic oil, with about 10–20% of the biomass converted into char [37]. Fast pyrolysis offers a flexible and attractive way of converting biomass into a liquid, which can be easily stored, transported and handled for the production of heat, power and chemicals[35]. The reason for this high liquid yield is that a high heating rate provides less time for the dehydration reactions and reduces the formation of anhydrocellulose, the precursor of char. The result is that the rapid heating of biomass favors the polymerization of cellulose and the formation of volatiles and suppresses the dehydration to anhydrocellulose and char formation[32]. Therefore, bio-oil production is maximized and biochar production is minimized. Experimental studies suggest that higher heating rates (i.e. fast pyrolysis) produce chars with higher macroporosities, larger macropore surface areas, high reactivity, higher oxygen and hydrogen contents, and thus a higher availability of active sites and larger macropore sizes[38, 39]. The reason is that a higher heating rate results in higher hydrogen and oxygen and lower nitrogen and carbon contents of biochar. The hydrogen content can be related to the availability of active sites[40].

Conventional (or slow) pyrolysis is used for producing biochar (mainly) and chemicals (such as methanol and acetic acid) at a low heating rate, and has been used for hundreds of years. In practice, more than 20% of the biomass is converted into biochar at a low heating rate. Unlike fast pyrolysis biochar, slow pyrolysis biochar has less surface active sites, making it more suitable for soil amendment[39].

The decrease in char yield with increasing temperature can be attributed to the competition between charring and devolatilization reactions. The volatile gas yield increases as temperature increases[41]. The fixed carbon and the elemental carbon contents of the biochars increase with temperature at the expense of volatile matter, elemental oxygen, and hydrogen.

A widely known characteristic of biochar is the existence of condensed aromatic ring structures, which increase with temperature to above 450°C to become larger aromatic clusters and finally large graphitic sheets. The size of ring clusters is believed to relate to its long-term stability in soil [42], with larger ring clusters being more stable. With increasing heat treatment temperature (HTT), the changes in the biochar chemical composition are characterized by the conversion from O-alkyl carbon to aryl and O-aryl (furan-like) aromatic structures [40], which transforms bio-accessible compounds to more environmentally stable ones [43]. When the HTT is below a threshold of about 450°C, predominantly small biochar clusters are produced which are easier to oxidize than larger biochar units and, thus, may be more easily degraded [44]. Knicker et al.[45] prepared biochar by controlled charring of biomass at 350°C and found a low aromatic carbon content with considerable N, O and S substitutions. Such heterogeneous biochar would likely be more vulnerable to biological and chemical oxidation. Therefore, my work focused on the high-temperature (HTT≥ 450°C) biochar, which should be the most stable.

Besides the pyrolysis conditions, biomass raw materials need to be carefully selected. Biomass is very heterogeneous and its components (holocellulose, lignin and extractives) react differently during thermal conversion. Feedstocks with high lignin content, such as wood, produce biochars with higher charcoal yields since lignin is preferentially converted to char during pyrolysis [46-48]. The high yield of carbon from lignin is, in part, a result of its low oxygen content relative to the carbohydrate components. The greater the thermal stability of the aromatic

structure, the lower the volatility of decomposition products [49]. At elevated pressures and temperatures, however, high charcoal yields can be obtained with feedstocks having relatively low lignin content [47, 50]. The theoretical yield of biochar from various carbon contents biomass is in the range 50-80% on a dry biomass weight basis [51].

Heating rate has a significant influence on cellulose pyrolysis [32]. When combined with the different decomposition behavior of each component, differences in the cellulose, hemicellulose and lignin contents of biomass feedstocks result in diversity in pyrolysis behavior with different kinds of biomass feedstock. Cellulosic materials quickly decompose in a very limited temperature range of 300–400 °C. Woody materials are the most thermally stable, requiring the longest pyrolysis duration. The pyrolysis of grasses starts earlier than the other two kinds of material with a medium reaction rate[52]. In my study, I compared the biochar generated from woody biomass and grass biomass.

In most of the previously mentioned investigations, the effect of particle size of biomass on biochar properties was neglected. The role of particle size in the pyrolysis process is quite controversial. Some reported no relationship [53-55], while the majority believed that the biochar yield increased with increasing particle size [32, 56, 57]. This is because small particles have enough surface area to be more thoroughly pyrolyzed to form volatile products. In case of larger particle sizes, this led to char formation due to unthroughly pyrolysis. On the other hand, mass and heat limitations are more severe inside the larger particles [56]. I performed a thorough analysis to study the particle size effect.

As mentioned above, biochar properties vary greatly, depending on the biomass used to produce biochar and the production conditions (such as pyrolysis temperature). Biochar produced below 400°C has a low pH, low CEC, and small surface area, and may therefore not be

suitable for improving soil fertility. Similar assessments for the stability of biochar in the environment are not yet available, but should show important effects of both production procedure and biomass type. A rapidly decaying form of biochar is less likely to be a sustainable improver of soil or a long-term carbon sink. Pyrolysis conditions strongly affect the long term stability of biochars and their ability to retain nutrients, water, and natural organic matter in soil[15, 40]. Properties of biochar that make it a promising soil amendment include its resistance to decay and its ability to retain soil water and nutrients for plant growth[6]. There are two possible explanations for the long term stability of biochar: (a) inherent chemical resistance of the solid aromatic backbone to microbial decay, and (b) reactivity of the biochar surface structures and dissolved fragments towards Al and Fe oxides, producing mineral-complexed organic matter[58]. Therefore, a through understanding of the relationship between pyrolysis conditions and biochar structure is needed.

Many fundamental aspects of the biochar pyrolysis process are still not well understood[59, 60], making it challenging to determine the specific pyrolysis conditions needed to optimize the structure of biochar for carbon sequestration and soil fertility improvement. Multiple studies have shown that the final heat treatment temperature (HTT) used for the preparation of a biochar is an important control on its physical and chemical properties [40, 44, 61-65]. The role of HTT has not been fully elucidated, however, since most studies were not designed to test for other potentially important controls (heating rate, holding time, biomass raw materials and particle size) and to discriminate between their effects. Previous studies have often used either muffle or tube furnaces, or fluidized bed reactors to produce biochar, setups that do not allow for very accurate monitoring of the temperature of a biochar sample, due to the large volume of the reactor or variations in heating between regions of the biomass. Other potentially important

controls (heating rate, holding time, biomass raw materials and particle size) are studied mainly to focus on their impacts on biochar yields [32, 56]. Therefore, I used a custom-built, precisely controlled reactor to distinguish the impact of the above-mentioned factors on biochar physical and chemical structures.

1.3 Characterization the pore structure of biochar

Biochar pore structure begins to develop at 450 °C, when microporous structures start to form[66]. The total development of the char microporous structure requires pyrolysis at 600 °C or higher temperatures [67]. However, the biochar specific surface area decreases when the pyrolysis temperature is higher than 900 °C [39]. This is attributed to the partial graphitization of the carbon at 900 °C. The carbon graphitization process consumes the disorganized carbon and increases the graphitic layers, affecting the char properties [39]. The same trends are observed in the micropore volume data[68].

On the other hand, increasing the heating rate results in variation in the pore characteristics of the biochar samples [39]. Average pore diameters and total pore volumes decreases with increasing heating rate, while the specific surfaces increases [39]. This suggests that the removal of only a small fraction of volatile matter led to a considerable development of the char porosity. Biochars have low specific surface areas; therefore, they must be thermally or chemically activated before being used as adsorbants [39].

Increasing temperature alters the relative properties of different sized pores. Generally, increasing the temperature results in increasing the micropore volume, but the increase is more remarkable for smaller sized micropores. Increasing the temperature decreases the mesopore volume. Increasing the temperature has negligible effect on macropore volume [69].

Biochars have a complicated pore structure consisting of multiple interconnected networks of micropores, mesopores and macropores[59, 70-74] that span multiple length scales: from sub-nanometer micropores to macropores with sizes of the order of 10 microns or larger. Such pore structures cannot be characterized by a single analytical technique, such as nitrogen adsorption with BET analysis. A combination of analytical techniques must be used to bridge the vastly different length scales: adsorption of multiple gases (like nitrogen, carbon dioxide and water) for the smallest pores (typically smaller than 50 nm)[75-77], mercury porosimetry for the intermediate pores and stereological methods[78] based on sectioning, image analysis and 3-D reconstruction techniques for the largest pores (typically larger than 1 μm).

Every one of these techniques has its limitations. For example, BET nitrogen adsorption analysis is the most widely used technique in charactering biochar surface area [79]. However, we should keep in mind it is not accurate to rely only on BET results to determine the biochar pore size, if the micropores are the dominant pore structure. The pore volume and surface are detected by N_2 physisorption mainly shows the characteristics of the pores larger than 2 nm and smaller than 50 nm. Due to the severe pore constrictions, micropore volumes determined from the N_2 isotherms do not represent the total micropore volumes, but larger micropores. However, these larger micropore volumes can be used to compare structural changes among chars produced at various conditions[80]. If using N_2 adsorption to characterize microporous carbon materials, normally it takes more than 60 hours or more to obtain the adsorption isotherm due to the poor diffusivity of N_2 in mocropores at 77°K (-196°C). Therefore it takes lots of time to reach experimental equilibrium. However, a CO_2 adsorption isotherm either at room temperature or 0°C is easiliy to obtain [81]. The reported micropore volume measured by CO_2 is larger that measure by N_2[80]. Mercury porosimetry is normally used to obtain macropores. The pressure

may lead artifacts to pore size distribution at low pressure range, may even crack the macropores at high pressure range [82]. Other sophisticated measurement techniques to detect the largest pores (typically larger than 1 μm) includes X-ray microtomography and 3D micro-CT [70, 83, 84]. X-ray microtomography as a tool for the non-destructive, three-dimensional examination of the internal structure of charcoal using randomly selected vertical/horizontal image slice can identify and map the distribution of mineral contaminants within charcoal fragments and pore structures [70]. 3D micro-CT and pore partitioning study can derive pore scale parameters including pore radius distribution, accessible radius, throat radius, and connectivity over the pore space [83]. Longitude and transverse reflected light optical microscopic (ROM) images can also show the microstructures of porous carbon materials [84].

As a result, it is very difficult to piece together an accurate picture of the geometries, size distributions and interconnectivity of the pore networks of biochars even when all these time-consuming techniques are employed.

When biochars and activated carbons were used primarily as adsorbent materials, most researchers focused their attention on characterizing the micro- and mesopore structures of biochars using various gas adsorption techniques[75]. Pores larger than 50 nm were considered to be of secondary importance since their main role was to serve as feeder pores for the transport of adsorbate molecules[74]. When biochars are used for soil amendment, however, macropores play vital roles in modulating the interactions of biochar particles with water [38, 85-90], microbes and plant roots[88, 91-95]. Thus, it becomes imperative to seek new approaches that can measure the micro-, meso- and macropore networks.

1.4 Biochar adsorption

Under any production scenario, the cation exchange capacity (CEC) of freshly produced biochar is relatively low. Only aged biochar shows high CEC values, as in Amazonian Dark Earths [96]. It is not clear under what conditions and over what period of time biochar develops its adsorbing properties [33]. At high temperatures (30–70°C), cation retention properties evolve within a few months after biochar biotic or abiotic inoculation [97, 98]. If certain types of biochar under certain environmental conditions require decades of exposure to microbial and abiotic oxidation to develop the cation retention properties that justify their application, then the technology would not be successful.

Therefore, it is important to develop a new theoretical framework that will allow us to evaluate the beneficial effects of soil amendment by biochar and, more specifically, to design biochars with optimal properties for each application. The environmental performance of biochars will depend on their ability to adsorb, retain and release water and nutrients. These biochar properties are controlled by their porosity and surface chemistry, which can vary widely depending on the composition of the biomass feedstocks and on the pyrolysis conditions employed during biochar production.

Properly “engineered” charcoals can increase the water holding and cation exchange capacities of soils, improving the ability of plants to survive under drought conditions and reducing fertilizer runoff into watersheds. Once applied to a certain location, biochar additions may not need to be repeated annually, as exemplified by the persistently high fertility of Amazonian Dark Earths over several hundred to thousands of years, as well as by remnants of historic biochar production [14]. Fertilizer runoff has become a serious problem, because as much as 70% of fertilizer applied to crop fields is leached into the groundwater or lost to streams and

rivers, eventually leading to large hypoxic 'dead' zones in the world's oceans (including the Gulf of Mexico)[99].

Ammonium is a major component of fertilizers and is used to improve plant growth. Since plants typically use only about 30% of applied fertizer, however, ~70% will be leached into the groundwater or lost to streams and rivers. There, ammonium creates harmful algal blooms, decreases dissolved oxygen in rivers and lakes, poisons aquatic organisms, totally eliminates fish, and finally, threatens human health[100]. Ammonium is able to form inner-sphere complexes with soil clay surfaces [101, 102]. Biochar can adsorb ammonium to its surfaces, building a larger plant-available nitrogen pool and minimizing nitrogen losses into the environment.

The addition of biochar to soil can result in major improvements in the fertility of soils [4, 14, 103]. The crop growth enhancement seen in biochar-amended soils is due, in part, to the capability of biochar to hold soil nutrients in a plant-available form[4]. Nutrient sorption is a function of both the surface chemistry of the char and its porosity. Both char porosity and surface chemistry are determined by pyrolysis conditions, which mean that it is possible to make chars that vary significantly in their effect on crops.

Although biochar has been shown to improve the performance of many crops [18-21, 104], it sometimes does not improve crop performance, or does not act to efficiently sorb soil nutrients. The cation exchange capacity of biochars varies widely and depends strongly on both the biomass feedstock and pyrolysis conditions [6, 105]. Novak et al.[106] showed one of the first published examples of a biochar that did not improve a soil's CEC. Their biochar did improve other soil properties (soil pH and Ca, K. and P), leading to a net improvement in the soil quality. Since their biochar was prepared at high pyrolysis temperatures, the authors concluded that it did not have the appropriate surface chemistry to enhance the CEC of the soil/biochar mixture. Other

studies have also found pyrolysis conditions that do not lead to char that improve crop performance[107].

1.5 Objectives and significance of this study

The extensive experimental and mathematical modeling work conducted in my research is summarized as follows:

Biochar pyrolysis and characterization experimental study

To determine the pyrolysis conditions that lead to biochars with useful environmental properties, I generated a "library" of biochars using a custom-built, precisely controlled pyrolysis reactor. My goal was to fully understand the impacts of different pyrolysis conditions on biochar physical and chemical structure. I varied four feedstock and pyrolysis parameters: final heat treatment temperature (450°C or 600°C), heating rate (1°C/s or 0.1°C/s), particle size (1.5 mm or 0.25 mm), and feedstock (corn stover or apple wood).

The chemical and pore structure of the produced biochars were carefully characterized using a suite of analytical techniques. Each technique was chosen because it could quantify a fundamental chemical or physical property that can be connected to the carbon sequestration capacity or the environmental behavior of the biochar. I used elemental analysis (EA) to determine the carbon yield, which sets the upper limit of how much C can be sequestered. NMR was used to determine the bulk chemical structure and degree of aromatic condensation, which are thought to determine how easily biochar can be degraded by microbes[73]. The chemistry of the biochar surface was probed using X-ray photoelectron spectroscopy (XPS).

The temperature history of biomass particles can be determined if we know their size, their physical properties (heat capacity, conductivity etc.), the temperature of their surroundings and

the kinetics of all the chemical reactions that occur within the particles. Then, the temperature history of pyrolyzing biomass particles can be computed by integrating a system of ODEs that describe the mass and energy balances for our system.

Biochar pore structure experimental and modeling study

I report here the development of a novel approach to probe the multiscale pore structure of biochars. This approach uses thermogravimetric measurements of the transient reactivity of biochars in air over a wide range of temperatures, using (a) the classical diffusion-reaction theory[108] and (b) mathematical models that describe the temporal evolution of the porosity of solid reactants with the extent of combustion[78, 109, 110].

The novelty of my approach lies in the use of sophisticated discrete models that can accurately describe the temporal evolution of the surface area of solid reactants with complicated pore structure. The new models are significant extensions of the continuous [109, 110] and discrete models[78] that have appeared in the literature. Simulations start by generating solids with the desired pore structure on three-dimensional computational grids. Pores of various shapes and sizes are distributed on the grid in a random or orderly fashion to match the experimentally determined micro, meso- and macroporosities, as well as any available information about the shape of the pores. The generated porous solids are then eroded using rules that simulate non-catalytic reactions between a gas and a solid reactant. Access of the gas reactant into pores of progressively increasing sizes is restricted to model pore diffusional limitations and parallel simulations are carried out to handle the multiple scales of this problem. Multiple realizations of a solid with the same pore structural properties are generated and reacted to estimate the average pore surface and to establish confidence intervals. For a given pore structure, this process will generate a family of curves that give the evolution of pore surface area with conversion as the

intraparticle diffusional resistances increase. A comparison of these surface evolution patterns to the char reactivity patterns measured at different temperatures can provide important information about the complex pore structure of carbonaceous materials [78, 109-111], such as the shape, spatial arrangement and connectivity of the multiple pore networks present in biochars.

Biochar adsorption modeling study

While it is clear that the physical and chemical structure of biochars strongly affects environmental performance, we know of no systematic study that has examined these effects individually. In an effort to fill this gap, I carried out a theoretical study that quantifies the ability of soils amended with known amounts of well-characterized biochars to adsorb and release a key nutrient for plant growth. This mathematical model explicitly considers a heterogeneous packed bed consisting of a mixture of porous biochar particles and soil grains. This analysis reveals the effects of various biochar properties on these important processes and quantifies their kinetics.

Very few previous works have modeled ammonium transport in soil. The partial differential equation model I have already developed to analyze experimental data is a significant extension of what has been used before in this area. For example, earlier models considered adsorbent particles to be impervious to ammonium diffusion[112]. Moreover, previous studies only considered homogeneous systems with one absorbent. This is the first model that considers a multi-absorbent heterogeneous system of soil amended with biochar and explicitly accounts for intraparticle diffusion in the porous biochars. For instance, my mathematical model analyzes breakthrough curve data and quantifies the differential effects of the key processes: (a) diffusion and adsorption of the solute in the porous biochar particles. It was impossible to measure the intraparticle concentration through experiments. Therefore, the model results can provide insights into the intraparticle mass transfer during the adsorption process; (b) solute adsorption of

the surface of impervious soil grains; (c) dispersion in the packed bed. Quantification was obtained by adjusting key model parameters so that experimental measurements agree with the model predictions.

Similarily, the water infiltration rates and water saturation profiles of unsaturated water flow have been widely studied in civil and petroleum engineering. However, most of the studies are based on single porosity, single permeability models, by treating the porous media homogenously [113, 114]. By dividing the porous media as two distinct regions (bulk/particles), multi-porosity multi-permeability model considered fluid mass transport inside different pore regions separately and fluid mass transport exchange between different pore regions [115-117]. . This is the first model that considers a multi-component heterogeneous system of soil amended with biochar.

CHAPTER 2

Materials, Experimental Equipment and Procedures

2.1 Biomass Feedstocks

Apple wood (*Malus domestica*) sawdust was purchased from Allied Kenco (Houston, TX, USA) and oven-dried (60°C). Corn stover (*Zea mays*) was obtained from the Kellogg Long-Term Ecological Research station (Hickory Corners, MI, USA). My samples came from a conventionally managed corn crop harvested in 2005. Stover was separated from the leaves and reproductive tissues and then oven dried (60°C). Apple wood and corn stover were ground in a Wiley cutting mill (Thomas Scientific Inc.) until particles passed through 20 or 60 mesh sieves.

2.2 Fixed-bed Pyrolysis Reactor

2.2.1 The reactor system

The main design objectives for our pyrolyzer were: (a) accurate and direct measurement of the pyrolyzing biomass temperature, (b) precise temperature control and (c) flexible and reproducible temperature programming. To achieve the first objective, I used small biomass samples and a fine thermocouple embedded in the pyrolyzing mass. The latter objectives were achieved by developing a sophisticated feedforward-feedback control scheme for our reactor.

Our custom-built fixed bed reactor is machined from 316 stainless steel. A water-cooled jacket keeps the temperature around the reactor constant to provide for better temperature control. The biomass sample holder is a 1.5 ml porcelain crucible surrounded on three sides by the heating element that is made from nichrome ribbon. The reactor top is a flat optical window

made of quartz glass to allow for direct observation of the pyrolysis process using video microscopy. Mass flow controllers (247C, MKS) are used to control the flow rate and composition of gas flowing through the reactor. Nitrogen flowing at 150 mL/min was used for all the pyrolysis experiments of this study.

The temperature of the reactor is programmed with a custom-built data acquisition and control system (Figure 2.1). To provide for accurate measurement of the sample temperature and precise control of the reactor, a sheathed chromel-alumel type K thermocouple (TJC36-CAXL-040U-12, Omega) is inserted directly between the biomass particles. The thermocouple signal is isolated and linearized by signal conditioning modules (USB-9211A, National Instruments) that have a gain of 10 mV/°C. The calculated control signal is sent to the phase-fired heater controller using a data acquisition board (USB-6009, National Instruments). The program that controls the temperature of the reactor and the composition of the pyrolysis atmosphere runs on a personal computer (iMac, Apple Computer) and was developed using the LabView software (National Instruments). It implements a combination of feed-forward and feedback control algorithms. The feed-forward algorithm is based on a process model derived with the procedure we described in an earlier publication [118]. Feedback control is used to compensate for model inaccuracies and for the temperature dependence of the process parameters, thus ensuring high repeatability [119]. Our custom-built reactor and control software provide for precise monitoring and control that cannot be easily achieved with experimental configurations typically used for biomass pyrolysis experiments (e.g. crucibles or other packed bed reactors placed in muffle furnaces or tube heaters).

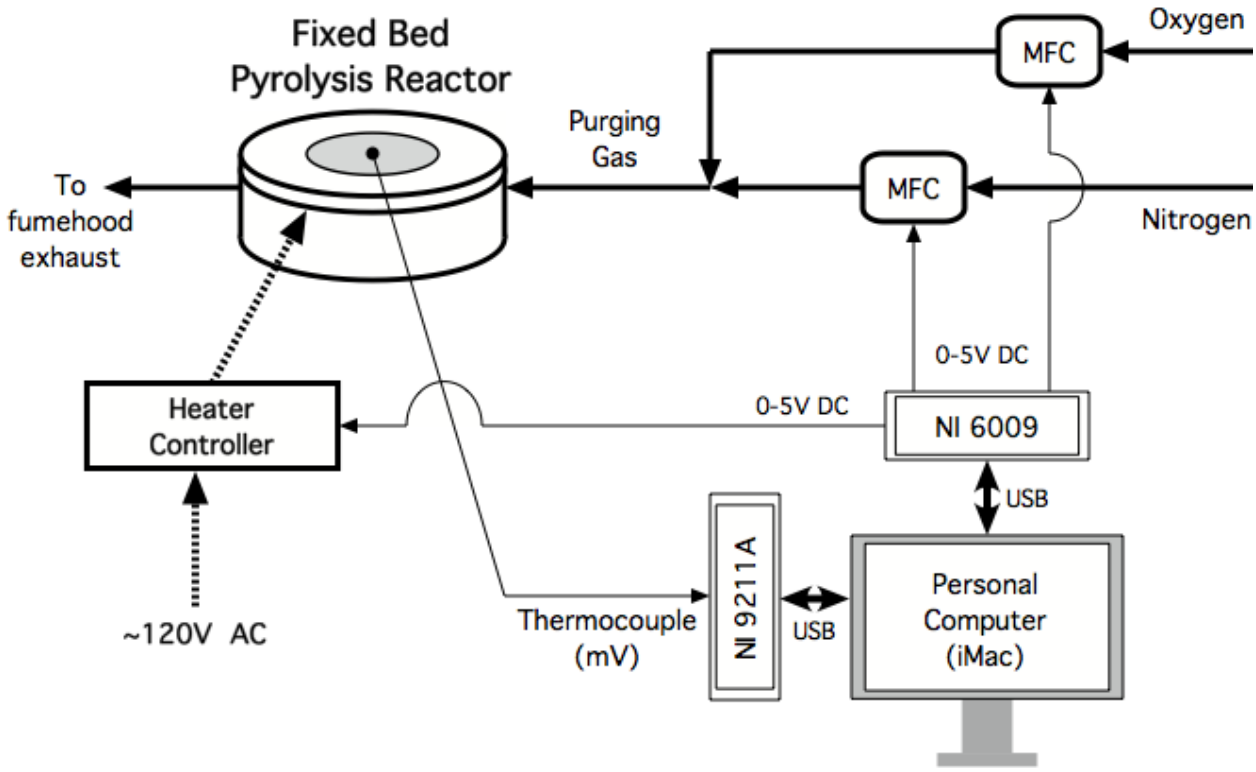

Figure 2.1 Components of pyrolysis reactor system

2.2.2 Digital control algorithm

The digital control algorithm is a combination of a feedforward controller and a standard proportional-integral-derivative (PID) feedback controller (Figure 2.2-2.3). A system feedforward controller was experimentally obtained and used to implement the desired temperature program. Feedback control is used to compensate for model inaccuracies, and for the temperature dependence of the process parameters.

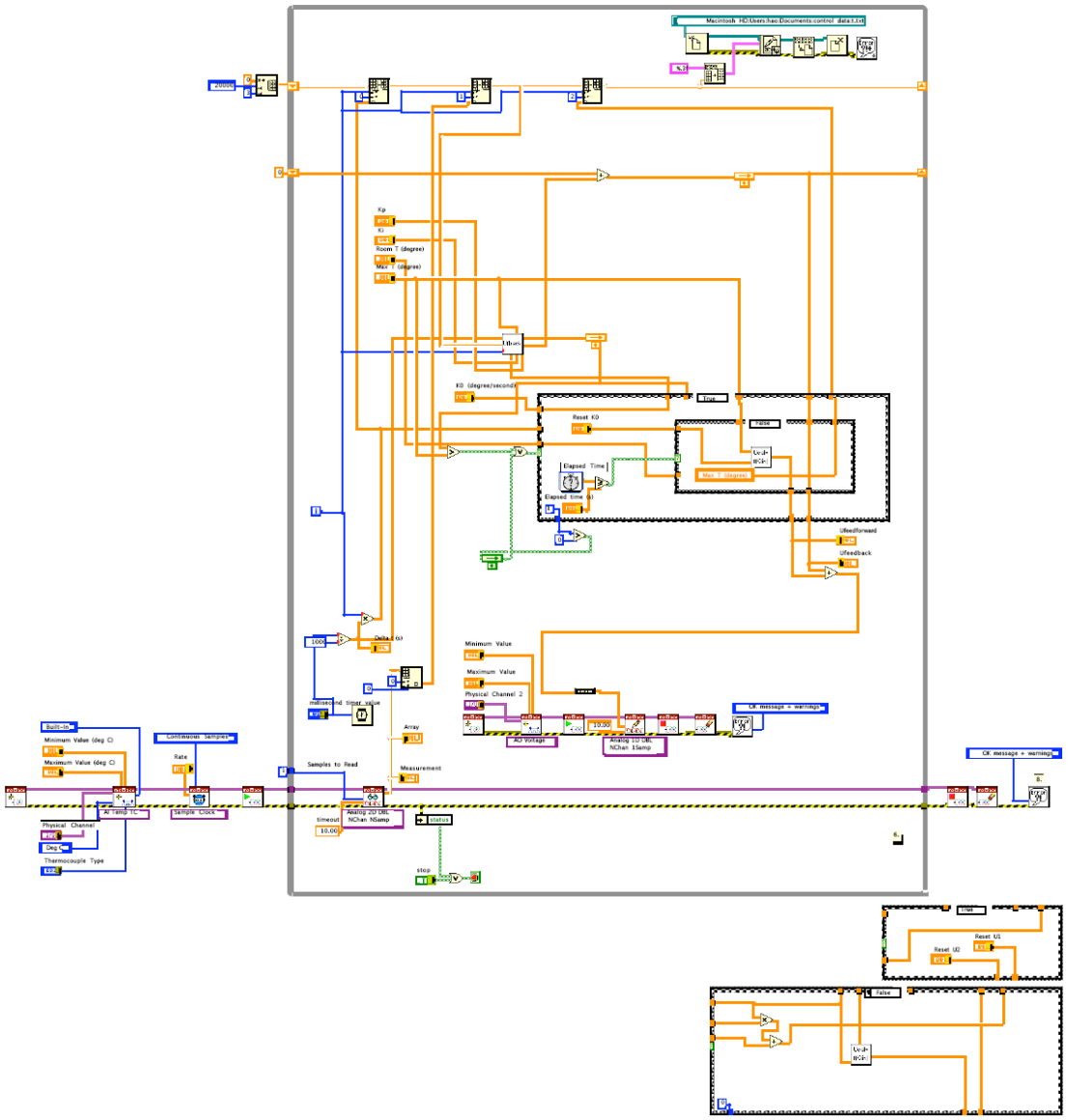

Figure 2.2 Block diagram of Labview control program

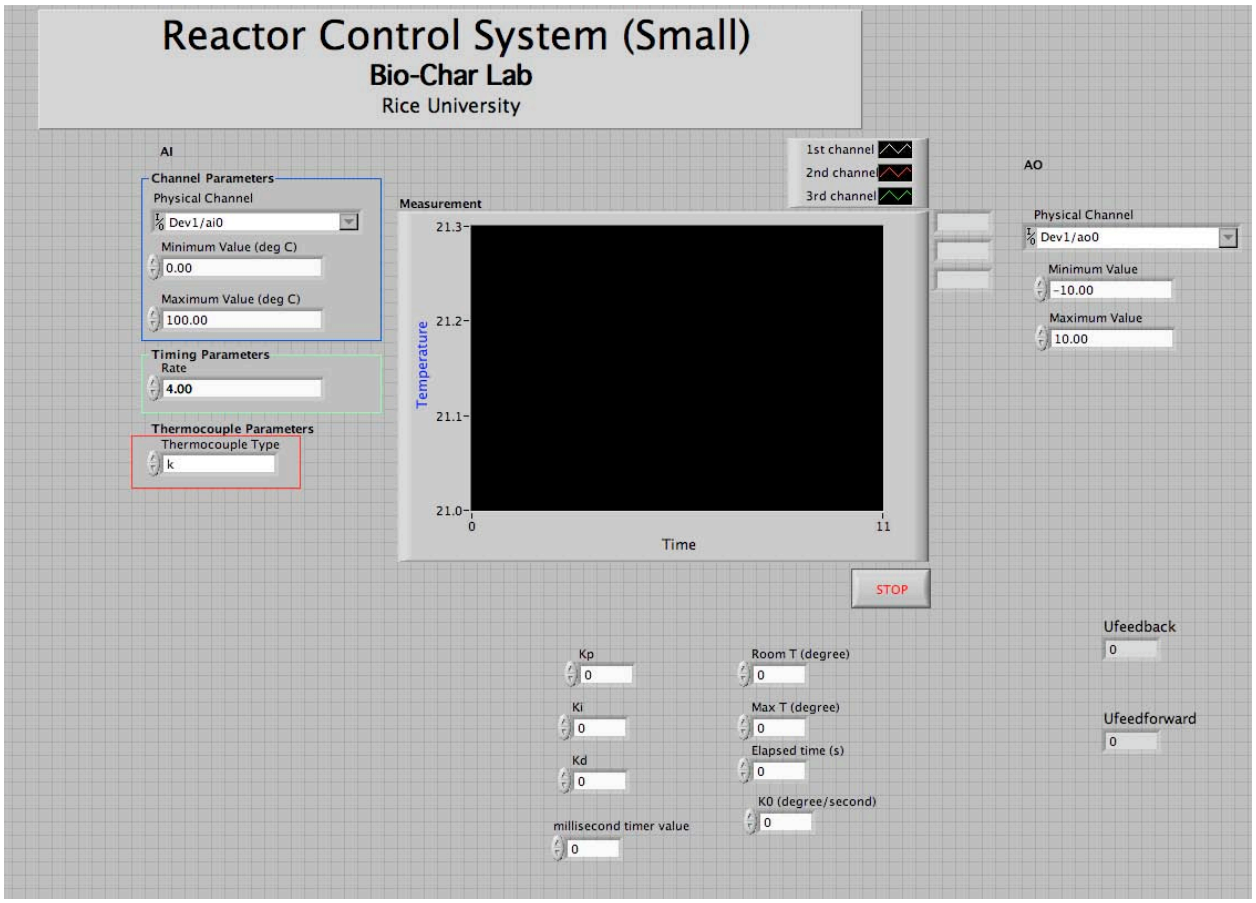

Figure 2.3 Front panel of Labview Control program

Feedforward Control Algorithm:

The process model for feedforward control was obtained by assuming that the reactor dynamics could be described by the following ordinary differential equation[120]:

$$a\frac{dT}{dt} = Q_{in} - Q_{out} \tag{2.1}$$

where T is the temperature of the heated biomass sample, Q_{in} is the power input to the reactor, and Q_{out} is the rate of heat losses to the surroundings. Since the large thermal mass of the reactor block is kept at a constant temperature by circulating water through its copper tube, Q_{out} will depend only on the temperature T, the flow rate and properties of the purging gas. For given

same experiments conditions (0.2g biomass (corn stover/apple wood), constant given water and gas flow rate), open loop experiments were performed to get the temperature-time history of the reactor as a function of reactor voltage signals (Figure 2.4). The unsmoothness of the curves is due to the endothermic biomass pyrolysis reactions, which occurs through the temperature range 200 °C-500 °C. The platua of the curves around 100 °C is due to the evaporation of the sample moisture. Q_{out} can be determined as a function of T by applying several constant power inputs, allowing the reactor to reach thermal equilibrium and recording the final temperatures (Figure 2.5). Due to the severe tar accumulation on the heating element (nichrome ribbon), the final temperature always shows plus/minus 20 °C difference under same voltage signal. I took their ten runs average values. a is the heat capacity of the reactor. Its value is adjusted by fitting to the reactor response obtained from a step change of the power input (Figure 2.6).

$$a = \frac{Q_{in} - Q_{out}}{\frac{dT}{dt}} \tag{2.2}$$

Then the power input Q_{in} required to achieve a given heating rate at any temperature setpoint can be directly calculated as

$$Q_{in}(T) = Q_{out}(T) + a\frac{dT}{dt} \tag{2.3}$$

Finally, the value of the control signal can be found from the desired Q_{in} (Figure 2.7).

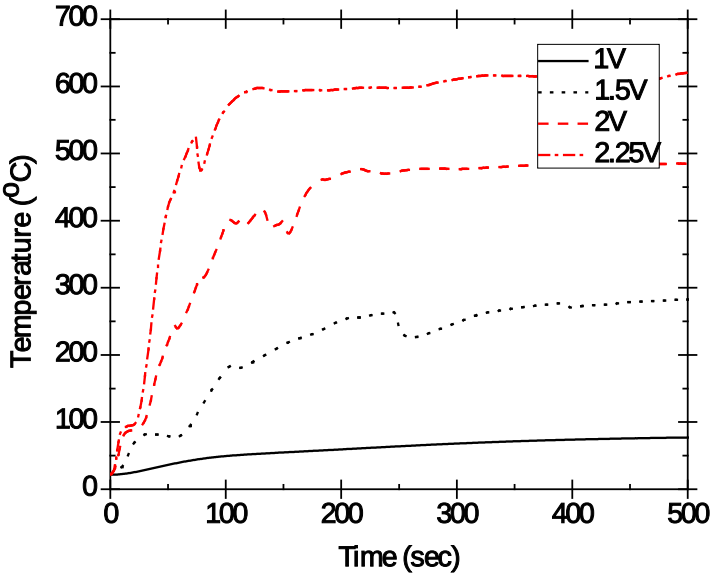

Figure 2.4 Temperature-time history of the reactor as a function of reactor voltage signals

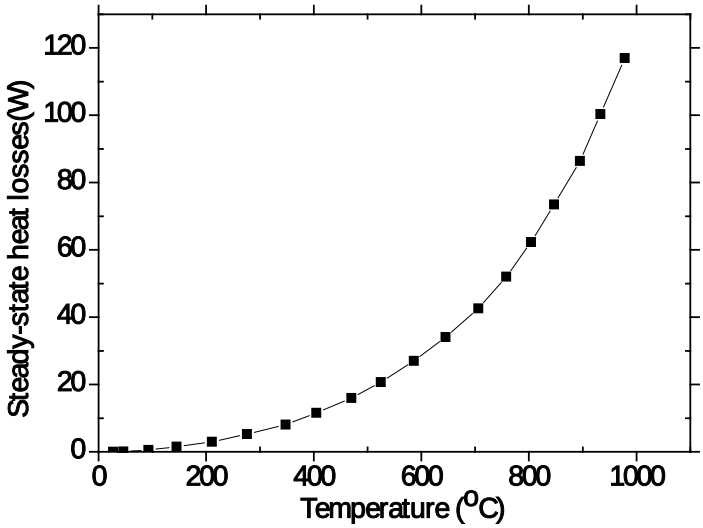

Figure 2.5 Steady-state heat losses from the reactor as a function of reactor temperature

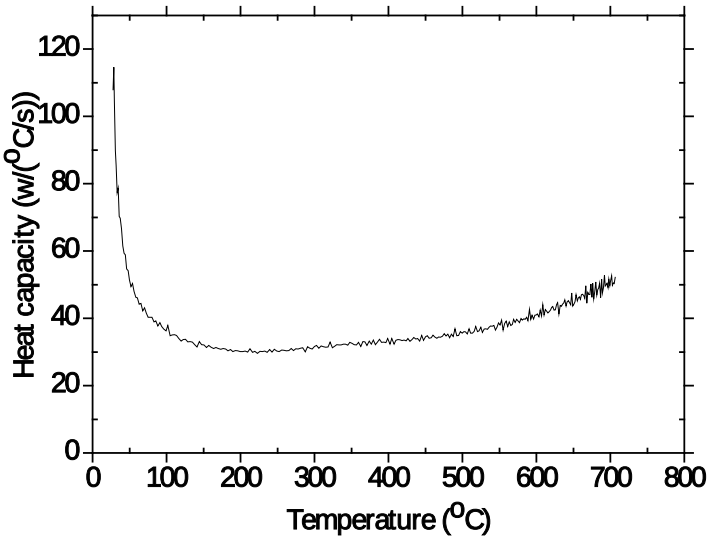

Figure 2.6 Heat capacity (a) of the reactor as a function of reactor temperature

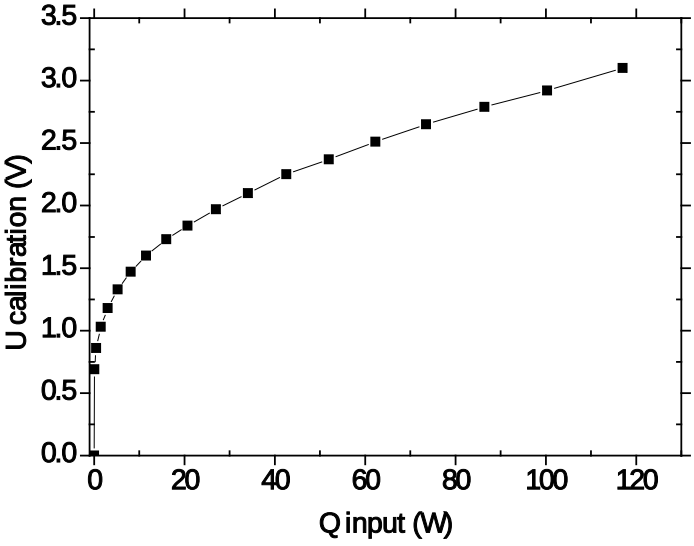

Figure 2.7 U calibrations as a function of Q input

Feedback (PID) control algorithm [121]:

$$e(t) = R(t) - B(t) \tag{2.4}$$

$R(t)$ = set point

$B(t)$ = measured value of the controlled variable

According to PID control theory:

$$\Delta U_{fb}(t) = K_P(e_n - e_{n-1}) + K_I e_n + K_D(e_n - 2e_{n-1} + e_{n-2}) \tag{2.5}$$

$$\begin{aligned}\Delta U_{fb}(t) = {} & K_P[T_0(t) - T(t) - (T_0(t-\Delta t) - T(t-\Delta t))] + \\ & K_I[T_0(t) - T(t)] + \\ & K_D[(T_0(t) - T(t)) - 2(T_0(t-\Delta t) - T(t-\Delta t)) + (T_0(t-2\Delta t) - T(t-2\Delta t))]\end{aligned} \tag{2.6}$$

$$T_0(t) = k_0 t + T_{room} \tag{2.7}$$

$$\Delta U_{fb}(t) = K_P[k_0\Delta t - T(t) + T(t-\Delta t)] + K_I[k_0 t + T_{room} - T(t)] + K_D[-T(t) + 2T(t-\Delta t) - T(t-2\Delta t)]$$

(2.8)

$$\Delta U_{fb}(t) = U_{fb}(t) - U_{fb}(t-1) \tag{2.9}$$

$\Delta U_{fb}(t)$ is the feedback (PID) output voltage changes at time t. K_P is the proportional controller gain. K_I is the integral controller gain. K_D is the derivative controller gain. $T(t)$ is the actual temperature at time t. $T_0(t)$ is the set temperature at time t. $k_0(t)$ is the set temperature rate at time t. Δt is taken as 1s. T_{room} is the room temperature. The same PID control parameters (K_P =1e-2; K_I =1e-4; K_D =1e-2) were used for the whole temperature control scheme, whether ramping or steady-state, showing our system is quite robust. The accurate temperature control ensures high repeatability.

2.3 Pyrolysis Protocol

2.3.1 Small reactor pyrolysis protocol

For a typical pyrolysis experiment, about 0.2 g of biomass was heated at either 1 or 0.1°C/s until the reactor temperature had reached the final heat treatment temperature (HTT). After keeping the reactor at the HTT for a set period of time (usually 60 minutes), the heater was turned off and the reactor was allowed to cool down. For a few experiments, the heater was turned off as soon as the reactor had reached the HTT. A constant flow of nitrogen at 150 ml/min was maintained through the reactor during the heating and cooling stages. Three samples of biochar were prepared for each set of conditions and feedstock. The samples were then mixed and used for the analytical measurements.

Figure 2.8 shows the temperature setpoint and the actual reactor temperature for a run with corn stover particles having an average diameter of 0.25 mm, a heating rate of 1°C/s and HTT equal to 600 ºC. During the ramp stage of the temperature program, the temperature of the reacting biomass never deviated by more than 10ºC from the setpoint, except for an excursion of about 40ºC caused by the evaporation of the sample moisture (see insert detail of Figure 2.8). Deviations from the setpoint never exceeded 15ºC during the constant temperature stage of the program. Such small deviations were typical of our experiments.

The biochar yield (ychar) is a measure of the efficiency of the pyrolysis process. I define the biochar yield as ychar = mchar/mbio, where mchar is the dry mass of biochar produced by pyrolysis of a biomass feedstock with dry mass mbio. The overall yield of the biochar from the dry biomass feedstock is about 30 wt% for all my pyrolysis experiments.

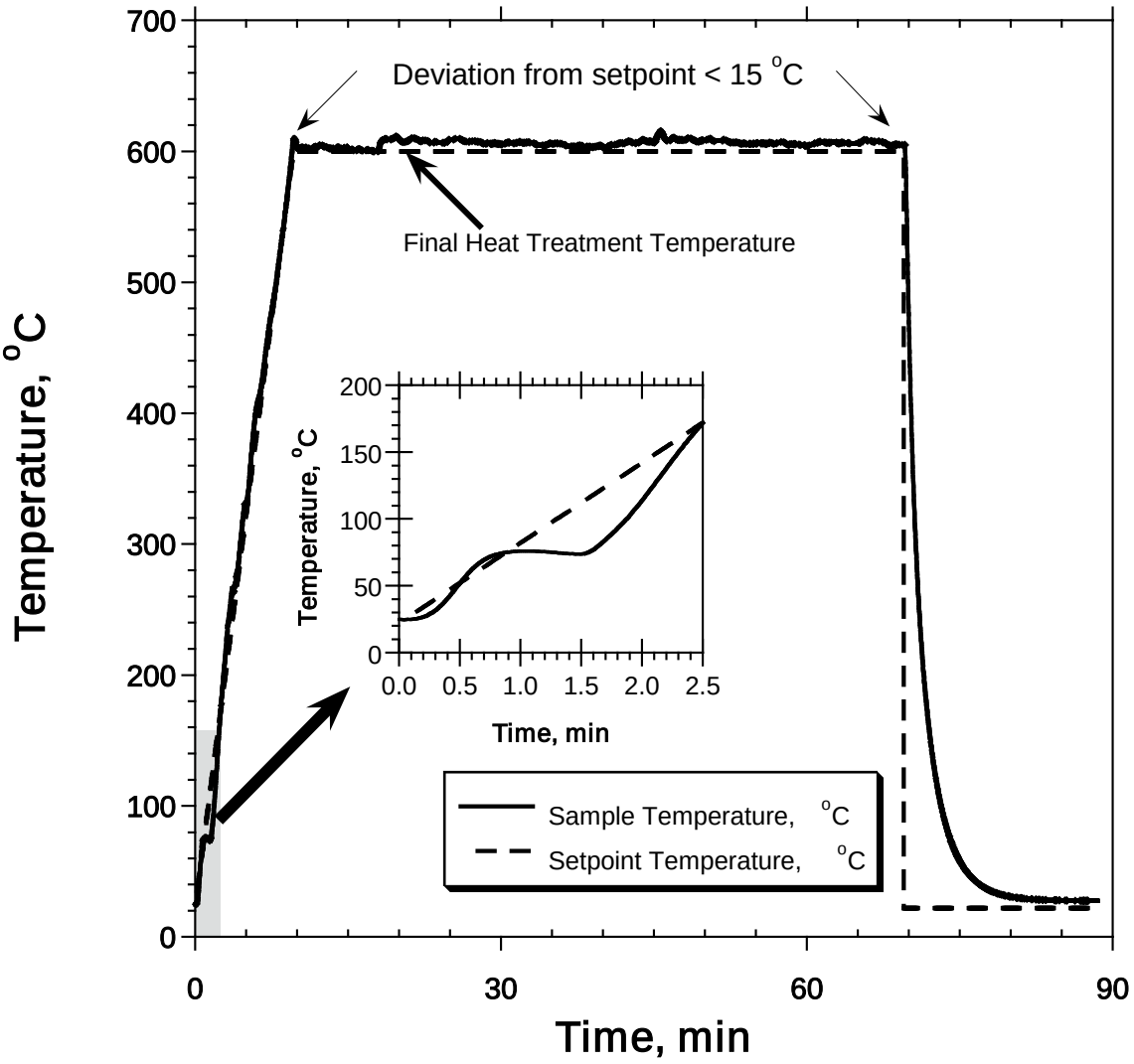

Figure 2.8 Temperature program (setpoint) for the typical pyrolysis protocol and actual temperature measurement from a run with corn stover feedstock (HTT = 600ºC; particle size = 0.25 mm, pyrolysis heating rate = 1ºC/s)

2.3.2 TGA for biomass pyrolysis kinetics characterization

I also performed thermogravimetric analysis to characterize the biomass pyrolysis kinetics. Thermogravimetric analysis (TGA), derivative thermogravimetry (DTG) and differential scanning calorimetry (DSC) were used for this study. The weight loss-temperature profile for biomass is collected on the thermogravimetric analyzer (Q600 Simultaneous DSC/TGA, TA Instruments). A brief summary of the setup is as following: In each TGA experiment, around 5 mg biomass is weighted and spread evenly in a sample platinum pan; the pan is then placed on the balance sample holder; the sample is heated at a rate of 10ºC/min to 105ºC and held at 105ºC for 15 min to remove moisture, which is not considered during the estimation of kinetic parameters. The sample is then heated to 600ºC at rates of 6 or 60ºC /min and then held at 600ºC for 15 min using nitrogen as the carrier gas at a constant flow rate of 150 cm^3/min (Figure 2.9). While in each DSC experiment, the heating protocol is directly to heat up from room temperature to 600ºC at rates of 6ºC /min and then held at 600ºC for 60 min (Figure 2.10).

The biochar sample reactivity $R(t)$ was computed by the formula:

$$R(t) = \frac{dx}{dt} = -\frac{1}{m_0 - m_f}\frac{dm(t)}{dt} \tag{2.10}$$

where x is the conversion of the combustion reaction defined by

$$x = \frac{m_0 - m(t)}{m_0 - m_f} \tag{2.11}$$

$m(t)$ is the measured weight of the sample at time t, m_0 is the initial weight of the sample, and m_f is the final weight of the sample (ash). All TGA measurements were done in triplicate and the average reactivity is reported.

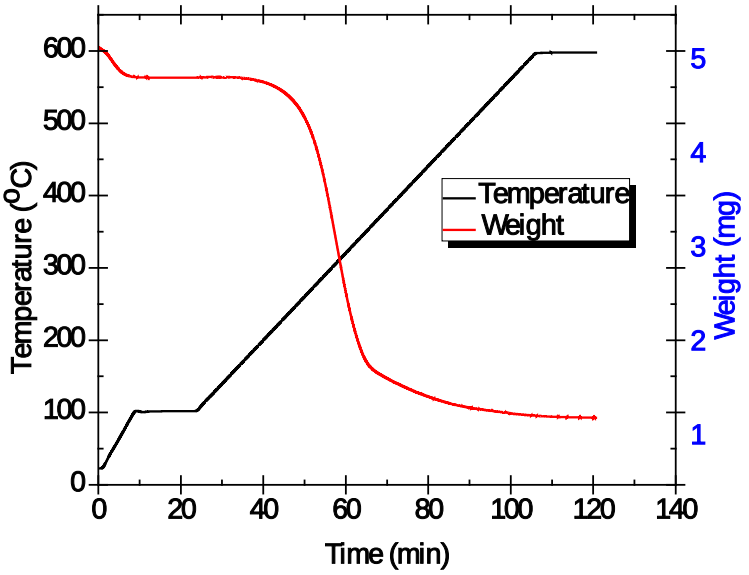

Figure 2.9 TGA measured weight vs. time and temperature vs. time

Heating Rate=0.1 °C/sec, HTT=600°C

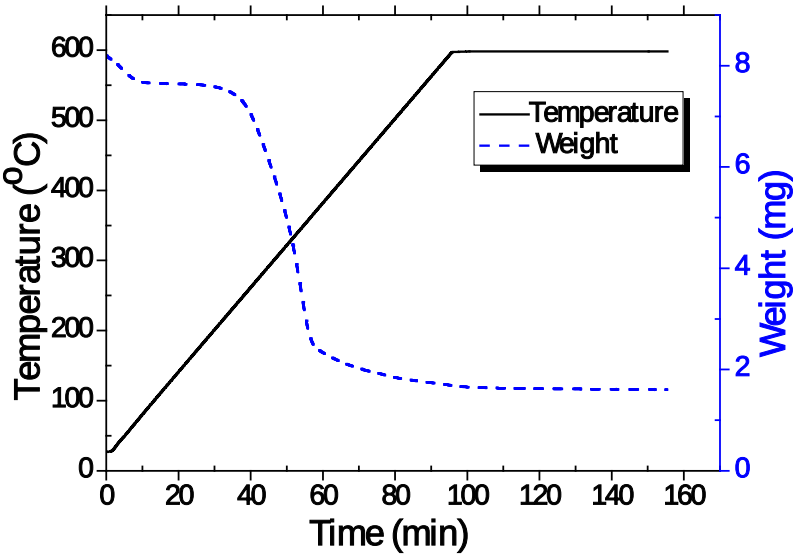

Figure 2.10 TGA measured weight vs. time and temperature vs. time

Heating Rate=0.1 °C/sec, HTT=600°C

2.4 Elemental Analysis (EA)

Measurements of %C for pyrolysis experiments document the mass of original carbon retained in the biochar, an essential term in carbon sequestration estimates. Approximately 3 mg of dried and pulverized sample were placed in a 5 mm × 9 mm tin capsule. The concentrations of C, H, and N were measured in duplicate using a catalytic combustion analyzer (ESC4010, Costech Analytical Technologies). The analyzer was externally calibrated $\left(r^2 > 0.9999\right)$ using a high-purity acetanilide standard (Costech Analytical Technologies Inc., Valencia, CA). The remaining carbon (%) was calculated using the following equation:

$$\text{Carbon Yield}\left(\%\right) = \frac{\text{Biochar C}\left(wt\%\right) \times \text{Biochar Yield}\left(wt\%\right)}{\text{Biomass C}\left(wt\%\right)} \tag{2.12}$$

The biomass ash content was determined by combustion at 600°C in air for 13 hours using a laboratory muffle furnace (550-14 Isotemp Programmable muffle furnace, Fisher Scientific).

2.5 ^{13}C DPMAS NMR Measurements

We used solid state ^{13}C NMR to understand how the molecular structure of chars varied with pyrolysis conditions. We employed both a direct polarization pulse (DP) sequence, which quantified carbon functional groups, and direct polarization in combination with dipolar dephasing (DP+DD) pulse sequences, which we used to determine more detailed structural information.

All NMR experiments were performed using a NMR spectrometer (Bruker 200 MHz DSX, Billerica Massachusetts) operating at a ^{13}C resonance frequency of 50 MHz. We placed approximately 60 mg of pulverized sample into a 4 mm (external diameter) zirconia rotor with a

Kel-F cap. We ran all ^{13}C NMR experiments using a Bruker 4 mm double-resonance magic angle spinning (MAS) probe, operating at a spinning rate of 7 KHz. The ^{13}C chemical shift scale was referenced to tetramethylsilane (=0 ppm) and adjusted with glycine (=176.04 ppm) as an external standard. The 20° direct excitation pulse for ^{13}C was 1.0μs in length and the recycle delay for quantitative DP/MAS ^{13}C NMR was 5 s [122]. The DP spectra represent the accumulation of 6,000 scans to 10,000 scans. We performed a background subtraction to remove signals arising from probe and rotor components made from carbonaceous materials [123].

We also conducted DP+DD NMR experiments to quantify the non-protonated aromatic carbons. The delay time for dipolar dephasing of C-H signals was 50 μs, as determined by the analysis of pure chemical compounds. ^{13}C atoms that have a ^{1}H atom directly attached through a covalent bond relax (dephase) more rapidly than those without a ^{1}H atom due to the magnetic dipolar interaction through the ^{13}C-^{1}H bond. Therefore, at the end of the 50 μs (DD) delay, only the non-protonated ^{13}C atoms (bridgehead carbons) are detected in the NMR spectrum. These data were used to determine the average number of aromatic carbons fused in a cluster according to the algorithm developed by Solum et al[124]. The two arrangements of aromatic rings that we considered in our analysis were: primary (linear) catenation and circular catenation. Primary (linear) catenation is prevalent when the number of carbons per cluster is less than 14, and circular structures more abundant when the number of aromatic carbons per cluster is greater than 24 [124].

We quantified all NMR signal distributions by integrating the signal intensity across eight fixed chemical shift ranges: 190 - 215 ppm (designated as ketone C), 165 - 190 ppm (amide/carboxyl C), 145 - 165 ppm (phenolic C), 110 – 135 ppm (aromatic C), 135 – 145 ppm (alkyl-substituted aromatic C), 95 - 110 ppm (di-O-alkyl C), 60 - 95 ppm (O-alkyl C), 45 - 60

ppm (N-alkyl/methoxyl C), 20 – 45 ppm (methylene C) and 0 - 20 ppm (methyl C) [125]. The signal in spinning side bands (SSBs) was accounted for by: (a) integrating the low field aromatic, alkylated-aromatic, phenolic and amide/carboxyl SSBs, which appear at chemical shifts of (spinning rate(kHz)/50000(kHz)*10^6) ppm higher than those of the corresponding central resonances; (b) adding twice this signal to that of the central bands; and (c) subtracting this signal from that designated as aromatic, alkylated-aromatic, phenolic and amide/carboxyl C signal at appropriate chemical shift ranges [126].

2.6 X-ray photoelectron spectroscopy (XPS)

Since the main objective of this study is to characterize the basic chemical composition and structure of biochars, we chose to use XPS for surface chemical analysis. This technique provides specific information about the functional groups present on the surface of biochar particles and the elemental composition of the top surface layer (3-5 nm) of biochar.

We used an XPS instrument (PHI Quantera XPS, Physical Electronics) with a focused monochromatic Al Kα X-ray source for excitation operated at 40W (15 kV). We collected survey scan spectra in the 1200–0 eV binding energy range in 0.5eV steps with a pass energy of 140eV. XPS can detect all elements except hydrogen and helium, making XPS elemental percentages accurate only for samples without measurable H or He. Because our biochar contains hydrogen, our XPS-derived elemental percentages are meaningful only in relation to other elements (e.g. C/O ratios are correct, but absolute %C and %O values are too high due to the inability of XPS to detect H).

We also conducted high resolution scanning of the C1s region in 0.1eV steps with pass energy of 26 eV. This region of XPS spectra is specific to carbon and provides information on

the bonding environment of carbon atoms at the surface of samples. All carbon functional groups are observed by XPS, making high-resolution spectra in this region quantitative. Low energy electrons and Ar+ ions were used to bring samples to charge neutrality in each measurement.

The C=C, C-C, and C-H bonds exhibit the same binding energy (284.5 eV in our experiments), and thus are grouped together. The C-O binding energy differed (286.1 eV), as did the COO (carboxylate) binding energy at 289 eV. C=O and O-C-O shared a binding energy at 287.5 eV. The 289 eV peak for COO would have also detected CO_3 (carbonate) functional groups, if they were present in our samples (NIST X-ray Photoelectron Spectroscopy Database) [98, 127].

Peak deconvolutions of high resolution C1s spectra were accomplished using the peak fitting software accompanying the instrument, a non-linear least squares curve-fitting program (Multipak software) with a Gaussian-Lorentzian mixed function.

2.7 Pore Structure Characterization

2.7.1 Sample preparation and experimental procedures

The ability to adsorb water and nutrients is potentially one of the most environmentally valuable properties of biochar. Since pore structure is a major control of the sorptive capacities of biochars [38, 86, 89, 91], we used several analytical techniques to characterize the broad range of pores encountered in these materials.

We performed nitrogen adsorption experiments at 77 °K (-196 °C) using a gas adsorption analyzer (ASAP 2010, Micromeritics). Samples were vacuum dried overnight at 250°C and nitrogen adsorption/desorption isotherms were obtained by a 102-point analysis for relative

pressures P/P_o ranging from 1.21×10^{-4} to 0.99, where P is the adsorption equilibrium pressure and P_0 is the vapor pressure of bulk liquid nitrogen at the experimental temperature. The nitrogen isotherms revealed that our biochars are very microporous with the vast majority of their pores being smaller than 2 nm. For this reason, I analyzed the data using both the BET and the Dubinin-Raduskevitch [76] (DR) methods. No attempt was made in this study to characterize the micropores by CO_2 adsorption at 293 °K because the pore volumes and surface areas measured with this technique are associated with sub-micropores whose diameters are smaller than 0.8 nm [75]. Total pore volumes were determined from a single adsorption point at a relative pressure close to unity (P/Po > 0.995)[128]. The mesopore volume was calculated by subtracting the micropore volume from the volume adsorbed at P/Po=0.95[129] . Values for the micropore volume were obtained with the t-plot method. P/ Po < $5*10^{-3}$ are used to intercept the micropore volumes. The Horvath-Kawazoe method was utilized to determine the pore size distributions from a nitrogen adsorption isotherm between 0.000003758 <P/Po <0.3.

Since the large pores may play important roles in microbial and hydrologic processes [38, 86, 89, 91, 93, 94], I visualized the micrometer-scale pore structure of our biochars using scanning electron microscopy (SEM). I obtained scanning electron micrographs using a high-resolution (1.5 nm) thermal field emission electron microscope (JEOL 6500F) capable of imaging at voltages from 200 V to 30 kV. The scanning was carried out at a short working distance (10 mm) and high accelerating voltage (15 kV). Micrographs were obtained at two magnifications: 500X and 5000X.

2.7.2 TGA for pore structure characterization

I also performed thermogravimetric analysis to further characterize the pore structure and the connectivity of the micropore and macropore networks of our biochar samples. For each TGA experiment, about 5 mg of biochar was spread evenly in a platinum pan that was then placed on the sample holder of the thermogravimetric analyzer (Q600 Simultaneous DSC/TGA, TA Instruments). Using argon as the carrier gas at a constant flow rate of 100 ml/min, the sample was first heated at a rate of 10°C/min to 250°C, held there for 60 min to remove moisture, and then heated to a temperature ranging from 325 to 700°C again at a rate of 10 °C/min. When the desired temperature was reached, I switched the gas from argon to air to start the combustion reaction. The sample was held at the reaction temperature for 360 minutes until all the carbon was reacted and only ash remained (Figure 2.11). The temperature-time peak corresponds to the exothermic biochar combustion process.

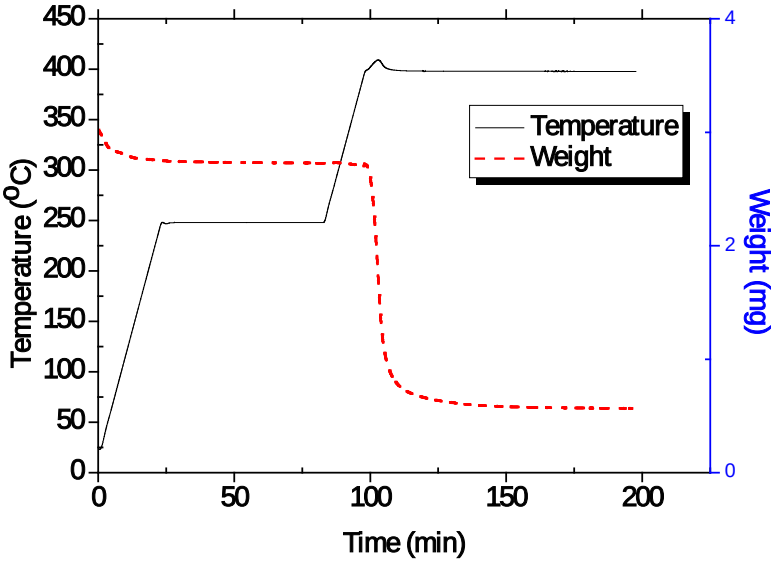

Figure 2.11 TGA measured weight vs. time and temperature control vs. time

Heating Rate=10°C/sec, Combustion Temperature=400°C, O2%=21%

The biochar sample reactivity $R(t)$ was computed by the formula:

$$R(t) = \frac{dx}{dt} = -\frac{1}{m_0 - m_f}\frac{dm(t)}{dt} \tag{2.13}$$

where x is the conversion of the combustion reaction defined by

$$x = \frac{m_0 - m(t)}{m_0 - m_f} \tag{2.14}$$

$m(t)$ is the measured weight of the sample at time t, m_0 is the initial weight of the sample, and m_f is the final weight of the sample (ash). All TGA measurements were done in triplicate and the average reactivity is reported.

Since numerical differentiation is used to obtain reactivity, it is essential to choose the appropriate method to interpolate the raw weight data. During each experiment, thousands of weight data points are collected (depending on the burn-off time as well as the data acquisition frequency). Although the raw weight vs. time curve was monotonically decreasing, the weight data tended to oscillate along the curve due to the high sensitivity of the TGA weighing system. Note that I cannot detect these rate oscillations from the weight approximations. A cubic spline method was initially used to interpolate the data. Since this interpolating method generated a function to match all data points including the oscillating ones, the calculated reactivity curve was quite noisy (Figure 2.12). The raw sample weight data were smoothed using a least-squares method with piecewise quadratic splines [130] to improve the interpolation quality. The rate computed with quadratics is piecewise-linear (because the second derivative of the weight function may be discontinuous. It divided the whole raw weight data set into subintervals. Within each subinterval, B-spline method interpolated weight data in the least-square sense (L2 norm) and required continuous first derivative between subintervals. Since my program allowed for

dynamic placement of the break points so that each subinterval contained more than 25 data points, data noise could not significantly influence the interpolation. I chose C-1 quadratics as the interpolating polynomial at each subinterval. The earlier studies in our lab also indicated that the discontinuous 1st derivative of the combustion reactivity plot could be caused by the opening of large internal pores during the combustion in the diffusion limited regime [119]. By assuming that the reactivity is a linear function of time at each interval, C-1 quadratics preserve the fine details of the reactivity curve which would be smoothed out by a cubic spline [119]. The approximation with cubics and a large number of breakpoints oscillates significantly as the rate goes through its maximum (Figure 2.13). I choose parameters of our codes as: Input order of spline=2 (quadratic splines), Input number of breakpoints =51, Input RUNID character string=_3, Input number of passes for knot improvement=20 and Input number of additional breakpoints per pass=0.5.

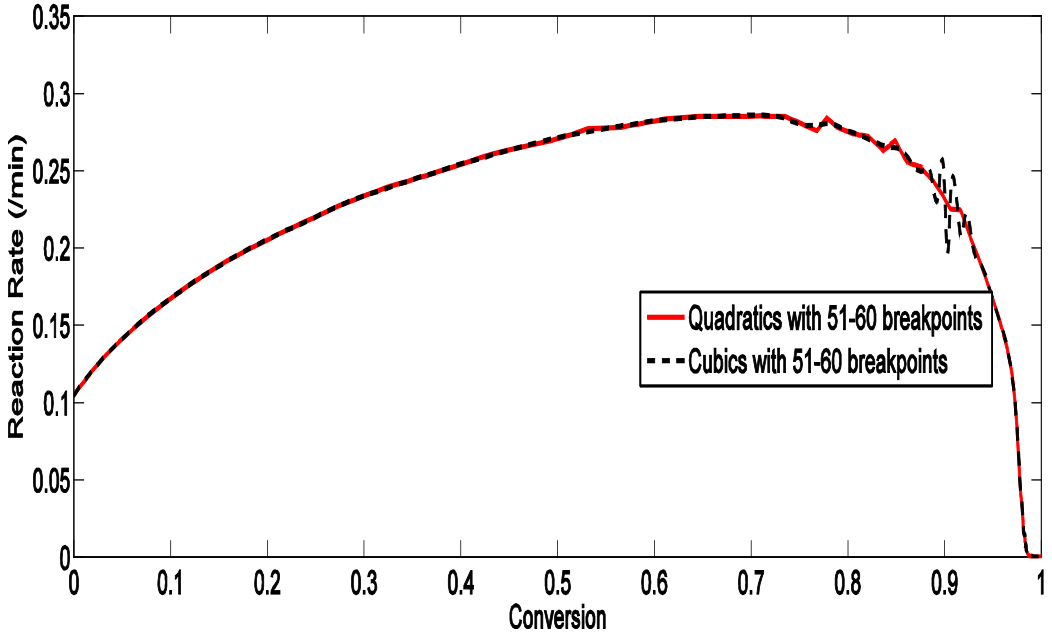

Fig. 2.12 Comparison of cubic spline and B-spline data interpolation on corn stover biochar (particle size = 1.5 mm, pyrolysed under 0.1℃/sec 600℃ 1 hour) combustion temperature = 550 ℃, O_2=21%

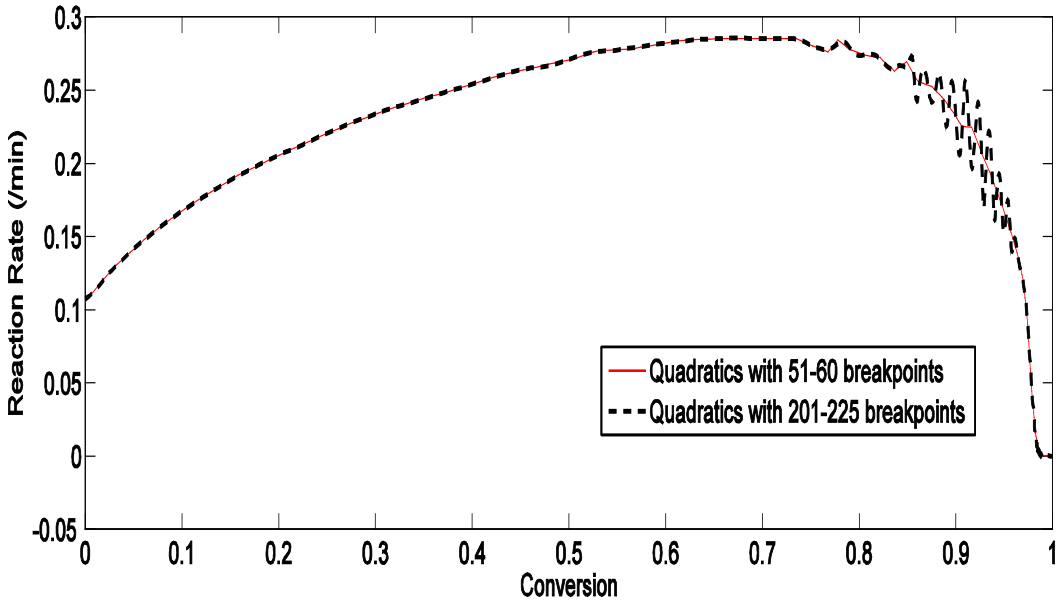

Figure 2.13 Comparison of the influences of different breakpoints number on B-spline data interpolation on corn stover biochar (particle size = 1.5 mm, pyrolysed under 0.1℃/sec 600℃ 1 hour) combustion temperature = 550 ℃, O_2=21%

CHAPTER 3

Biochar chemical and physical characterization

3.1 Overview

Using my computer-controlled pyrolysis reactor, I generated a library of biochars from two different feedstocks (corn stover and apple wood) by varying several operating conditions (see Table 3.1) that I hypothesized were significant controls on the chemical composition and pore structure of the produced biochars.

In agreement with earlier literature studies, I found that the biomass feedstock and the final heat treatment temperature (HTT) are major controls on biochar properties. For both feedstocks, higher HTT values led to biochars with larger clusters of aromatic rings and larger microporosities or micropore surface areas. However, I also found that HTT is not the only control of final properties. Particle size, the pyrolysis heating rate and the duration of the pyrolysis process also had significant effects on the chemical and pore structure of produced biochars. Moreover, the pyrolysis conditions did not always have the same effect on the properties of biochars produced from corn stover or apple wood. For both feedstocks, the size of aromatic ring clusters and the microporosity increased with decreasing particle size. However, the pyrolysis heating rates affected differently the biochars produced from corn stover and apple wood. A slower heating rate led to larger clusters of aromatic rings and larger microporosities for apple wood biochars, while the opposite effect of heating rate was observed for biochars produced from corn stover.

Table 3.1:

Feedstocks and operating conditions used for preparing our biochar library

PARAMETER	VALUES	
Feedstock	Apple Wood	Corn Stover
Final Heat Treatment Temperature (HTT), °C	450	600
Pyrolysis Heating Rate, °C/s	0.1	1.0
Particle size, mm	1.5	0.25
Duration of treatment at final HTT, min	60 (*)	

(*) Four samples were cooled immediately after reaching the final HTT

3.2 Kinetics of pyrolysis reactions

The rate of the biomass pyrolysis reaction increases sharply and reaches maxima at around 350℃. Then the rate dropped at around 500℃. Biomass pyrolysis starts with lignin pyrolysis, then the shoulder peak at a low temperature represents the decomposition of the thermally labile hemicellulose and the highest peak (the maximum pyrolysis rate) is due to cellulose decomposition. Finally, the tailing at high temperatures is due to lignin decomposition since it decomposes slowly, which was reacting throughout the devolatilization process [131, 132]. By comparing with different choices of bspline order, I choose quadratics 51 breakpoints, which gives the best spline quality (Figure 3.1-3.4). For apple wood pyrolysis, the loss of volatiles occurred in two stages: 250°C –450°C and 450°C –600°C (Figure 3.2); for corn stover pyrolysis, the loss of volatiles occurred in one stages: 250°C –600°C (Figure 3.4), which is due to different hemicellulose-cellulose-lignin compositions in apple wood and corn stover.

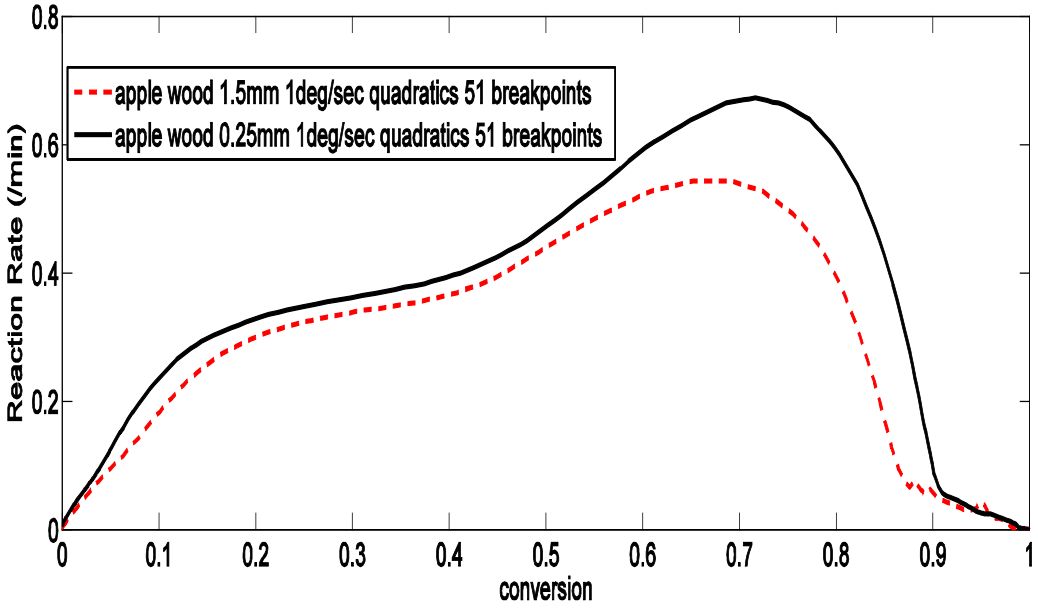

Figure 3.1 The reaction rate of mass loss .vs. conversion plot of different particle size apple wood pyrolysis reaction. The measurements using heating rates of 1 °C /sec apple wood.

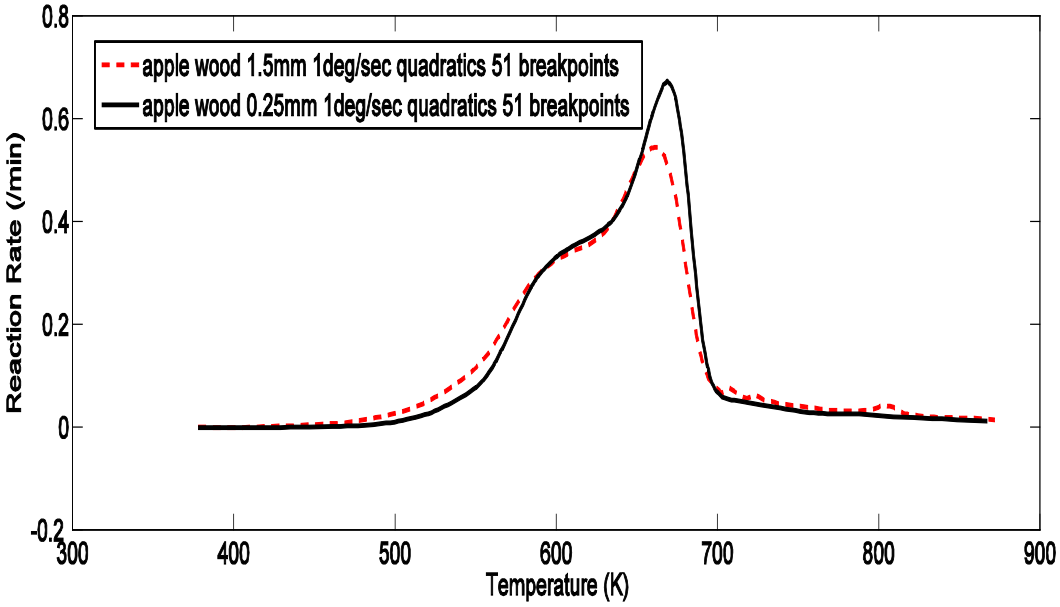

Figure 3.2 The reaction rate of mass loss temperature plot of different particle size apple wood pyrolysis reaction. The measurements using heating rates of 1 °C/sec apple wood.

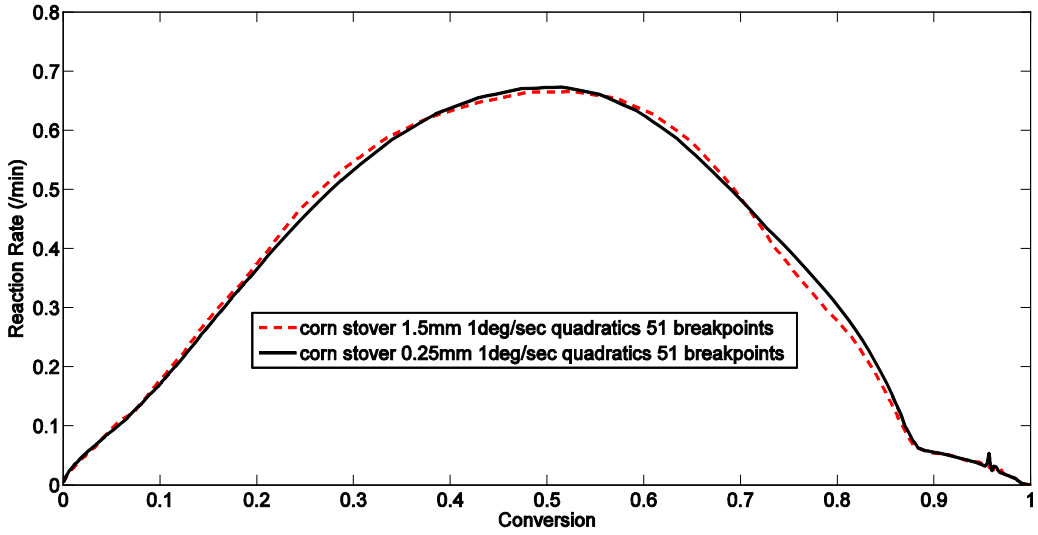

Figure 3.3 The reaction rate of mass loss .vs. conversion plot of different particle size corn stover pyrolysis reaction. The measurements using heating rates of 1 °C/sec corn stover.

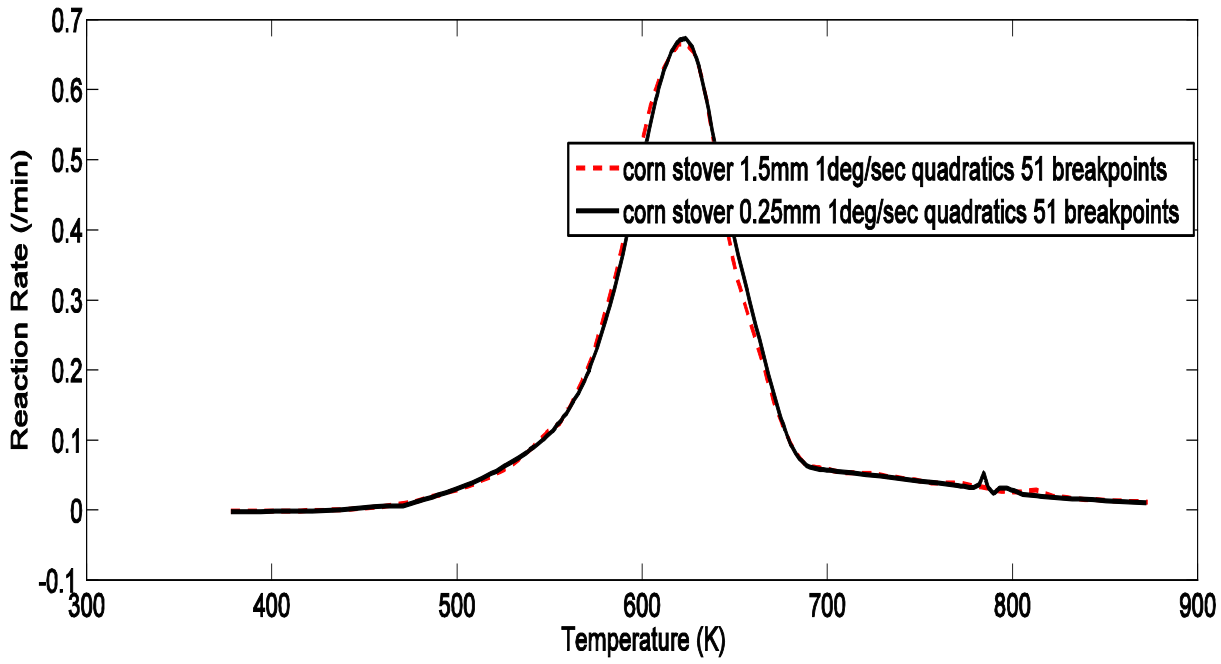

Figure 3.4 The reaction rate of mass loss .vs. temperature plot of different particle size corn stover pyrolysis reaction. The measurements using heating rates of 1 °C/sec corn stover.

Thus, I can write Eq. (2.10) as

$$\frac{dx}{dt} = A\exp(-\frac{E}{RT})(1-x)^n \tag{3.1}$$

In order to determine the reaction order n, equation (3.1) is rearranged by taking the ln of both sizes. When plotting $\ln(\frac{dx}{dt})$ vs. $\ln(1-x)$, the slope should give the reaction order n. According to equation (3.1), a plot of $\ln[\frac{\frac{dx}{dt}}{(1-x)^n}]$ versus $\frac{1}{T}$ corresponds to a straight line with a slope of $(-\frac{E}{R})$ for a certain value of n and $\ln(A)$ is the intercept. For a solid-state organic decomposition, the plausible assumption is first-order elementary reactions [133].

The apparent activation energy and the pre-exponential factor for biomass pyrolysis process are given in Table 3.2. The extent of difficultness of the pyrolysis process of different biomass feedstock can be compared from kinetic parameters. The larger the activation energy, the slower the pyrolysis process of that biomass feedstock under the same temperature level is, which means the more difficult the pyrolysis process is. Moreover, the activation energy usually does not work over a wide temperature range (0-600 °C), making it important not to extrapolate the data.

Table 3.2 Apparent activation energy and pre-exponential factor for biomass pyrolysis process

Biomass sample	Heating rate	Apparent activation energy, E (kJ/mol)	pre-exponential factor, $\log_{10}(A)$ (min^{-1})
1.5mm	6 °C/min	74.836	7.5133
Apple wood	10 °C/min	84.64	8.6425
0.25mm	6 °C/min	88.678	8.903
Apple wood	10 °C/min	84.601	8.599
1.5mm	6 °C/min	76.690	7.7739
Corn stover	10 °C/min	70.519	7.2527
0.25mm	6 °C/min	74.705	7.5567
Corn stover	10 °C/min	66.786	6.9053

In order to better understand the biomass pyrolysis process, I repeat the exact pyrolysis conditions in the TGA. After deducting the moister contents, the temperatures at 1%, 5%, 95% and 99% of weight loss are 189°C, 242°C, 458°C and 574°C.

Kinetics parameters of primary and secondary decomposition reactions are taken directly from the literature [134-136] (Table 3.3-3.4).

Table 3.3 Kinetic parameters of woody biomass pyrolysis process[134-136]

reaction	1	2	3
A_i (s^{-1})	$2*10^{10}$	$2.51*10^{7}$	$1.38*10^{10}$
E_i (J mol^{-1})	148000	117000	161000
$\triangle h_i$ (J kg^{-1})	110000	0	-210000

The convective heat transfer between biomass particle and environment is given by Nusselt's number:

$$Nu = \frac{h_{conv} 2r}{\lambda_g} = 2 + 0.6 \,\mathrm{Pr}^{\frac{1}{3}} \,\mathrm{Re}^{0.5} \tag{3.2}$$

where Pr is the Prandtl number, $\mathrm{Pr} = \frac{C_{pg}\mu_g}{\lambda_g}$ and Re is the Reynolds number, $\mathrm{Re} = \frac{\rho_g V 2r}{\mu_g}$. For the stagnant flow:

$$h_{conv} = \frac{\lambda_g}{r} \tag{3.3}$$

The Biot number, Bi, for a biomass particle determines whether the conduction of heat within a particle is faster than the transport of heat to the exterior of the particle from the reactor.

$$Bi = \frac{r h_{conv}}{\lambda_b} = \frac{\lambda_g}{\lambda_b} \tag{3.4}$$

<0.1 will result in an almost uniform temperature throughout the particle. So the internal heat transfer is negligible.

Table 3.4 Thermophysical properties of nitrogen gas and woody biomass[134-136]

Property	Value	Unit
nitrogen gas specific heat	C_{pg}= 1090	J kg^{-1} K^{-1}
Thermal conductivity of the nitrogen gas	λ_g= 0.02598	Wm^{-1} K^{-1}
woody biomass specific heat	C_{pb}= 1500+T	J kg^{-1} K^{-1}
Intermidate solid specific heat	C_{pi}= 1500+T	J kg^{-1} K^{-1}
Tar specific heat	C_{pt}=-100+4.4*T-1.57*10^{-3}*T^2	J kg^{-1} K^{-1}
Gas specific heat	C_{pg}=770+0.629T-1.91*10^{-4}*T^2	J kg^{-1} K^{-1}
Volatile specific heat	C_{pv}=0.15*C_{pg}+0.85*C_{pt}	J kg^{-1} K^{-1}
woody biochar specific heat	C_{pc}=420+2.09*T+6.85*10^{-4}*T^2	J kg^{-1} K^{-1}
Thermal conductivity of the woody biomass	λ_b= 0.3 or 0.13+(T-273)*3*10^{-4}	Wm^{-1} K^{-1}
Thermal conductivity of the woody biochar	λ_c= 0.25 or 0.08-(T-273)*10^{-4}	Wm^{-1} K^{-1}
Initial density of woody biomass	ρ=650	kg m^{-3}
Initial mass of woody	m_{b0}=0.28*10^{-3}	kg

biomass		
Final mass of woody biochar	$m=0.06*10^{-3}$	kg

Since there is a thermocouple directly inserted in the geometrical center of the small reactor crucible to measure the exact pyrolysis temperature, we can develop a model for our system for the heat and mass transfer process. I assume:

(1) Biomass is in the form of spherical particles.

(2) The temperature is uniform throughout the biomass particles during the pyrolysis.

(3) The volume of the biomass particle does not shrink as it heats up.

(4) The heat convection of volatiles is negligible.

I demonstrate this by considering the simple case of sequential chemical reactions:

$$\text{Biomass} \longrightarrow \text{Unreacted Residue} + \text{Water}$$

$$\text{Unreacted residue} \xrightarrow{k_1} \text{Volatiles}$$

$$\text{Unreacted residue} \xrightarrow{k_2} \text{Intermediate solid} \xrightarrow{k_3} \text{Biochar}$$

This reaction scheme is a “sub-network” of the many pyrolysis models that have been proposed [132, 134].

The environmental temperature is guaranteed to increase from the room temperature by a constant linear heating rate, β:

$$T_e = T_0 + \beta t \tag{3.5}$$

According to the above biomass pyrolysis reactions, mass conservation is as following:

$$\frac{\partial m_b}{\partial t} = -(k_1 + k_2) m_b \tag{3.6}$$

$$\frac{\partial m_i}{\partial t} = k_2 m_b - k_3 m_i \tag{3.7}$$

$$\frac{\partial m_c}{\partial t} = k_3 m_i \tag{3.8}$$

$$\frac{\partial m_v}{\partial t} = k_1 m_b \tag{3.9}$$

Heat transferred across the biomass particles is used to increase the samples' temperature and is consumed for pyrolysis heat. Therefore, the external heat transfer flux balance at the biomass particles' surface can be written as:

$$h A_r(T_e - T_s) = m_b c_{pb} \frac{\partial T_s}{\partial t} + m_i c_{pi} \frac{\partial T_s}{\partial t} + m_c c_{pc} \frac{\partial T_s}{\partial t} + m_v c_{pv} \frac{\partial T_s}{\partial t} + \Delta H_1 \frac{\partial m_v}{\partial t} + \Delta H_2 \frac{\partial m_i}{\partial t} + \Delta H_3 \frac{\partial m_c}{\partial t} \tag{3.10}$$

The number of biomass particles is:

$$n = \frac{m_0}{\rho \frac{4}{3} \pi r^3} \tag{3.11}$$

The total heat transfer specific area is:

$$A_r = n 4 \pi r^2 \tag{3.12}$$

where m_b is the biomass mass, m_i is the intermediate solid mass, m_c is the biochar mass, m_v is the volatile mass, h is the heat transfer coefficient, A_r is the surface area for heat transfer, m_{b0} is the initial mass of the biomass sample measured at initial room temperature, T_0, c_{pb} is the woody biomass specific heat. The assumption of constant hA_r in (3.10) is illustrated before in the literatures [137-139]. I assume the biomass particles number and radius do not change. So their volumes and surface areas remain constant. However, their densities and masses decline during the pyrolysis. The gas flux leaving the biomass particle during heating up will influence the value of the heat transfer coefficient h. But I neglect it since it is minor.

The initial conditions are determined by considering the water evaporation process: $T_s = T_0 = 378K$, $m_b = 0.9m_{b0}$, $m_v = m_i = m_c = 0$ at $t = 78 + t_{vap}$ Integration of the material and energy balances (system of ODEs) yields the following temperature histories for the two biomass particles of Figure 3.5.

When the heating rate is 1°C /sec (typical conditions for this study), T environment is nearly the same as T surface apple wood 0.25mm. The temperature lags between T surface apple wood 0.25mm and T surface apple wood 1.5mm is nearly 15°C (Figure 3.5) as it is heated to the final temperature. The deviations from the temperature program increase expontentially with increasing particle size and increasing heating rates, a well-known result from system dynamics theory and disappear only after the temperature program moves from the heating ramp to the constant temperature stage. By changing m_{b0} to half its value to indicate the mass changes in the pyrolysis process, it seems no effect from mass to the plot (Figure 3.5) at all with heating rate keeps at 1°C /sec.

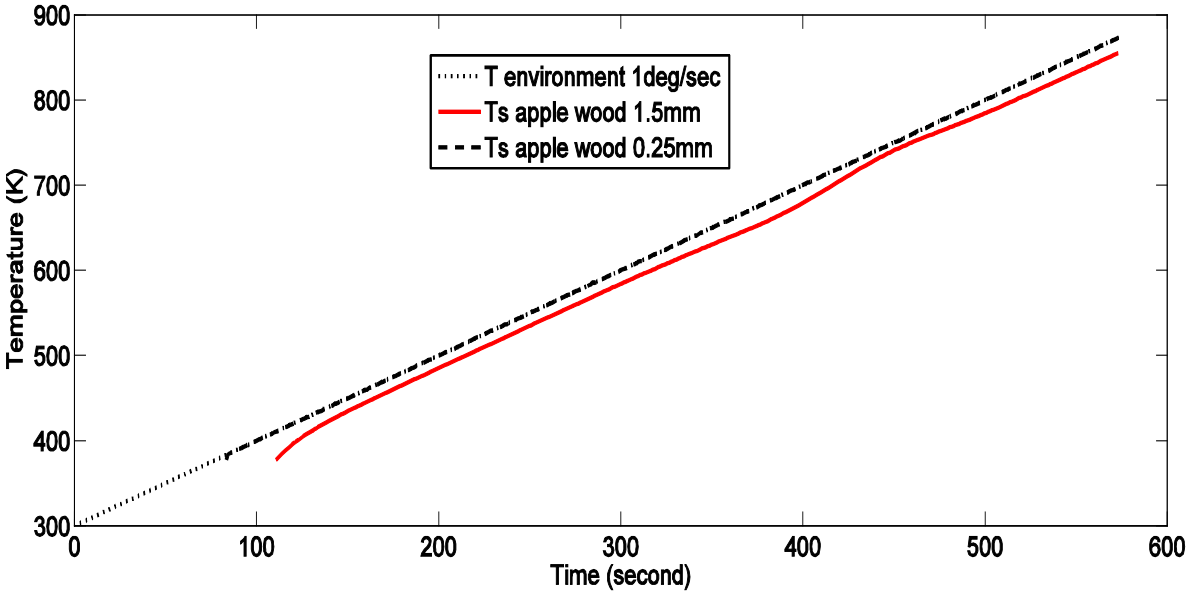

Figure 3.5 Temperature lags during the heating of two biomass particles with different sizes and heat effects

In practice, the temperature lags will be larger than estimated here because the thermal conductivity of the biomass is not high enough to ensure a uniform temperature across the particle. Moreover, the thermal conductivity will decrease as the pyrolysis reactions proceeds and the particle become more porous, further increasing the temperature differences between the surface and the center of pyrolyzing particles. All these are real situations, which are neglected in our assumptions due to simplicity.

I also generate the different components mass-temperature plots (Figure 3.6). It is clear that different particle sizes cause different components generating history even under the same pyrolysis conditions.

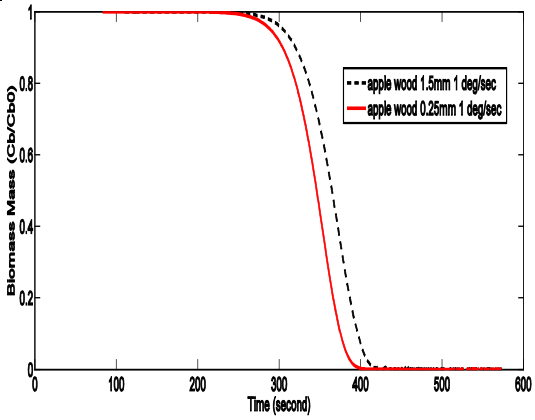

Figure 3.6 (a)
Mass of unreacted residues
for the two runs of Figure 3.5

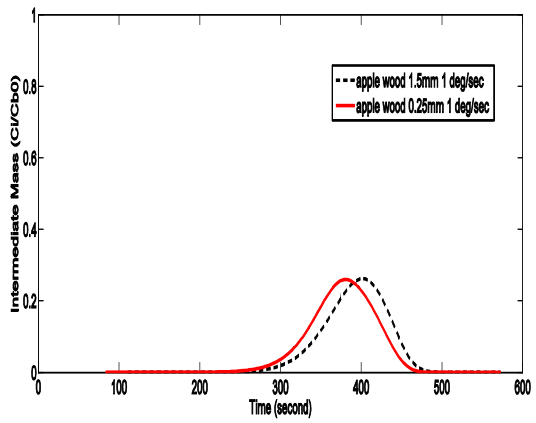

Figure 3.6 (b)
Mass of intermediate solid
for the two runs of Figure 3.5

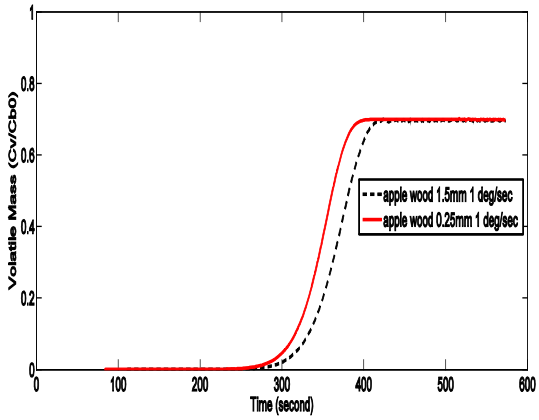

Figure 3.6 (c)
Mass of volatiles
for the two runs of Figure 3.5

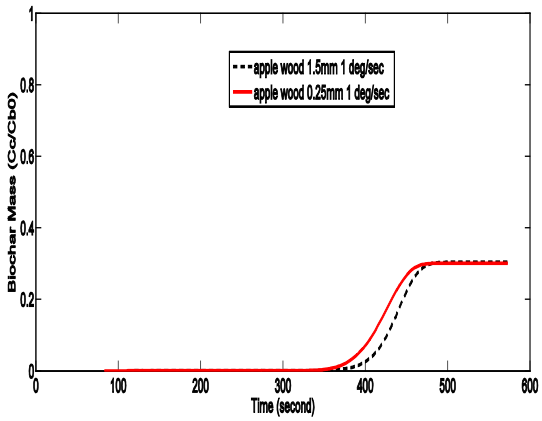

Figure 3.6 (d)
Mass of biochar
for the two runs of Figure 3.5

I also consider the case of two particles 1.5 mm in diameter made of different biomass feedstocks. The same consecutive reactions take place in both particles, but the activation energies of the reactions in the second case are 10% higher than the activation energies of the first case. As expected, the temperature lags increases with a higher activation energy (more difficult reactions) and, thus, the temperature histories $T_{pi}(t)\Big|_0^{t_f}$, $i=1,2$ of the two particles are different (Figure 3.7).

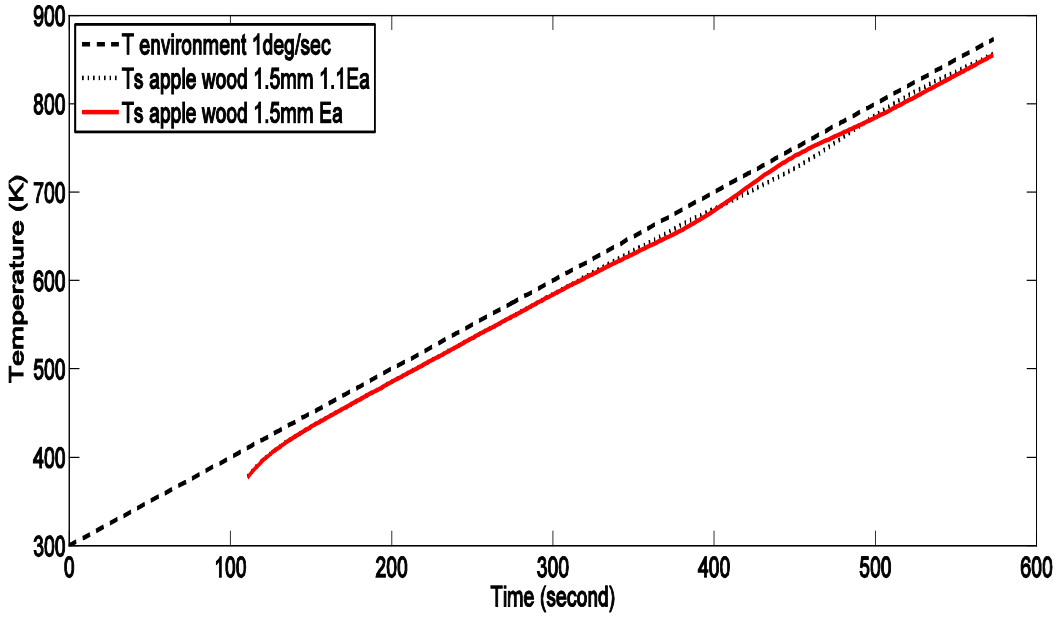

Figure 3.7 Temperature lags during the heating of two biomass particles with equal sizes (1.5 mm) but different reaction kinetics

The important observation to make here, however, involves the estimated mass of the components' unreacted residues, intermediate solid, volatiles and biochar at the time that the simulation is stopped. By t = 400 s, unreacted residues have completely disappeared (Figure 3.8 (a)) and the intermediate solid has passed its maximum mass and is reacting fast to produce the final product biochar (Figure 3.8 (b,d)).

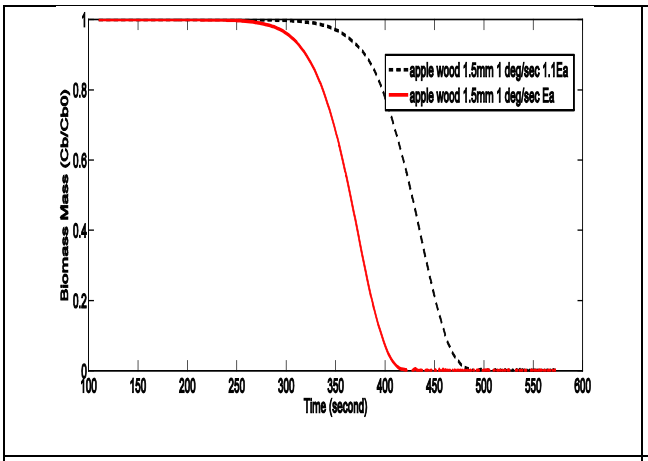

Figure 3.8 (a)
Mass of unreacted residues
for the two runs of Figure 3.7

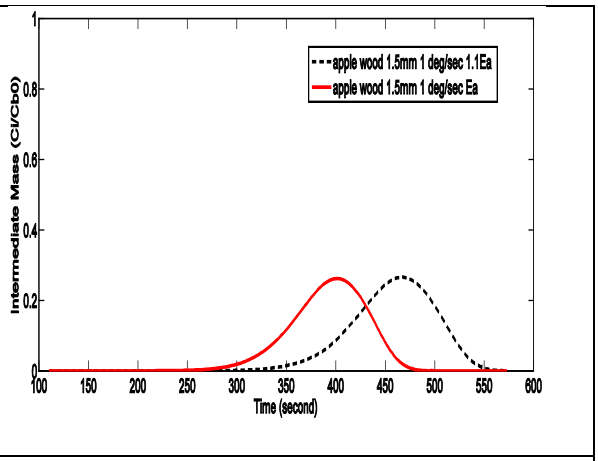

Figure 3.8 (b)
Mass of intermediate solid
for the two runs of Figure 3.7

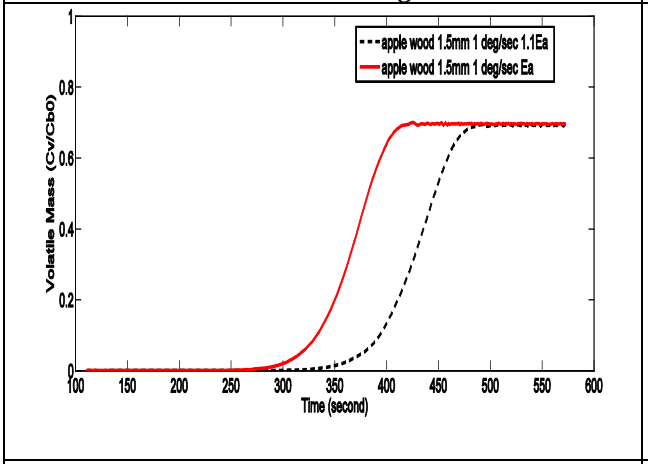

Figure 3.8 (c)
Mass of volatiles
for the two runs of Figure 3.7

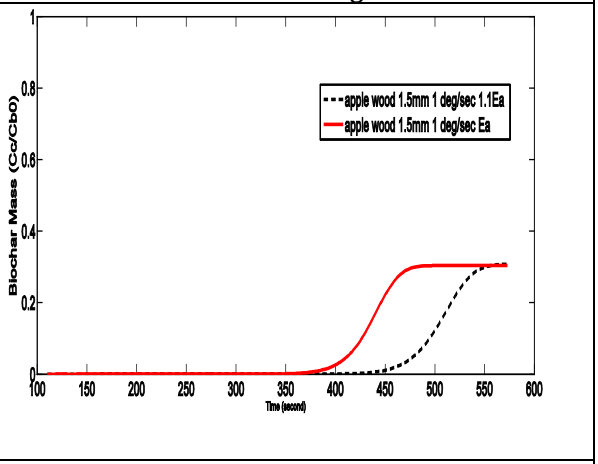

Figure 3.8 (d)
Mass of biochar
for the two runs of Figure 3.7

On the other hand, chemical reactions proceed more slowly in particle 2. As a result, unreacted residues have not completely disappeared until 500 s of reaction time (Figure 3.8 (a)) and the intermediate solid has not yet reached its maximum concentration. Production of the final product biochar is slower than that of particle 1 (Figure 3.8 (d)).

It is clear from the previous analysis that the temperature history $T_p(t)\Big|_0^{t_f}$ of a biomass particle is influenced by (a) the chemical composition of the biomass feedstocks, (b) the physical properties of the biomass (heat capacity, thermal conductivity etc.) that change as the pyrolysis

reaction proceeds, (c) the particle size and (d) process conditions like the final heat treatment temperature, pyrolysis heating rate, and duration of treatment at the final temperature.

Thus, the final chemical and pore structure of a biochar will depend upon the complete temperature history $T_p(t)\Big|_0^{t_f}$ of the biomass particles, from t = 0 when heating begins until the final time t_f when the particle temperature has cooled down again and all reactions have stopped.

3.3 Elemental Analysis

The biochar C/H mass ratio increased with increasing HTT (Table 3.5). The pyrolysis heating rate and the particle size also influenced the C/H atomic ratio, but to a lesser extent than HTT (Table 3.5). The increases in the C/H ratio came primarily from hydrogen mass losses. We observed a 94% H mass loss at 450^{o}C, and 95% H mass loss at 600^{o}C for both corn stover and apple wood biochars. This implies that the thermal cracking reactions responsible for the losses of volatiles and tars are nearly complete when our feedstocks are pyrolyzed at a final HTT of 450°C. Table 3.6 compares the C/H ratios of chars produced by raising the reactor temperature to 600°C and, then, either (a) cooling the reactor immediately or (b) keeping it at 600°C for 60 min at the final HTT of 600°C. Corn stover chars cooled immediately after reaching 600°C had C/H atomic ratios equal to 1.8 if heated at 0.1°C/s, and 1.4 if heated at 1°C/s. The corresponding chars that were kept at 600 °C for one hour had C/H ratios equal to 4.3 (0.1°C/s) and 4.6 (1°C/s). Similar behavior was observed for the apple wood chars. The standard errors of the calculated C/H atomic ratios for the 22 samples of Tables 3.2 and 3.3 had an average value of 0.13. Finally, Tables 3.5 and 3.6 show that our biochars retained 30-40% of the carbon present in the original

biomass, with apple wood retaining more than corn stover. Similar fixed-carbon yields have been reported in the literature [140, 141].

Table 3.5:

Elemental Composition Data for Biochar Library

All sixteen biochar samples were maintained for 60 min at the final HTT

HTT (°C)	Particle Size (mm)	Heating Rate (°C/s)	N (wt %)		C (wt %)		H (wt %)		Fraction of Original Biomass C Remaining in Biochar (wt %)		C/H Atomic Ratio	
			Apple Wood	Corn Stover	Apple Wood	Corn Stover	Apple Wood	Corn Stover	Apple Wood	Corn Stover	Apple Wood	Corn Stover
600	1.5	0.1	0.4	0.6	75.1	67.7	1.4	1.3	36.6	33.6	4.6	4.3
		1.0	0.4	0.6	72.4	66.0	1.1	1.2	35.2	32.7	5.3	4.6
	0.25	0.1	0.4	0.5	76.9	63.9	1.3	1.1	37.5	31.6	5.0	4.8
		1.0	0.4	0.6	75.4	62.0	1.3	1.2	36.7	30.7	4.9	4.4
450	1.5	0.1	0.5	0.7	70.6	65.7	1.7	1.6	34.4	32.6	3.5	3.3
		1.0	0.5	0.7	72.0	66.5	1.9	1.7	35.0	33.0	3.1	3.3
	0.25	0.1	0.5	0.7	80.8	64.8	1.9	1.5	39.4	32.1	3.6	3.6
		1.0	0.6	0.7	81.7	81.7	2.2	2.2	39.8	33.0	3.1	3.1
Original Biomass			**0.2**	**0.7**	**45.2**	**44.4**	**6.3**	**6.1**	**---**	**---**	**0.6**	**0.6**

Table 3.6:

Elemental Composition Data for Biochar Library:

The effect of duration of treatment at the final HTT

For all chars: Final HTT = 600ºC; particle size =1.5 mm.

Time at final HTT (min)	Heating Rate (ºC/s)	N (wt %)		C (wt %)		H (wt %)		Fraction of Original Biomass C Remaining in Biochar (wt %)		C/H	
		Apple Wood	Corn Stover	Apple Wood	Corn Stover	Apple Wood	Corn Stover	Apple Wood	Corn Stover	Apple Wood	Corn Stover
60	0.1	0.4	0.6	75.1	67.7	1.4	1.3	36.6	33.6	4.6	4.3
	1.0	0.4	0.6	72.4	66.0	1.1	1.2	35.2	32.7	5.5	4.6
0	0.1	0.7	0.9	80.4	71.6	4.3	3.2	39.0	35.0	1.6	1.8
	1.0	0.6	0.8	80.3	71.7	5.0	4.2	39.0	36.0	1.3	1.4

3.4 Bulk Organic Chemical Structure

^{13}C solid state NMR is useful in quantifying the organic functional groups of carbonaceous solids [125]. In addition, spectral editing techniques (like dipolar-dephasing) provide more detailed information about the chemical structure of biochars [64, 73].

As biochar pyrolysis temperature increases, the range in signal distribution of the spectra decreases, due mainly to the loss of intensity in signals related to cellulose, and also due to a dramatic increase in overall aromaticity [40, 142]. At lower pyrolysis temperatures NMR spectra

show remaining plant functional groups in the alkyl and O-alkyl regions. At higher temperatures, however, signals collapse to a broad peak near 130 ppm, which is assigned to aromatic structures [40, 142].

We used dipolar-dephasing NMR techniques to estimate the aromatic cluster size and the extent of cross-linking between clusters in our biochars. Aromatic carbon cluster size was strongly affected not only by the final heat treatment temperature (HTT), but also by the feedstock particle size and heating rate. The aromatic domains in apple wood biochars produced at a final HTT of 450°C consisted of clusters with about 15 aromatic carbon atoms, while the average number of aromatic carbon atoms per cluster increased to about 19 for apple wood biochars produced at a HTT of 600°C (Table 3.7). For both biomass feedstocks, smaller particle sizes led to biochars with larger clusters of aromatic carbon (lower part of Table 3.7). The heating rate also affected cluster size, with a slower heating rate producing larger ring clusters. The clusters in apple wood-biochars produced at 1°C/s contained 16 carbon atoms, while the average number of carbon atoms per cluster increased to 19 for apple wood biochars produced at 0.1°C/s (see data in lower part of Table 3.7). However, we did not observe the same effect of heating rate on biochars produced from corn stover. For these biochars, increasing the heating rate from 0.1 to 1 °C/s did not significantly change the number of aromatic carbons per cluster (see data in lower part of Table 3.7).

We hypothesize that the observed effects of particle size and heating rates on the chemical structure of chars are due to the different chemical compositions of our feedstocks, which result in significant differences in the kinetics of the pyrolysis reactions [131, 132, 143]. In addition to the heating rate, the size and heat capacity of a biomass particle will also affect the thermal lag [143]

observed during rapid heating of the particle and, hence, the final extent of pyrolysis reactions and degree of aromatic ring condensation.

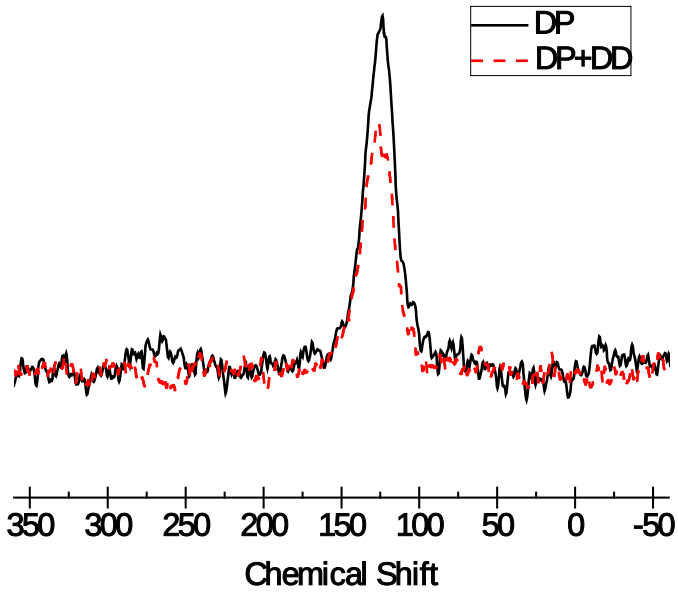

Figure 3.9 ^{13}C direct polarization spectra (DP – solid line) and direct polarization with dipolar dephasing spectra (DP+DD – dash line) for an apple wood biochar. The sample was ground to 1.5 mm, heated at 0.1°C/s to 600°C and held at 600°C for 1 hour.

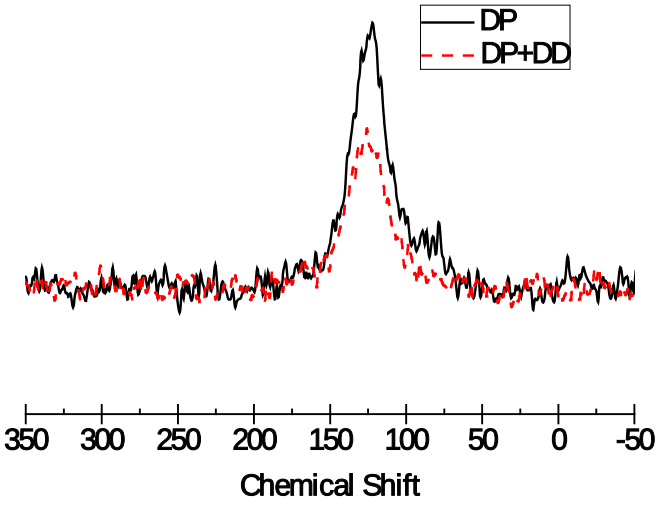

Figure 3.10 ^{13}C direct polarization spectra (DP – solid line) and direct polarization with dipolar dephasing spectra (DP+DD – dash line) for a corn stover biochar. The sample was ground to 1.5 mm, heated at 0.1°C/s to 600°C and held at 600°C for 1 hour.

Table 3.7

Number of aromatic carbons per cluster determined by DP and DP+DD ^{13}C NMR.

The reproducibility of ring cluster size measurements is ±1.

All samples were kept for 60 min at the final HTT

Effect of final heat treatment temperature (HTT)				
HTT (ºC)	Feedstock	Particle Size (mm)	Heating Rate (ºC/s)	Aromatic C per Cluster
450	Apple Wood	1.5	0.1	15
450	Corn Stover	0.25	0.1	15
600	Apple Wood	1.5	0.1	19
600	Corn Stover	0.25	0.1	20
Effect of feedstock, particle size, heating rate				
HTT (ºC)	Feedstock	Particle Size (mm)	Heating Rate (ºC/s)	Aromatic C per Cluster
600	Apple Wood	1.5	0.1	19
	Corn Stover	1.5	0.1	15
	Apple Wood	1.5	1.0	16
	Corn Stover	1.5	1.0	16
	Apple Wood	0.25	1.0	19
	Corn Stover	0.25	0.1	20

3.5 X-ray photoelectron spectroscopy (XPS)

Surface chemistry and pore structure act together to determine the adsorption performance of biochars, making it important to chemically characterize the surface chemical composition of biochars produced under a variety of pyrolysis conditions. The XPS wide-scan survey spectra were dominated by the carbon peak (C1s) at 284.5eV and the oxygen (O1s) peak at 533 eV, with smaller peaks corresponding to N, K, Ca, and Mg. Sample XPS spectra are provided in the Supporting Information.

There were clear effects of feedstock on the wide-scan XPS results. Similar to combustion elemental analysis, wide-scan XPS results showed that apple wood biochars had more C and less O than corn stover biochars (Table 3.8). XPS wide-scan spectra also showed that the metal content of corn stover biochar was greater than apple wood.

I saw effects on surface functional groups due to production conditions only in two cases. First, for the largest corn stover particles (1.5 mm) heated to 600°C at 0.1 °C/s, I saw approximately a doubling of C=O functionality, from an average of 7±1% to 14%. This was accompanied by a decrease of similar magnitude in the sum of C=C, C-C, and C-H functionalities. Second, the smaller corn stover particles heated to 600°C at both rates were lower in C-O functionalities by more than a factor of 2 compared to all other samples (see Table 3.9). Regardless of production conditions, all values for functionalities containing oxygen were low compared to environmentally exposed charcoals [144].

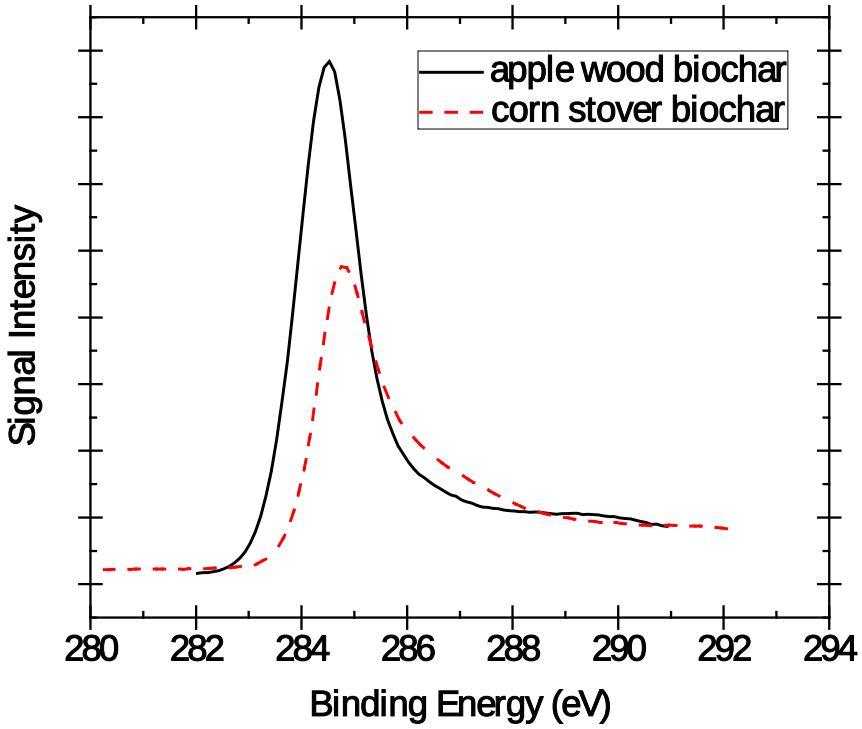

Figure 3.11 C1s XPS spectra for an apple wood biochar (solid line) and a corn stover biochar (dash line). Both samples were ground to 1.5 mm, heated at 0.1°C/s to 600°C and held at 600°C for 1 hour.

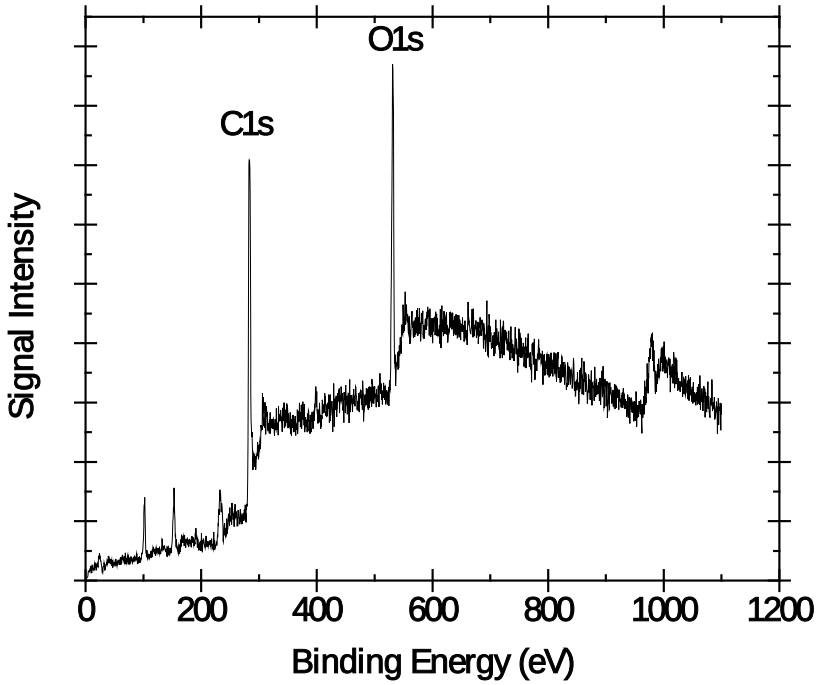

Figure 3.12: **XPS survey spectrum for an apple wood biochar. The sample was ground to 1.5 mm, heated at 0.1°C/s to 600°C and held at 600°C for 1 hour.**

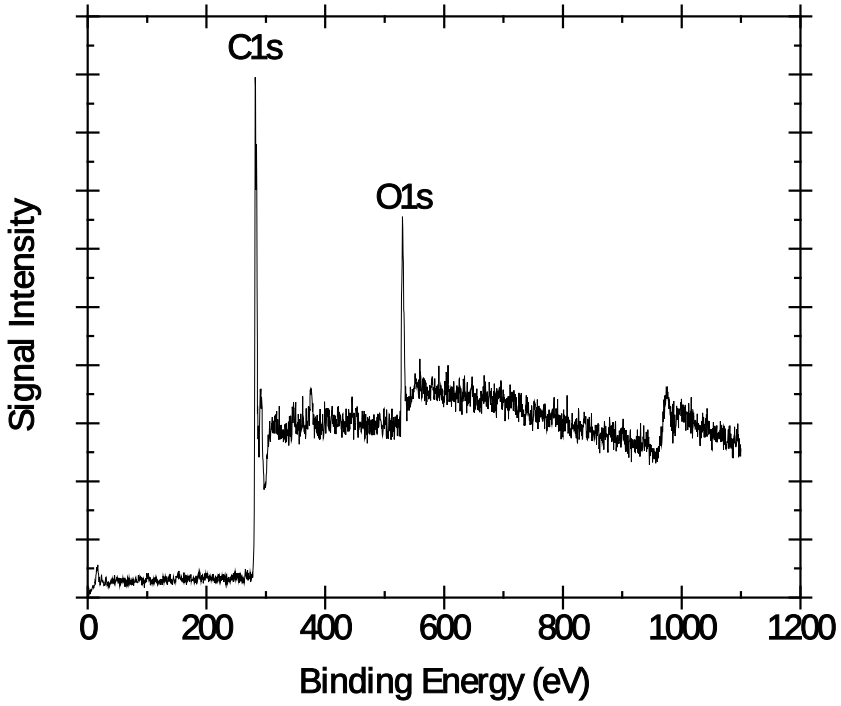

Figure 3.13: **XPS survey spectrum for a corn stover biochar. The sample was ground to 1.5 mm, heated at 0.1°C/s to 600°C and held at 600°C for 1 hour.**

Table 3.8

Atomic elemental contents measured from XPS wide-scan spectra of whole biochar particles

All sixteen biochar samples were maintained for 60 min at the final HTT

HTT (°C)	Particle Size, (mm)	Heating Rate, (°C/s)	C (%)		O (%)		K (%)		Mg (%)		Ca (%)	
			Apple Wood	Corn Stover	Apple Wood	Corn Stover	Apple Wood	Corn Stover	Apple Wood	Corn Stover	Apple Wood	Corn Stover
600	1.5	0.1	85	72	12	20	0	3	0	1	1	1
		1.0	84	83	13	12	0	2	0	0	2	1
	0.25	0.1	88	73	11	20	0	3	0	1	1	1
		1.0	89	79	9	16	0	3	0	1	1	1
450	1.5	0.1	87	74	11	19	0	4	0	0	1	1
		1.0	86	68	12	23	0	4	0	1	2	2
	0.25	0.1	90	74	9	19	0	4	0	1	0	1
		1.0	92	70	7	20	0	3	0	0	1	1

Table 3.9:

Chemical composition (%) of carbon (C1s) from high-resolution XPS spectra of apple wood and corn stover biochar particles

All sixteen biochar samples were maintained for 60 min at the final HTT

HTT (°C)	Particle Size (mm)	Heating Rate (°C/s)	C=C, C-C, C-H (%)		C-O (%)		C=O (%)		COO (%)	
			Apple Wood	Corn Stover	Apple Wood	Corn Stover	Apple Wood	Corn Stover	Apple Wood	Corn Stover
600	1.5	0.1	77	67	15	17	5	14	3	2
		1.0	76	65	15	24	7	8	3	4
	0.25	0.1	77	80	16	8	5	8	2	4
		1.0	78	85	15	5	4	7	2	3
450	1.5	0.1	73	76	20	15	5	7	2	3
		1.0	75	71	19	18	3	8	3	3
	0.25	0.1	81	71	13	19	4	7	2	4
		1.0	77	81	15	13	5	5	3	2

CHAPTER 4

Biochar reactivity and pore structure

4.1 Micropore Structure

The N_2 adsorption/desorption isotherms obtained for all samples belonged to type I of the International Union of Pure and Applied Chemistry (IUPAC) classification [77]. The IUPAC classification of isotherms allows us to quickly identify some key characteristics of the pore structure. Thus, the type of the isotherm reveals that our biochars are very microporous [77] with the vast majority of their pores being smaller than 2 nm. Figure 4.1 shows two typical isotherms obtained for biochar samples prepared from corn stover and apple wood. Both isotherms exhibit a steep rise for small values of P / P_0 and approach a limiting value as $P / P_0=1$, behavior that is typical for predominantly microporous carbons. The plateau of the type I isotherm represents the pores filling up with N_2 adsorbate by a process similar to capillary condensation, rather than a layer-by-layer adsorbate building up on the pore surfaces [76].

Since the apple wood char isotherm plateaus at a higher P / P_0 value compared to the corn stover one, we can conclude that the apple wood char has a larger micropore volume. The isotherms for all corn stover and apple wood chars show considerable hysteresis of the H4 type [77] that extends to the lowest attainable pressures (Figure 4.1). Moreover, the H4 hysteresis loops observed indicates the presence of narrow, slit-like pores [77] . This is consistent with a molecular structure of biochars that consists of a mix of (a) aromatic carbon in an amorphous mass and (b) nanometer-size crystallites composed of graphitic-like layers of aromatic carbon clusters that are arranged turbostratically [59, 61, 145] .

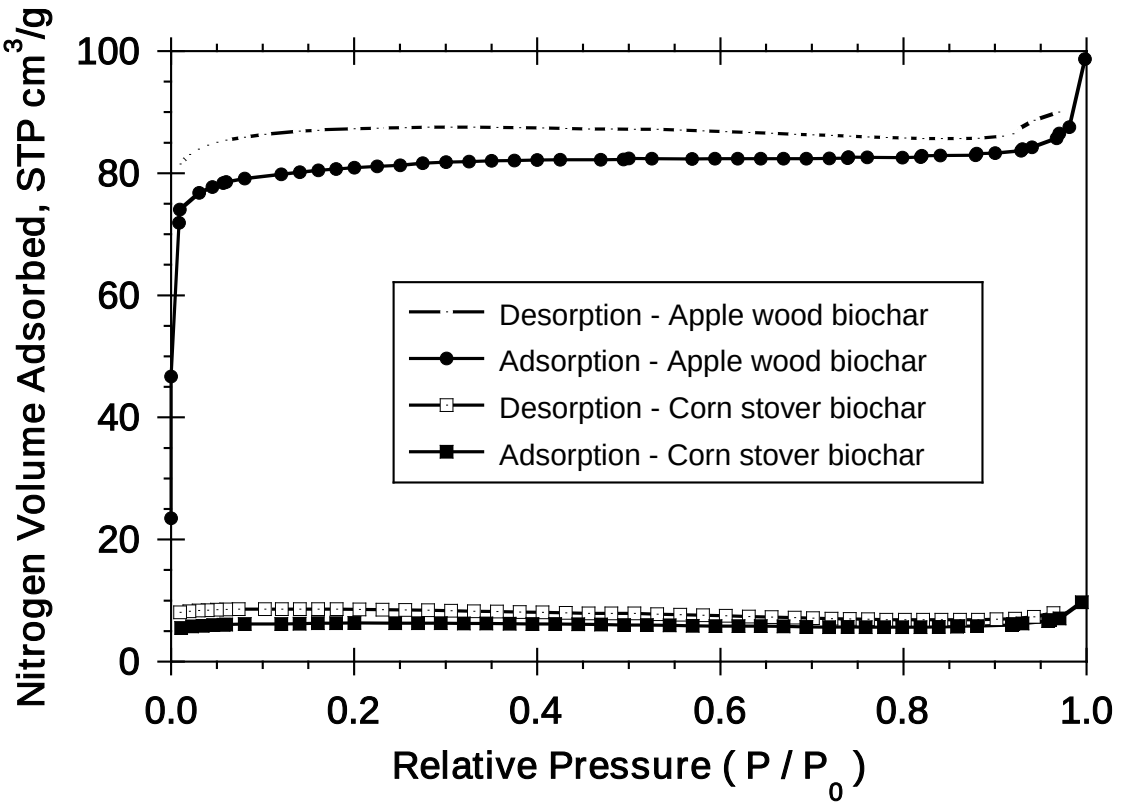

Figure 4.1: Nitrogen adsorption and desorption isotherms for two biochar samples prepared from corn stover and apple wood feedstock. Both biochar samples were prepared using the following conditions: HTT = 600 ºC; duration of treatment at HTT = 60 min; pyrolysis heating rate = 0.1 ºC/s; particle size = 1. 5 mm.

N_2 adsorption/desorption data have been widely used to explore the micropore and mesopore structure of biochars via BET analysis (e.g. [59, 64, 91, 141]). The BET method, however, does not yield accurate values of the actual surface area of microporous solids exhibiting the adsorption/desorption isotherm observed for our chars [76]. For this reason, we also used the Dubinin-Raduskevitch (DR) method to compute the micropore volume from the N_2 adsorption/desorption data (Tables 4.1 and 4.2). Apple wood chars produced at a HTT of 600°C have from 5-10 times the micropore volume of chars produced from corn stover at the same final HTT. These differences are even larger for chars produced at a HTT of 450°C.

I also did 92-point micropore analysis and used the Horvath-Kawazoe method to get the pore size distribution, which is used for slit pore geometry [146]. It takes more than 60 hours to get the micropore analysis for apple biochar, which is due to the restricted diffusion of N_2 into very narrow micropores at low adsorption temperature (77K). The pore size distribution of applewood biochar sample is displayed in Figure 4.2.

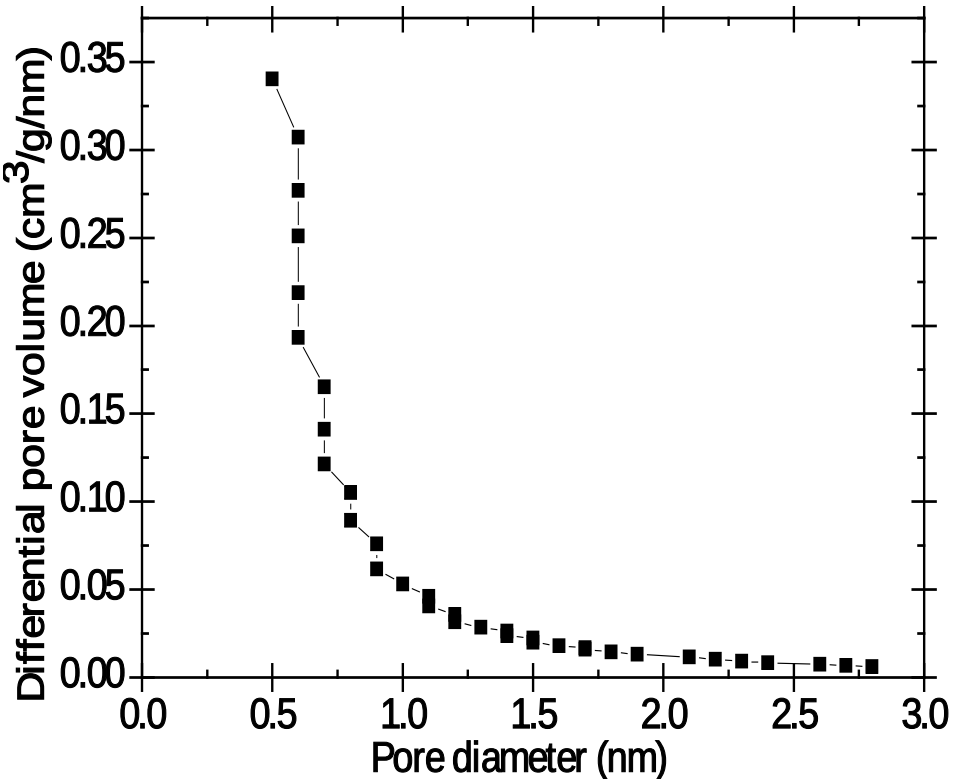

Figure 4.2 Horvath-Kawazoe differential pore volume of biochar samples prepared from apple wood feedstock. The biochar samples were prepared using the following conditions: HTT = 600 ºC; duration of treatment at HTT = 60 min; pyrolysis heating rate = 0.1 ºC/s; particle size = 1. 5 mm.

The data of Tables 4.1 and 4.2 reveal that the particle size and the pyrolysis heating rate are additional controls on the microporosity of the chars. For both feedstocks, small biomass particle sizes gave chars with larger DR and BET micropore volumes and larger BET surface areas. This effect was more pronounced for the corn stover biochars. However, the pyrolysis heating rate had opposite effects on the microporosity of biochars produced from different feedstocks. Apple wood chars produced at 0.1 °C/s had larger DR and BET micropore volumes than chars produced at 1 °C/s. The opposite trend was observed with corn stover chars.

We note here the similar effect of pyrolysis conditions on the microporosity and the size of aromatic clusters. For chars from both feedstocks, the size of aromatic ring clusters and micropore volumes increased with increasing final HTT. Our data (Figure 4.3 and Table 4.1) also show that both the size of aromatic ring clusters and the micropore volume increased with decreasing biomass particle sizes for both feedstocks. However, slower heating rates yielded apple wood biochars with larger aromatic ring clusters and larger micropore volumes, while corn stover chars had smaller aromatic ring clusters and smaller micropore volumes for the slower heating rate.

Table 4.2 provides additional evidence of the importance of reaction kinetics in determining the final structure of biochars by comparing the microporosities of biochars obtained with different heating times at the final HTT temperature of 600°C. For both feedstocks and pyrolysis heating rates, 60 min of heating time at the final HTT of 600°C led to chars with larger micropore volumes and BET surface areas. These results indicate that the evolution of the micropore structure is strongly influenced by the pyrolysis reaction kinetics.

The results of Table 4.2 also indicate that corn stover biochars developed porosity more slowly than apple wood biochars, regardless of the heating rate used. The micropore volumes of

corn stover chars that were cooled immediately after reaching the final HTT of 600°C were 4-5 times smaller than the micropore volumes obtained when the corn stover particles were kept for 60 min at 600°C (Table 4.2). On the other hand, apple wood chars cooled immediately after reaching 600°C had micropore volumes and BET surface areas that were only 30-50% smaller than the corresponding chars that were treated for 60 min at 600 °C (Table 4.2). This leads me to hypothesize that the pyrolysis reaction rates are very different for the two feedstocks because of differences in their chemical composition.

Table 4.2 reveals another subtle difference between apple wood and corn stover biochars. The micropore volumes and BET areas of apple wood chars decrease with increasing heating rate regardless of whether they were kept for 0 or 60 min at the final HTT. This is consistent with a hypothesis that slow heating rates allow more time for the pyrolysis reactions to proceed. With a heating rate of 1 °C/s, approximately 9.6 min are required to raise the temperature of a particle to 600 °C. This time increases to almost 96 min when the pyrolysis heating rate is 0.1 °C/s.

However, the opposite effect of heating rate is observed for corn stover chars, for which faster heating rates produce chars with larger micropore volumes and BET surface areas. This behavior cannot be explained by the reaction kinetics. An additional mechanism must be at play here, like pore blocking by tars [147] or pore deformation due to the larger force with which volatiles are released at the higher heating rates.

Table 4.1:

Micropore volumes and BET surface areas of biochars

All sixteen biochar samples were maintained for 60 min at the final HTT

HTT (°C)	Particle Size (mm)	Heating Rate (°C/s)	DR Micropore Volume (cm^3/g)		BET Micropore Volume (cm^3/g)		BET Surface Area (m^2/g)	
			Apple Wood	Corn Stover	Apple Wood	Corn Stover	Apple Wood	Corn Stover
600	1.5	0.1	0.130	0.010	0.113	0.009	271	21
		1.0	0.110	0.016	0.090	0.012	228	35
	0.25	0.1	0.170	0.017	0.140	0.017	341	34
		1.0	0.155	0.034	0.130	0.032	320	73
450	1.5	0.1	0.040	0.002	0.030	0.002	91	4
		1.0	0.030	0.004	0.030	0.002	71	8
	0.25	0.1	0.082	0.003	0.051	0.003	138	6
		1.0	0.038	0.004	0.027	0.003	83	9

Table 4.2:

The effect of duration of treatment at the final HTT on the micropore volumes and BET surface areas of biochars

For all chars: Final HTT = 600ºC; particle size =1.5 mm.

Time at final HTT (min)	Heating Rate (ºC/s)	DR Micropore Volume (cm^3/g)		BET Micropore Volume (cm^3/g)		BET Surface Area (m^2/g)	
		Apple Wood	Corn Stover	Apple Wood	Corn Stover	Apple Wood	Corn Stover
60	0.1	0.130	0.010	0.113	0.009	271	21
	1.0	0.110	0.016	0.090	0.012	228	35
0	0.1	0.095	*	0.080	*	203	1
	1.0	0.075	0.003	0.060	0.003	160	5

* None detected

4.2 Macropore Structure

Figure 4.3 shows micrographs obtained at 500X and 5000X magnification for four biochar samples produced in our fixed-bed pyrolysis reactor. These micrographs provide strong indication that the biochars have retained major characteristics of the cellular structure of their parent [71, 74, 148]. Apple wood biochars retained the cell wall structure of their biomass precursor with large pores, on the order of 10 μm. The pore structure of the corn stover biochars is characterized by thinner walls and channels with sizes of the order of 1-10 μm. Because of the

regular size and arrangement of plant cells in most woody biomass, the macropores do not have a continuous size distribution. Instead, they consist of discrete groups of pores with very similar sizes and rather regular spatial arrangement [74].

Since the macropores visible in the micrographs of Figure 4.3 are three orders of magnitude larger than the micropores detected by gas adsorption, we can conclude that the macropore surface area is very small when compared to the micropore surface area of biochars [59]. However, macropores account for most of the pore volume of biochars. Because of their size, the large pores are more easily accessible to water [149, 150] and microorganisms [93, 94]. Therefore, macropore structure is probably a major control on many important hydrologic and environmental properties of biochars.

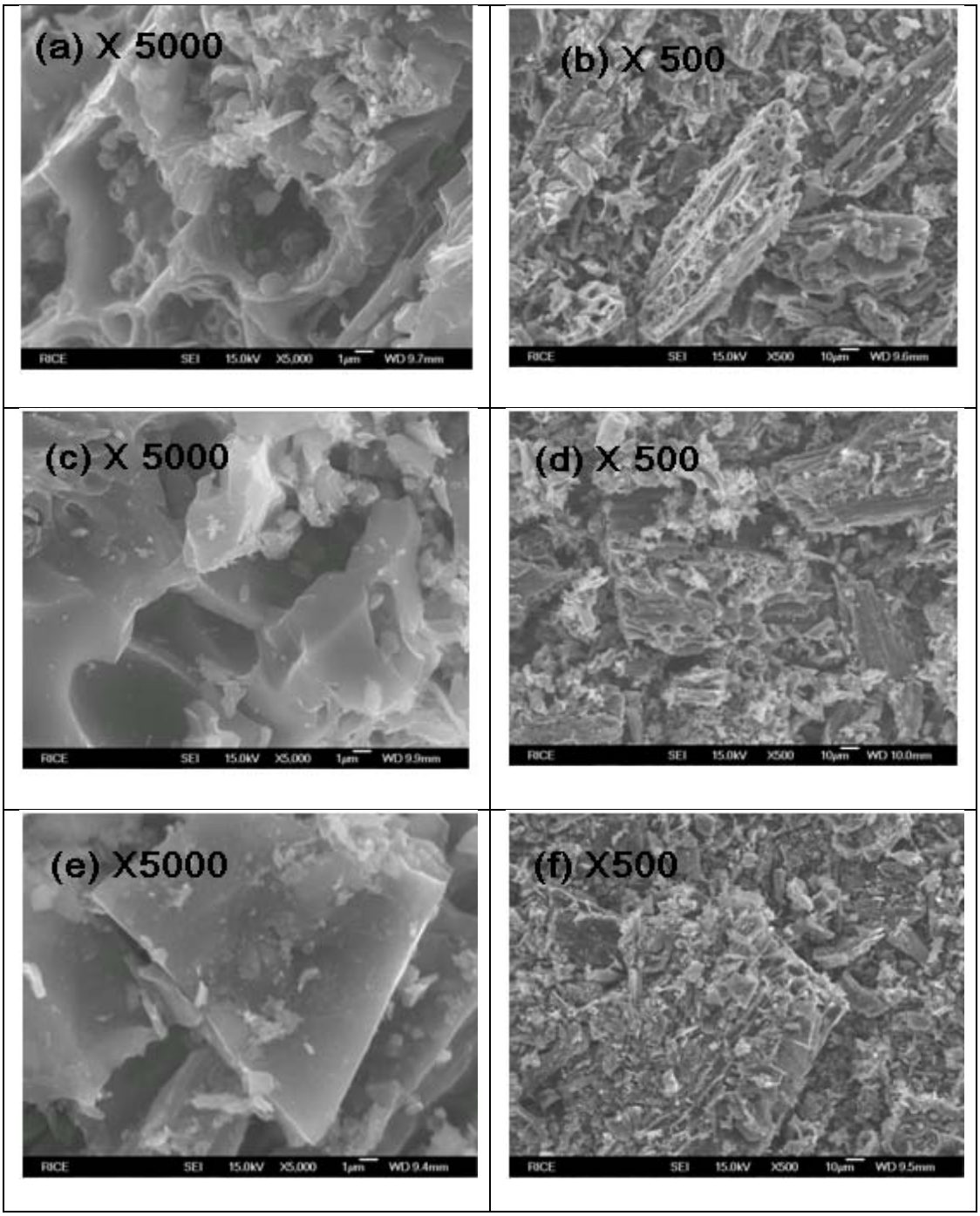
(a) X 5000
RICE SEI 15.0kV X5,000 1μm WD 9.7mm
(b) X 500
RICE SEI 15.0kV X500 10μm WD 9.6mm
(c) X 5000
RICE SEI 15.0kV X5,000 1μm WD 9.9mm
(d) X 500
RICE SEI 15.0kV X500 10μm WD 10.0mm
(e) X5000
RICE SEI 15.0kV X5,000 1μm WD 9.4mm
(f) X500
RICE SEI 15.0kV X500 10μm WD 9.5mm

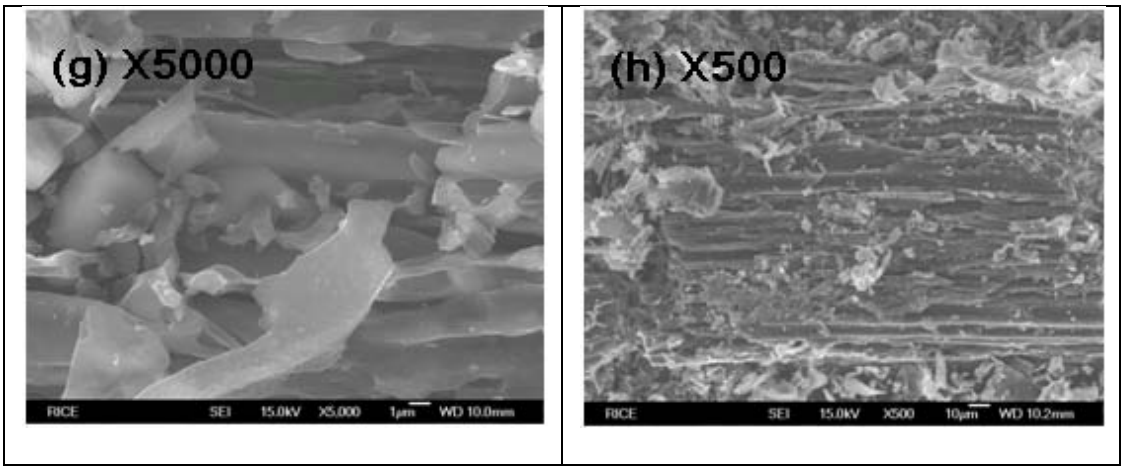

Figure 4.3:SEM micrographs of biochar samples prepared from apple wood and corn stover feedstocks. Panels (a-b): Apple wood biochar (HTT = 600ºC for 60 min; particle size = 1.5 mm; heating rate = 1 ºC/s). Panels (c-d): Apple wood biochar (HTT = 600ºC for 60 min; particle size = 0.25 mm; heating rate = 0.1 ºC/s); Panels (e-f): Corn stover biochar (HTT = 600ºC for 60 min; particle size = 0.25 mm, heating rate = 1 ºC/s); Panels (g-h): Corn stover biochar (HTT = 600ºC for 60 min; particle size =1.5 mm, heating rate = 0.1 ºC/s).

4.3 Probing the Multiscale Pore Structure of Biochars

To further probe the complicated multiscale pore structure of biochars, I used a simple combustion technique (thermogravimetric analysis) to measure the transient reactivity of biochars in air for temperatures ranging from 325 to 700 °C. Biochar reactivities were measured using equation (2.13) and their transient patterns were then interpreted with the help of well-established theoretical models [78, 109, 110, 151] that describe the temporal evolution of the porosity of carbonaceous materials with the extent of combustion.

At low temperatures, combustion proceeds in the regime of kinetic control and the entire surface area attributed to micropores is completely accessible to the reactant. As the temperature rises, the reaction regimes shifts to diffusion control and strong diffusional resistances start appearing first in the micropores and subsequently in the mesopores. Thus, larger and larger

fractions of the micropore and mesopore structure will become inaccessible to oxygen as the temperature is raised. At sufficiently high temperatures, combustion will take place only on the micropore and mesopores "mouths," where they open up into the large macropore cavities identified in SEM or optical microscopy images.

Simulation results were compared with experimental data from the combustion of different biochars to validate this technique. Chars produced from different biomass feedstocks (apple wood or corn stover) exhibited different reactivity patterns in the kinetic control regime. The simulations showed that the reactivity patterns of corn stover chars are consistent with a random distribution of the micropores. On the other hand, apple wood chars exhibited reactivity patterns that indicate the presence of a subpopulation of orderly distributed micropores. These micropores must be the slit pores formed between the graphitic-like layers of aromatic carbon clusters that are turbostratically arranged in nanometer-size crystallites, a structure that has been confirmed with NMR and XRD measurements. The same corn stover and apple wood chars exhibited similar reactivity patterns when combusted with oxygen in the regime of strong diffusional limitations, when oxygen cannot penetrate deeply into the micro- and mesopores and the reaction takes place at the pore "mouths" where they open up into the large macropore cavities. These patterns were consistent with a macropore structure that consists of many large cavities separated by walls of similar thickness.

These results demonstrate how TGA data and pore structure models can be used to gain significant insights into the pore structure of biochars. The new approach has the potential to overcome some of the major difficulties encountered in characterizing the complex pore structure of biochars and other carbonaceous solids.

From the solution of the diffusion-reaction problem in a porous solid [108], I know that at low temperatures combustion proceeds slowly enough so that oxygen can penetrate al the pores, even the smallest ones. Thus, the entire surface area attributed to micro- and mesopores is completely accessible to the reactant. At higher combustion temperatures, however, the oxygen diffusion rate is no longer sufficiently fast to keep up with the rapidly increasing reaction rate. At first, only the smaller micropores become inaccessible to oxygen at some intermediate temperature. As the reaction temperature continues to increase, however, strong diffusional limitations gradually develop in micropores and mesopores of any size. Thus, larger and larger fractions of the micropore and mesopore structure become inaccessible to oxygen as the temperature is raised [108, 151]. At sufficiently high temperatures, combustion takes place only on the micropore and mesopore "mouths," where they open up into the large macropore cavities identified in SEM micrographs [151].

Because of this interplay between diffusion and reaction, biochar reactivity at low temperatures (kinetic control regime) is controlled by the micropores and mesopores, which usually account for most of the pore surface area. At high temperatures (diffusion control regime), however, the macropore structure of biochars will become the primary control on their reactivity patterns [151].

The pore surface area S_g accessible to oxygen is a strong function of conversion. The relative rates of two competing processes determine the shape of the function $S_g(x)$. At low conversion, pore enlargement due to the chemical reaction leads to increases in the reacting pore surface area [109, 110]. As the solid char reacts and its conversion increases, however, walls between adjacent pores will burn and disappear, driving down the surface area of reacting pores.

This competition between pore enlargement and pore wall disappearance may drive $S_g(x)$ through a maximum as conversion increases.

The reaction rate $R(x)$ can be expressed as

$$R(x) = a \cdot S_g \cdot f(c,T) \tag{4.1}$$

where *a* is a surface activity factor $(0 < a < 1)$ to account for the fact that reaction occurs only on a fraction of $S_g(x)$, T and c are the reaction temperature and oxygen concentration respectively and $f(c,T)$ is a function that describes the kinetics of the reaction. We can isolate the surface area evolution pattern, however, if we normalize $R(x)$ by the reaction rate at some low conversion x_0 (equal to 0.01 here):

$$r(x) = \frac{R(x)}{R(x_0)} = \frac{S_g(x)}{S_g(x_0)} \tag{4.2}$$

Thus, the normalized reaction rate $r(x)$ can be used to describe the evolution of accessible pore surface with the extent of reaction [152].

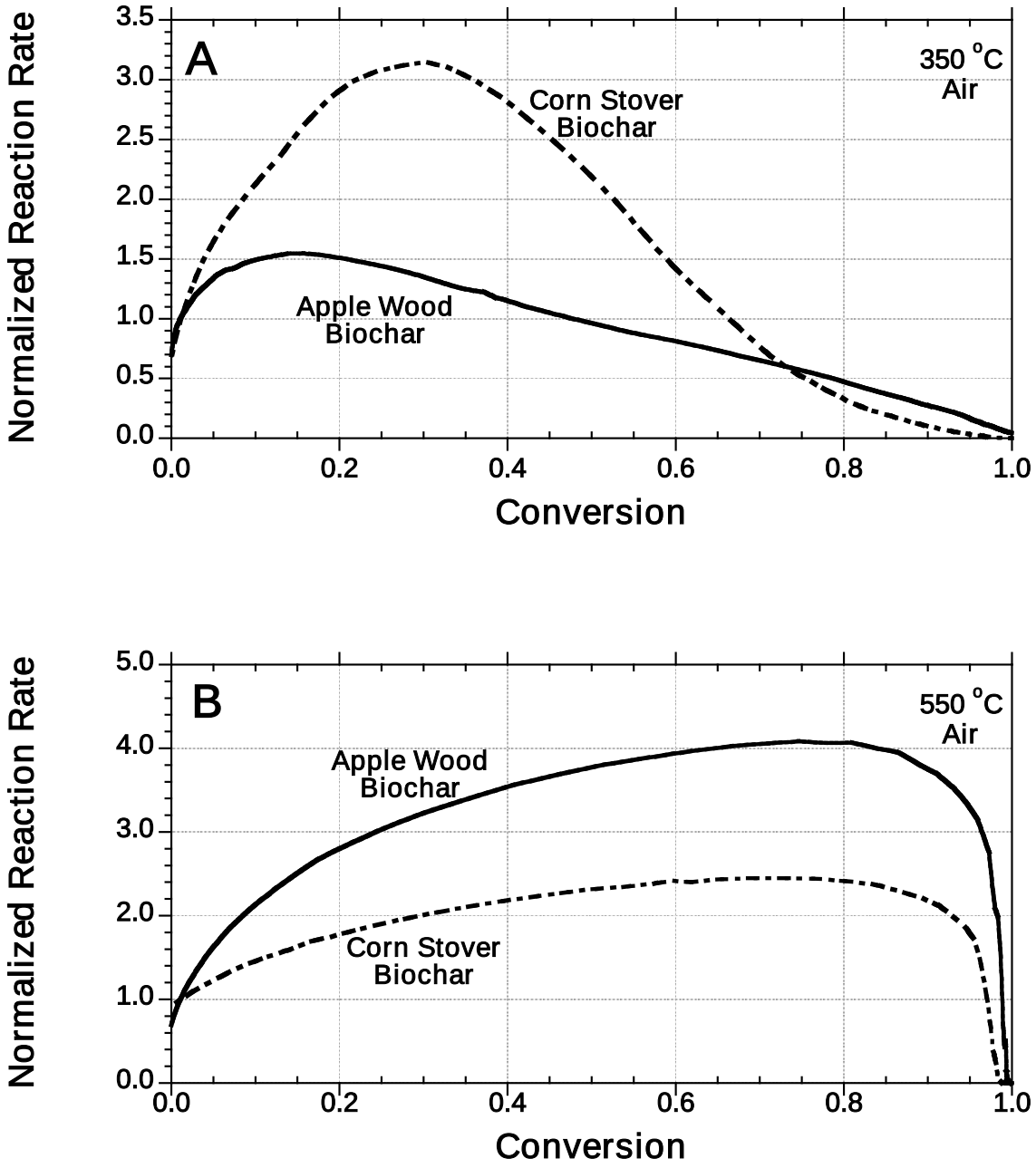

Figure 4.4: Normalized reactivity patterns for a corn stover and apple wood char reacted with air at (A) 350 ºC (kinetic control regime – micropores are fully utilized) and (B) 550 ºC (diffusion control regime – strong diffusional limitation in all but the largest pores). Both biochar samples were prepared using the following conditions: HTT = 600 ºC for 60 min; pyrolysis heating rate = 0.1 ºC/s; particle size = 1. 5 mm. All TGA measurements were done in triplicate and the average reactivity is reported here. The error bars indicate the standard deviation of the reaction rate values computed at several conversion levels.

Chars produced from apple wood or corn stover exhibit different reactivity patterns when combusted under low temperature (350°C) conditions, indicating significant differences in the structure of the pores accessible to oxygen at these conditions [78, 109, 110] (Figure 4.4A). The corn stover chars reach their maximum reactivity at 30% conversion to CO_2, an indication that the micropores and/or mesopores participating in the reaction are randomly distributed in the char (see references [78, 109, 110]). On the other hand, the apple wood chars exhibit maximum reactivity at about 15% conversion to CO_2, with an almost linear decrease in reactivity after that. We hypothesize that this pattern indicates either the onset of diffusional limitations or the presence of subpopulations of randomly and orderly distributed pores [78]. The orderly distributed pores, for example, may be the slit pores formed between the graphitic-like layers of aromatic carbon clusters that are turbostratically arranged in nanometer-size crystallites [59, 145]. Corn stover char reaches a higher maximum than that of apple wood char (Figure 4.4A). This is because the corn stover char has a much smaller micropore volume per unit mass of solid than the apple wood char (Tables 4.1-4.2). Thus, the pores of the corn stover char can enlarge considerably more than the corresponding pores of the apple wood char before the pore wall disappearance due to reaction will start driving down the surface area [78, 109, 110].

The corn stover and apple wood chars exhibit similar reactivity patterns when combusted with oxygen at 550 °C (Figure 4.4B). These patterns result from a macropore network that consists of many large cavities separated by walls of similar thickness (see Figure 4.3). At 550 °C, the diffusional limitations in the micro- and mesopores have become severe. Oxygen cannot penetrate deeply into them and the reaction takes place on the micropore “mouths,” where they open up into the large macropore cavities. As the solid walls are consumed by the reaction, the

macropores grow in size increasing the surface area available for reaction and, thus, the reactivity. This continues until the walls between adjacent cavities are completely consumed. Since the macropore cavities of our chars are separated by walls of similar thickness (see Figure 4.3), the reactivity drop due to pore wall disappearance occurs abruptly at a conversion close to 0.9 for both the apple wood and corn stover chars (Figure 4.4B). Since the reactivity pattern exhibits a smooth increase until the final dramatic drop, we can also conclude that there is no closed macroporosity consisting of internal cavities that are initially inaccessible to oxygen. If this were the case, the reactivity patterns would rise sharply when the reactant reached the "closed" macropores. Therefore, the large pores of our chars act as the main arteries through which oxygen diffuses into the particle interior to reach the meso- and micropores [153, 154].

Finally, Figure 4.4B shows that the reactivity pattern of the apple wood char reaches a higher maximum than the corn stover char. This is again consistent with the fact the corn stover chars have smaller bulk density than the apple wood chars [155], which implies that the walls separating the macropores of this char are thinner than the macropore walls of the apple wood char.

The approach used in the present work for the the determination of the apparent activation energy for combustion of biochar was based on the Arrhenius equation. We mainly focus on combustion of the biochar rather than on pyrolysis. The biochar sample reactivity $R(t)$ was computed by the formula (2.11) as function of weight conversion ratio x in time t, where x is the conversion of the combustion reaction defined by (2.12).

The reaction rate constant k can be described by the Arrhenius expression:

$$k = A\exp(-\frac{E}{RT}) \tag{4.3}$$

Where A is the pre-exponential factor (min^{-1})

E is the activation energy of the reaction (J/mol)

R is the gas constant (8.314 J/(mol·K))

T is the combustion temperature (K)

Thus, we can write equation (2.11) as

$$\frac{dx}{dt} = A\exp(-\frac{E}{RT})(y_A)^n \tag{4.4}$$

To determine the reaction order n, equation (4.4) is rearranged by taking the $\log_{(10)}$ of both sizes. When plotting $\log_{10}(\frac{dx}{dt})$ vs. $\log_{10}(y_A)$, the slope should give us the reaction order n. According to equation (4.4), a plot of $\log_{10}[\frac{\frac{dx}{dt}}{(y_A)^n}]$ versus $\frac{1}{T}$ corresponds to a straight line with a slope of $(-\frac{E}{R})$ for a certain value of n and $\log_{10}(A)$ is the intercept. Due to the dominat C and O components within the biochar, a single kinetic model can explain the general mechanism of combustion in all types of biochar.

The apparent activation energy and the pre-exponential factor for 1.5mm corn stover char (pyrolysed under 0.1°C /sec 600°C 1 hour) combustion process are shown in Table 4.3. I found that the activation energy usually does not work over a wide temperature range (0-973K), which is important in trying to extrapolate the data. Above 400°C, the reaction is in diffusion control regime (Figure 4.5). The reaction rate is taken as the conversion is 20%. The σat 350°C, 400°C and 550°C combustion experiment is 0.071952139, 0.034802276 and 0.036974544 (Fig. 4.6).

Table 4.3:

Apparent activation energy and pre-exponential factor for bichar combustion process

Temperature regime (K)	Apparent activation energy, E (kJ/mol)	pre-exponential factor, $\log_{10}(A)$ (min^{-1})
325-400	35.7	6.3
400-700	4.316	0.54

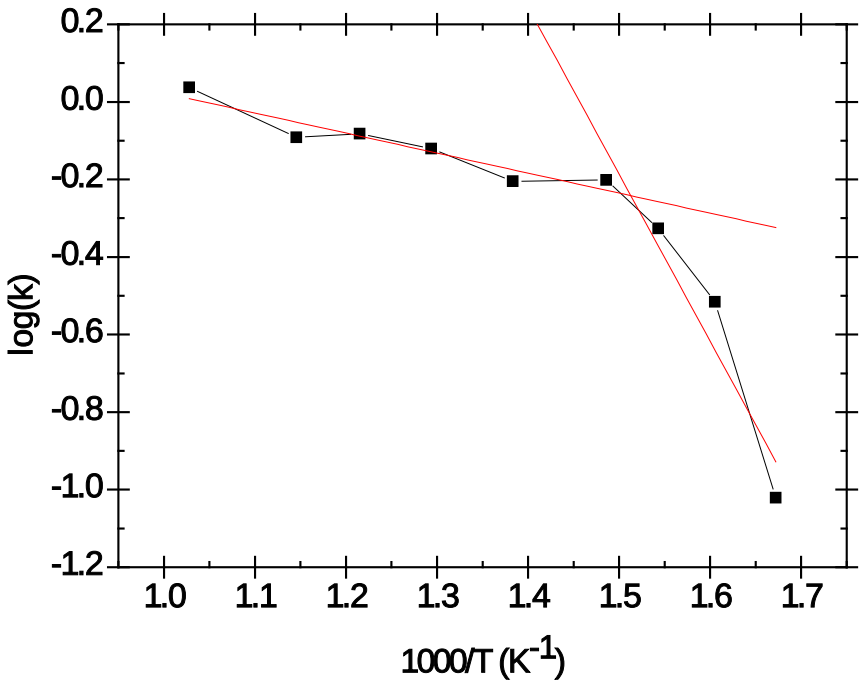

Figure 4.5 Arrhenius plot of Log10(K) vs. (1000/Temperature) of 1.5mm corn stover (Heating rate: 0.1 deg/sec) to determine the activation energy and pre-exponential factor

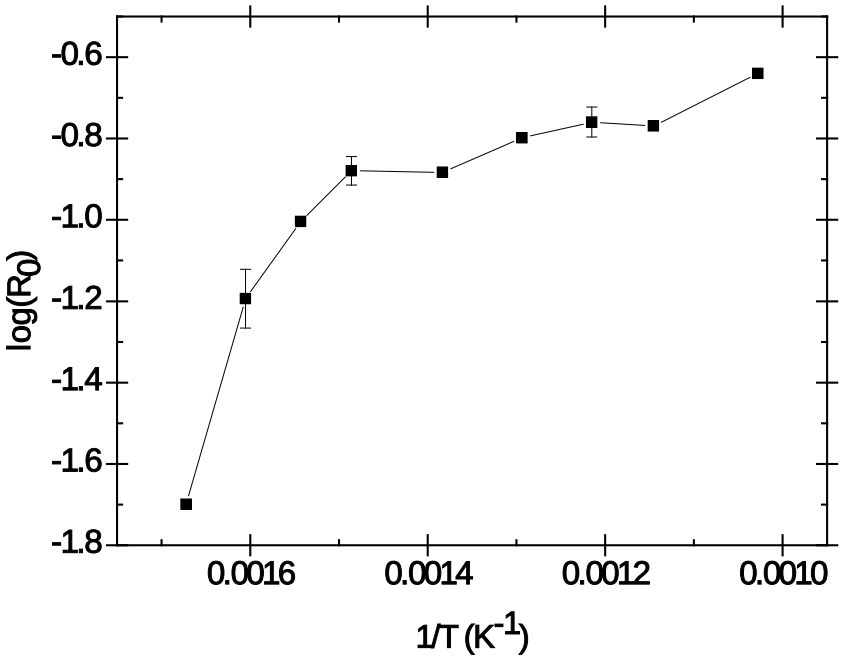

Figure 4.6 Log scale reaction rate plot

CHAPTER 5

Multi-porosity models for simulating the water and nutrient flow through biochar/soil mixture porous media

5.1 Models for the nutrient ions mass transfer through biochar/soil mixture porous media

A primary objective of my research was to develop a systematic process that will allow us to engineer biochars with optimal nutrient adsorption properties. For this reason, I describe here a theoretical model that can help us quantify the effect of biochar properties on the dynamics of the adsorption/desorption process and the total adsorption capacity of soil/biochar mixtures (Figure 5.1). The properties I will consider include the biochar/soil weight ratio, biochar particle size and porosity, and the parameters of the isotherm that describes adsorption of the nutrient on biochar. I will start by considering the case of nutrient (fertilizer) flow in a fully saturated porous medium consisting of a mixture of biochar and soil particles. As the solution flows through a fixed bed of biochar/soil, the solute will be transported from the bulk to the adsorbent particles and diffuse through the liquid-filled pores of the particles before being adsorbed on the pore surface. The overall process involves external mass transport, internal pore diffusion and adsorption steps. Using this model, I show that fertilizer adsorption is strongly influenced by the mass fraction of biochar in the soil, biochar particle size, porosity, and adsorption affinity.

In the second part of this chapter, I begin the development of a dynamic model that will allow us to relax the assumption that the solute flows through a fully saturated soil/biochar mixture. To do this, I must estimate the length of time it takes to saturate layer of soil/biochar mixture with water and the time it takes to drain the wayer from it. I will show that the time

required for saturation or drainage is much shorter than the timescale over which significant solute adsorption on the biochar will occur. This result allows us to treat the saturation or drainage as an essentially instantaneous process and, thus, consider the nutrient adsoption/elution processes independently from saturation and drainage.

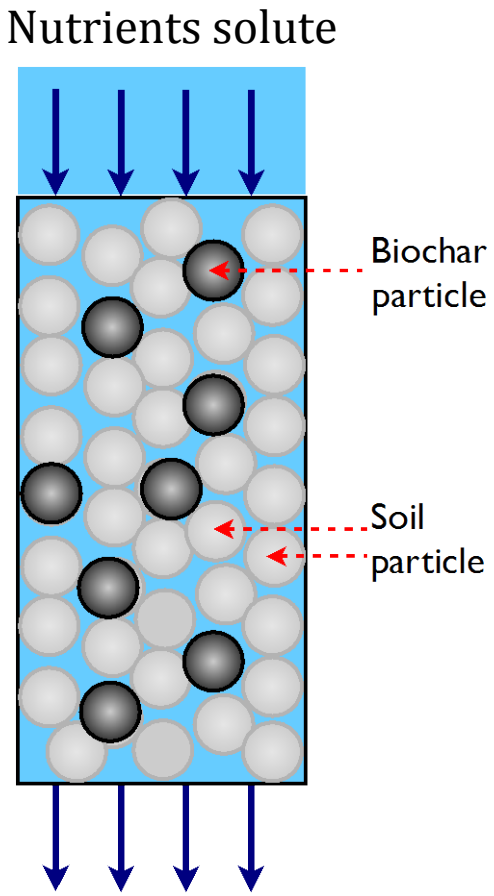

Figure 5.1 Schemetic picture of the biochar/soil porous media

5.1.1 Equilibrium isotherm and dynamic adsorption model

My model uses a Langmuir isotherm to describe the adsorption and desorption of the solute (nutrient) on biochar and soil. The affinity b and biochar maximum adsorption capacity q_m are the two constants determining the adsorption equilibrium. Both q_m and b are mathematical representations of the physical and chemical state of the surface of biochar. I attempted to

measure both these parameters using static adsorption experiments. However, our fresh biochars did not have a sufficient adsorption capacity to distinguish them from soils. This is consistent with studies on fresh vs aged biochars. For example, Cheng et al. measured the effective cation exchange capacity (ECEC) of biochar at field sites along a climosequence and found that fresh biochar had an ECEC of 9.5±3.1 mmol/kg C, while aged biochar had an ECEC of 1125±424 mmol/kg C[144]. Developing a process that will "age" the surface of fresh biochar is a future goal of our group. For this study, I relied on previous studies of ammonia sorption onto biochar[156] and soil [157] to chose the following values of the parameters: biochar affinity b is equal 2.25 m^3/mol, maximum biochar adsorption capacity q_m is 0.05 mol/kg, soil b is 0.4 m^3/mol, q_m at 0.01 mol/kg based on previous studies of ammonia sorption onto biochar[156] and soil [157] Figure 5.2 shows the isotherms obtained for these parameter values.

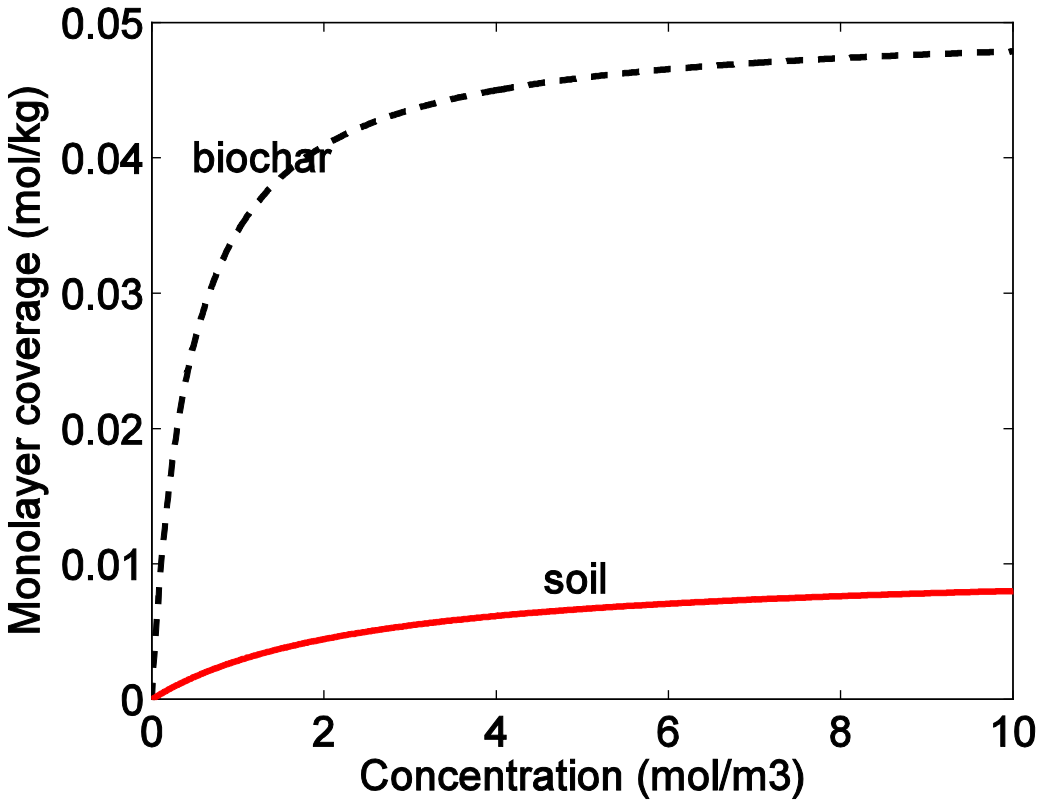

Figure 5.2 biochar [156] and soil [157] Langmuir isotherm

Langmuir isotherm model

I use the Langmuir isotherm to describe the adsorption equilibrium of NH_4^+ ions onto biochar/soil. If q_e (mol/kg) is the amount of solute adsorbed at equilibrium, the Langmuir isotherm[158] is expressed as:

$$q_e = \frac{q_m b C_e}{1 + b C_e} \tag{5.1}$$

where b (L/mol) is the adsorption affinity, C_e (mol/L) is the equilibrium bulk concentration and q_m (mol/kg) is the maximum adsorption capacity.

The linear form of Langmuir equation must be used given to identify q_m and b from experimental data:

$$\frac{C_e}{q_e} = \frac{1}{q_m b} + \frac{C_e}{q_m} \tag{5.2}$$

Thus, $1/q_m$ and $1/q_m b$ are the slope and intercept of the plot of C_e/q_e versus C_e.

The assumptions of the Langmuir isotherm (the adsorbent has a uniform surface; absence of interactions between the adsorbate molecules; a homogeneous single layer surface adsorption process) are applicable to the adsorption process of NH_4^+ ions onto biochar/soil [159]. Furthermore, the adsorption parameters are independent of the adsorbent particle size. While the adsorption rate decreases with increasing adsorbent particle size (as one expects when intraparticle diffusion becomes significant), the adsorption capacity is independent of the adsorbent particle size[160].

I considered and rejected four other isotherm models: the Henry, Freundlich, Sips and RP isotherms models. The Henry isotherm is the simplified version of Langmuir isotherm and assumes the slope of the adsoption isotherm is linear when the equilibrium bulk concentration is low. The Freundlich isotherm has similar form as the Henry isotherm, which is easy to use for

the mass transport models. However, both of them have the disadvantage of predicting an infinite maximum adsorption capacity when the equilibrium bulk concentration is large, which is not realistic. Both Sips and RP isotherms have more parameters than Langmuir isotherm. They may be used in situations when Lagmuir isotherm fail to describe the experimental isotherm data[159].

Dynamic adsorption model

Generally, the model of the uptake of NH_4^+ ion adsorbates on adsorbents is governed by the following distinct diffusion and reaction steps [161-164]:

(1) Diffusion of ions from the bulk fluid to the adsorbent particle surfaces across the thin liquid film that forms around the adsorbent particles.

(2) Diffusion of ions through a network of intraparticle pores to reach surface adsorption sites.

(3) Adsorption of ions at the surface adsorption sites.

Normally, the adsorption reaction rate at these sites is fast compared to intraparticle diffusion rates. Thus, the various diffusion steps are considered to be rate limiting.

Three models (pore/surface/parallel) diffusion models are normally set up to consider similar adsorption problems [161-164]. For the pore diffusion model, mass transport is assumed to only take place in the pore fluid. The pore diffusion model has been used for low-affinity solutes like metal ions in macroporous chars and zeolite adsorbents. The adsorbates can overcome the local adsorption with the surface and transport along the surface, which is defined as surface diffusion. Surface diffusion is negligible if it takes place in macropores with infinite concentration of free adsorbates, since pore diffusion is dominant at that case. However, for high-affinity adsorbates

like proteins adsorption on gel-type resins[165-170], although surface diffusivity is usually three or four orders of magnitude smaller than pore diffusivity, surface concentration can be orders of magnitude higher than pore concentration, which leads to a larger surface diffusion flux than the correspondent pore diffusion flux. The parallel (macro-micro/bidisperse) diffusion model considers the adsorbates diffusions both in the pore fluid and along the pore surface[160]. For ions adsorption on solids with a bimodal pore system like biochars, I use the pore diffusion model. However, the adsorption process of biochar soil amendment is complicated because multi-adsorbents (biochar/soil) form a heterogeneous system.

Here is a full list of my assumptions:

(1) The column is homogeneous with uniform porosity.

(2) Inside the biochar/soil particle, the NH_4^+ ion concentration in the pore liquid is in instantaneous equilibrium with that on the solid surface through Langmuir isotherm correlation.

(3) The biochar/soil particles are well packed and do not move in the column.

(4) Both fluid and solid compressibility are negligible.

(5) Fluid flows at a constant rate and is uniform throughout the bed.

(6) The flow is isothermal.

(7) Surface diffusion is negligible.

(8) Dispersion occurs only in the flow axial direction.

(9) The biochar/soil mixture particles are spherical.

(10) There is a uniform pH=7 of the solution throughout the column due to the high soil buffer capacity. NH_4^+ ions are available to plants in solution when the soil pH is around 7.

(11) The diffusion resistance in the micropores is negligible due to negligible NH_4^+ ion concentration in the micropores compared with that in macropores[158].

The derivation of the mass balance equations of my system is as following:

The overall mass transfer in the adsorption column for the process is the following:

Rate of solute enter by flow - Solute consumption = rate of solute exit by flow + rate of accumulation of solute in the fluid phase:

The resulting partial differential equation is:

$$\varepsilon_b JS\big|_x - \frac{\partial \overline{q_c}}{\partial t}\rho_{ac}\Delta xS(1-\varepsilon_b)\frac{V_{char}}{V_{char}+V_{soil}} - \frac{\partial \overline{q_s}}{\partial t}\rho_{as}\Delta xS(1-\varepsilon_b)\frac{V_{soil}}{V_{char}+V_{soil}} = \varepsilon_b JS\big|_{x+\Delta x} + \frac{\partial C}{\partial t}\varepsilon_b \Delta xS \quad (5.3)$$

The mass balance equations of bulk fluid include the accumulation term, the axial dispersion term, the convection term (I use Darcy's law to compute the superficial velocity) and the adsorption term.

According to Fick's Law:

$$J = -D_L\frac{dC}{dx} + Cu_o \quad (5.4)$$

$$u_o = \frac{u_s}{\varepsilon_b} \quad (5.5)$$

$$u_s = \frac{V_s}{\pi R^2} \quad (5.6)$$

$$V_{char} = \frac{m_{char}}{\rho_{ac}} \quad (5.7)$$

$$V_{soil} = \frac{m_{soil}}{\rho_{as}} \quad (5.8)$$

In the previous equations, k (m^2) is the permeability of the packed column, μ (pa*s) is the water viscosity, u_o (m/s) is the interstitial velocity, u_s (m/s) is the superficial velocity, x is the coordinate along the length of the column, t (s) is the time, ρ_{ac} (kg/m^3) is the apparent density of biochar particles, ρ_{as} (kg/m^3) is the apparent density of soil particles, $\overline{q_c}$ (mol/kg) is the average adsorption capacity of biochar particles, $\overline{q_s}$ (mol/kg) is the average adsorption capacity of soil particles, ε_b is the porosity of bed, D_L (m^2/s) is the axial dispersion coefficient, and C (mol/L) is the concentration of NH_4^+ ions in the bulk liquid. The soil and biochar are evenly mixed, and therefore $\frac{V_{char}}{V_{char}+V_{soil}}$ is the same for any volume element. Since the concentration ranges of NH_4^+ solutions are dilute, the density and the viscosity of the adsorbate solution are equal to those of water at room temperature (25°C).

By rearranging equation (5.3) we obtain:

$$-D_L\frac{\partial^2 C}{\partial x^2}+u_o\frac{\partial C}{\partial x}+\frac{\partial C}{\partial t}=-\frac{\partial \overline{q_c}}{\partial t}\rho_{ac}\frac{(1-\varepsilon_b)}{\varepsilon_b}\frac{V_{char}}{V_{char}+V_{soil}}-\frac{\partial \overline{q_s}}{\partial t}\rho_{as}\frac{(1-\varepsilon_b)}{\varepsilon_b}\frac{V_{soil}}{V_{char}+V_{soil}} \tag{5.9}$$

The axial dispersion coefficient D_L was calculated by the correlation[171]:

$$D_L=0.44D_m+0.83u_0d_p \tag{5.10}$$

The average particle diameter is d_p (m). The molecular diffusivity D_m is around 1.957×10^{-9} m^2/s for NH_4^+ ions in aqueous solution at 25°C [172]. This value is comparable with the experimental measured diffusivities of ammonium salts [173, 174].

Boundary Conditions:

$$x=L:\quad \left.\frac{\partial C}{\partial x}\right|_{x=L}=0 \tag{5.11}$$

$$x = 0: \quad D_L \frac{\partial C}{\partial x}\Big|_{x=0} = u_o (C\Big|_{x=0} - C_{input}) \tag{5.12}$$

This is a "closed-closed" boundary instead of "open-open" boundary [175].

Initial Conditions:

$$\text{t=0:} \quad C(t=0,x) = C_{pc}(t=0,x,r) = C_{ps}(t=0,x,r) = 0 \tag{5.13}$$

The concentration of NH_4^+ ions of feed is C_{input} (mol/L) and the length of the column is L (m).

For the mass transfer through the stagnant liquid film around a spherical biochar/soil particle, the adsorption rate is equal to the diffusion rate across the film:

$$\rho_{ac} \frac{\partial \overline{q_c}}{\partial t} = \frac{3k_{fc}}{r_{pc}} (C - C_{pc}\Big|_{r=r_{pc}}) \tag{5.14}$$

$$\rho_{as} \frac{\partial \overline{q_s}}{\partial t} = \frac{3k_{fs}}{r_{ps}} (C - C_{ps}\Big|_{r=r_{ps}}) \tag{5.15}$$

The mass-transfer coefficient of biochar particle is k_{fc} (m/s), the average biochar particle radius is r_{pc} (m), the concentration of NH_4^+ ions of the pore liquid in biochar particles is C_{pc} (M). The mass-transfer coefficient of soil particle is k_{fs} (m/s), the average soil particle radius is r_{ps} (m), the concentration of NH_4^+ ions of the pores liquid in soil particles is C_{ps} (M), q_c (mol/kg) is the adsorption capacity of biochar particles, q_s (mol/kg) is the adsorption capacity of soil particles.

By assuming that a pore liquid is in equilibrium with the adsorbed phase, mass transfer in macropores of biochar/soil particle is as follows:

Solute Enter- Solute consumption= Solute exit+ Solute accumulation

The resulting partial differential equation is:

$$N_c 4\pi r^2\Big|_r - \frac{\partial q_c}{\partial t} \rho_{ac} 4\pi r^2 \Delta r (1-\varepsilon_{pc}) = N_c 4\pi r^2\Big|_{r+\Delta r} + \frac{\partial C_{pc}}{\partial t} 4\pi r^2 \Delta r \varepsilon_{pc} \tag{5.16}$$

$$-\frac{1}{r^2}\frac{d(N_c r^2)}{dr} = \varepsilon_{pc}\frac{\partial C_{pc}}{\partial t} + \frac{\partial q_c}{\partial t}\rho_{ac}(1-\varepsilon_{pc}) \tag{5.17}$$

Inside the biochar particle, the NH_4^+ ion concentration in the pore liquid (C_{pc}) is in instantaneous equilibrium with that on the solid surface (q_c) through the Langmuir isotherm correlation.

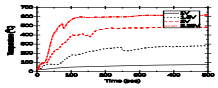

(5.18)

Similar to the mass balance for the biochar particle equation (5.16), we can write the mass balance for the soil particle:

$$N_s 4\pi r^2\big|_r - \frac{\partial q_s}{\partial t}\rho_{as}4\pi r^2\Delta r(1-\varepsilon_{ps}) = N_s 4\pi r^2\big|_{r+\Delta r} + \frac{\partial C_{ps}}{\partial t}4\pi r^2\Delta r\varepsilon_{ps} \tag{5.19}$$

$$-\frac{1}{r^2}\frac{d(N_s r^2)}{dr} = \varepsilon_{ps}\frac{\partial C_{ps}}{\partial t} + \frac{\partial q_s}{\partial t}\rho_{as}(1-\varepsilon_{ps}) \tag{5.20}$$

$$N_s = -\varepsilon_{ps}^2 D_{ps}\frac{\partial C_{ps}}{\partial r} \tag{5.21}$$

r is radial coordinate of the particle, ε_{pc} is the porosity of biochar particles, ε_{ps} is the porosity of soil particles, D_{pc} (m^2/s) is the biochar pore diffusivity and D_{ps} (m^2/s) is the soil pore diffusivity. Therefore, the soil effective diffusivity D_{pse} (m^2/s) and the biochar effective diffusivity D_{pce} (m^2/s) are defined from the random-pore model as following [176]:

$$D_{pce} = \varepsilon_{pc}^2 D_{pc}, D_{pse} = \varepsilon_{ps}^2 D_{ps} \tag{5.22}$$

This random-pore model is applied to a monodisperse macropore system, since the contribution to total diffusion from macropores is much higher than that from nanopores.

By rearranging equation (5.17), I obtain:

$$\frac{\varepsilon_{pc}^2 D_{pc}}{r^2}\frac{\partial}{\partial r}(r^2\frac{\partial C_{pc}}{\partial r}) = \varepsilon_{pc}\frac{\partial C_{pc}}{\partial t} + \frac{\partial q_c}{\partial t}\rho_{ac}(1-\varepsilon_{pc}) \tag{5.23}$$

With the following boundary conditions:

$$r = 0 : \frac{\partial C_{pc}}{\partial r}\Big|_{r=0} = 0 \tag{5.24}$$

$$r = r_{pc} : \varepsilon_{pc}^2 D_{pc}\frac{\partial C_{pc}}{\partial r}\Big|_{r=r_{pc}} = k_{fc}(C - C_{pc}\Big|_{r=r_{pc}}) \tag{5.25}$$

And initial conditions:

$$t = 0 : \quad C_{pc}(t = 0, x, r) = 0 \tag{5.26}$$

Rearrange equation (5.20), we have:

$$\frac{\varepsilon_{ps}^2 D_{ps}}{r^2}\frac{\partial}{\partial r}(r^2\frac{\partial C_{ps}}{\partial r}) = \varepsilon_{ps}\frac{\partial C_{ps}}{\partial t} + \frac{\partial q_s}{\partial t}\rho_{as}(1-\varepsilon_{ps}) \tag{5.27}$$

Boundary Conditions:

$$r = 0 : \frac{\partial C_{ps}}{\partial r}\Big|_{r=0} = 0 \tag{5.28}$$

$$r = r_{ps} : \varepsilon_{ps}^2 D_{ps}\frac{\partial C_{ps}}{\partial r}\Big|_{r=r_{ps}} = k_{fs}(C - C_{ps}\Big|_{r=r_{ps}}) \tag{5.29}$$

Initial Conditions:

$$t = 0 : \quad C_{ps}(t = 0, x, r) = 0 \tag{5.30}$$

The dimensionless form of (5.9) can be gotten by:

$$z = \frac{x}{L} \quad \tau = \frac{tu_o}{L} \tag{5.31}$$

Biochar Biot number:

$$Bi_c = \frac{k_{fc} r_{pc}}{D_{pce}} \tag{5.32}$$

Soil Biot number:

$$Bi_s = \frac{k_{fs} r_{ps}}{D_{pse}} \tag{5.33}$$

Peclet number in the bulk phase:

$$Pe_b = \frac{L u_o}{D_L} \tag{5.34}$$

Peclet number of the biochar particle:

$$Pe_{pc} = \frac{r_{pc} u_o}{D_{pce}} \tag{5.35}$$

Peclet number of the soil particle:

$$Pe_{ps} = \frac{r_{ps} u_o}{D_{pse}} \tag{5.36}$$

$$\frac{\partial C}{\partial \tau} - \frac{1}{Pe_b}\frac{\partial^2 C}{\partial z^2} + \frac{\partial C}{\partial z} + \frac{(1-\varepsilon_b)}{\varepsilon_b}\frac{3L}{r_{pc}}\frac{Bi_c}{Pe_{pc}}(C - C_{pc}\big|_{r=r_{pc}})\frac{V_{char}}{V_{char}+V_{soil}} + \frac{(1-\varepsilon_b)}{\varepsilon_b}\frac{3L}{r_{ps}}\frac{Bi_s}{Pe_{ps}}(C - C_{ps}\big|_{r=r_{ps}})\frac{V_{soil}}{V_{char}+V_{soil}} = 0 \tag{5.37}$$

Boundary Conditions:

$$z = 1: \quad \frac{\partial C}{\partial z}\Big|_{z=1} = 0 \tag{5.38}$$

$$z = 0: \quad \frac{\partial C}{\partial z}\Big|_{z=0} = Pe_b(C\big|_{z=0} - C_{input}) \tag{5.39}$$

Initial Conditions:

$$\tau = 0: \quad C(\tau, z) = 0, q_c(\tau, z, \rho) = 0, q_s(\tau, z, \rho) = 0 \tag{5.40}$$

Since $\rho = \frac{r}{r_{pc}}$, the dimensionless form of (5.23) can be gotten by:

$$\varepsilon_{pc}\frac{\partial C_{pc}}{\partial \tau}+\frac{\partial q_c}{\partial \tau}\rho_{ac}(1-\varepsilon_{pc})-\frac{1}{Pe_{pc}}\frac{L}{r_{pc}}\frac{1}{\rho^2}\frac{\partial}{\partial \rho}(\rho^2\frac{\partial C_{pc}}{\partial \rho})=0 \tag{5.41}$$

Boundary Conditions:

$$\rho=0:\ \frac{\partial C_{pc}}{\partial \rho}=0,\ \frac{\partial q_c}{\partial \rho}=0 \tag{5.42}$$

$$\rho=1:\ \frac{\partial C_{pc}}{\partial \rho}\Big|_{\rho=1}=Bi_c(C-C_{pc}\Big|_{\rho=1}) \tag{5.43}$$

Initial Conditions:

$$\tau=0:\quad C_{pc}(\tau=0,z,\rho)=0 \tag{5.44}$$

Since $\rho=\frac{r}{r_{ps}}$, the dimensionless form of (5.27) can be gotten by:

$$\varepsilon_{ps}\frac{\partial C_{ps}}{\partial \tau}+\frac{\partial q_s}{\partial \tau}\rho_{as}(1-\varepsilon_{ps})-\frac{1}{Pe_{ps}}\frac{L}{r_{ps}}\frac{1}{\rho^2}\frac{\partial}{\partial \rho}(\rho^2\frac{\partial C_{ps}}{\partial \rho})=0 \tag{5.45}$$

Boundary Conditions:

$$\rho=0:\ \frac{\partial C_{ps}}{\partial \rho}\Big|_{\rho=0}=0,\ \frac{\partial q_s}{\partial \rho}\Big|_{\rho=0}=0 \tag{5.46}$$

$$\rho=1:\ \frac{\partial C_{ps}}{\partial \rho}\Big|_{\rho=1}=Bi_s(C-C_{ps}\Big|_{\rho=1}) \tag{5.47}$$

Initial Conditions:

$$\tau=0:\quad C_{ps}(\tau=0,z,\rho)=0 \tag{5.48}$$

There are three important sets model parameters in the above equations: the external mass transfer coefficients (k_{fc} and k_{fs}), effective diffusivities (D_{pce} and D_{pse}) and the axial dispersion coefficient D_L. The values of D_{pce} and D_{pse} are determined by the pore structure of adsorbent particles. The external mass transfer coefficients k_{fc} and k_{fs} primarily depend on the flow

conditions around the biochar/soil particles and are virtually independent of feed concentrations in solution[158]. The axial dispersion coefficient D_L in a two-adsorbent system is determined by the larger particle adsorbent.

Since k_{fc} and k_{fs} are primarily dependent on the flow conditions around the biochar/soil particle, they can be calculated if we know the Sherwood number ($Sh = \frac{k_f d_p}{D_m}$). The commonly used empirical correlation is:

$$Sh = 2 + 0.6\,\mathrm{Re}^{0.5} Sc^{\frac{1}{3}} \tag{5.49}$$

where the Reynolds and Schmidt numbers are defined as $\mathrm{Re} = \frac{\rho u_s d_p}{\mu}$ and $Sc = \frac{\mu}{\rho D_m}$.

However, the empirical correlations may not be suitable for the biochar/soil particle–liquid system possibly because these correlations were developed with specific solids that are different in chemical and physical characteristics from the biochar/soil particles[158]. Therefore, experimental determination of these parameters is essential.

5.1.2 Numerical solution method (orthogonal collocation on finite elements)

I solved the set of partial differential equations (PDEs) (Equations 5.37-5.48) numerically using orthogonal collection on finite elements (OCFE), which divides the solution domain into a specified number of finite elements. Then orthogonal collection is applied within each element. The advantage of OCFE is that it increases the total number of grid points without increasing the trial function order (Figure 5.2). Thus, the OCFE technique combines the orthogonal collocation method, which is convenient for solving symetrial geometry problems, with the high accuracy of the finite elements method [177]. In orthogonal collocation on finite elements (OCFE), the

derivative is expressed in terms of the solution at all the collocation points in one finite element, whereas in the finite difference method the derivatives are expressed only in terms of the solution at adjacent grid points. When I choose the interior point as 1, the orthogonal collocation method is exactly the same as the central difference finite difference method. By using the same number of interior grid points, the accuracy of finite-difference method is lower compared with the orthogonal collocation method [178]. When implementing OCFE for the previous system of PDEs (Equations 5.37-5.48), the system of equation reduces to a system of algebraic differential equations (ADE). I employ DASSL, a backward differentiation scheme, to advance the solution in the time domain to solve such systems of ADEs numerically[179, 180].

Previous literature studies have shown how this numerical procedure can be used to solve the single adsorbent system [181-183]. To solve the two adsorbent problem, the grid point system and the grid point numbering need to be modified.

Both the z and the r direction need to be normalized to 1. In the z direction, the interval is divided into N_{el} equally spaced finite elements with N_{el} internal grid points Z_k. The length of each finite element is:

$$L_{el} = \frac{1}{N_{el}} \tag{5.50}$$

Inside each element such as the kth element, the distance variable needs to be normalized as below:

$$s_k = \frac{z - Z_{k-1}}{L_{el}} \tag{5.51}$$

In the r direction, it considers the concentration profile inside each particle of two adsorbents, the concentration gradient is not sharp. Therefore, one element is used for simplicity. Inside the particle, NR interior collocation points are taken in the symmetrical radial direction; in

the bulk fluid phase, NP interior collocation points are taken in the axial direction. The total number of grid points is (2*NR+3)*((NP+1)*N_{el}+1). The solutions of the PDE systems are the concentrations at all these grid points. The collocation points and discretization matrices in the z and r directions are calculated numerically using the subroutine PLANAR and COLL respectively as followings[178].

$$\frac{\partial C}{\partial z} = \frac{1}{L_{el}}[\sum_{l=1}^{l=NP+2} AZ_{i,l} C_l^{\,k}] \tag{5.52}$$

$$\frac{\partial^2 C}{\partial z^2} = \frac{1}{L_{el}^2}[\sum_{l=1}^{l=NP+2} BZ_{i,l} C_l^{\,k}] \tag{5.53}$$

$$\frac{\partial C_{ps}}{\partial \rho} = \sum_{l=1}^{l=NR+1} AR_{j,l} c_{l,soil}^{i,k} \tag{5.54}$$

$$\frac{1}{\rho^2}\frac{\partial}{\partial \rho}(\rho^2 \frac{\partial C_{ps}}{\partial \rho}) = \sum_{l=1}^{l=NR+1} BR_{j,l} c_{l,soil}^{i,k} \tag{5.55}$$

At each interior collocation point in the bulk phase in z direction,

$$\frac{dC_i^k}{d\tau} - \frac{1}{Pe_b}\frac{1}{L_{el}^2}[\sum_{l=1}^{l=NP+2} BZ_{i,l} C_l^{\,k}] + \frac{1}{L_{el}}[\sum_{l=1}^{l=NP+2} AZ_{i,l} C_l^{\,k}]$$
$$+ \frac{(1-\varepsilon_b)}{\varepsilon_b}\frac{3L}{r_{pc}}\frac{Bi_c}{Pe_{pc}}(C_i^k - c_{2NR+2,char}^{i,k})\frac{V_{char}}{V_{char}+V_{soil}} + \frac{(1-\varepsilon_b)}{\varepsilon_b}\frac{3L}{r_{ps}}\frac{Bi_s}{Pe_{ps}}(C_i^k - c_{NR+1,soil}^{i,k})\frac{V_{soil}}{V_{char}+V_{soil}} = 0 \tag{5.56}$$

k is the number of each element. i is the number of each interior collocation point in z direction.

Boundary Conditions:

column exit: $z = 1$:

$$\frac{1}{L_{el}}[\sum_{l=1}^{l=NP+2} AZ_{NP+2,l} C_l^{\,N_{el}}] = 0 \tag{5.57}$$

column inlet: $z = 0$:

$$\frac{1}{L_{el}}[\sum_{l=1}^{l=NP+2} AZ_{1,l}C_l^1] = Pe_b(C_l^1 - C_{input}) \tag{5.58}$$

Initial Conditions:

$$\tau = 0: \quad C_i^k(\tau, z) = C_{input} \tag{5.59}$$

Between two neighboring elements, the equality of the flux is assumed.

$$\frac{1}{L_{el}}[\sum_{l=1}^{l=NP+2} AZ_{NP+2,l}C_l^k] = \frac{1}{L_{el}}[\sum_{l=1}^{l=NP+2} AZ_{1,l}C_l^{k+1}] \tag{5.60}$$

In the above equation, for every element the last point concentration value of one element should exactly be the same as that of the first point of the next element due to continuity.

$$C_{NP+2}^k = C_1^{k+1} \tag{5.61}$$

Since the two different adsorbents (the biochar and soil particles) are well mixed in the column, I set the first two collocation points in the particle phase are always soil, while the next two collocation points in the particle phase are always biochar. They repeat by this way (Figure 5.3). Their volume ratios are accounted in the bulk fluid phase equation (5.56).

At each interior collocation point inside the soil particle solid phase in r direction,

$$[\varepsilon_{ps} + \frac{dq_s}{dc_{j,soil}^{i,k}}\rho_{as}(1-\varepsilon_{ps})]\frac{dc_{j,soil}^{i,k}}{d\tau} - \frac{1}{Pe_{ps}}\frac{L}{r_{ps}}[\sum_{l=1}^{l=NR+1} BR_{j,l}c_{l,soil}^{i,k}] = 0 \tag{5.62}$$

k is the number of each element. i is the number of z direction each interior collocation point. j is the number of each interior collocation point in r direction.

Boundary Conditions:

$$\rho = 0: \sum_{l=1}^{l=NR+1} AR_{1,l}c_{l,soil}^{i,k} = 0 \tag{5.63}$$

$$\rho = 1: \sum_{l=1}^{l=NR+1} AR_{NR+1,l}c_{l,soil}^{i,k} = Bi_s(C_i^k - c_{NR+1,soil}^{i,k}) \tag{5.64}$$

Initial Conditions:

$$\tau = 0: \quad C_{j,soil}^{i,k}(\tau,\rho) = C_{input} \tag{5.65}$$

For biochar particles, similarly I can get:

$$[\varepsilon_{pc} + \frac{dq_c}{dc_{j,char}^{i,k}}\rho_{ac}(1-\varepsilon_{pc})]\frac{dc_{j,char}^{i,k}}{d\tau} - \frac{1}{Pe_{pc}}\frac{L}{r_{pc}}[\sum_{l=NR+2}^{l=2NR+2} BR_{j,l-NR-1}c_{l,char}^{i,k}] = 0 \tag{5.66}$$

Boundary Conditions:

$$\rho = 0: \sum_{l=NR+2}^{l=2NR+2} AR_{NR+2,l-NR-1}c_{l,char}^{i,k} = 0 \tag{5.67}$$

$$\rho = 1: \sum_{l=NR+2}^{l=2NR+2} AR_{2NR+2,l-NR-1}c_{l,char}^{i,k} = Bi_c(C_i^k - c_{2NR+2,char}^{i,k}) \tag{5.68}$$

Initial Conditions:

$$\tau = 0: \quad C_{j,char}^{i,k}(\tau,\rho) = C_{input} \tag{5.69}$$

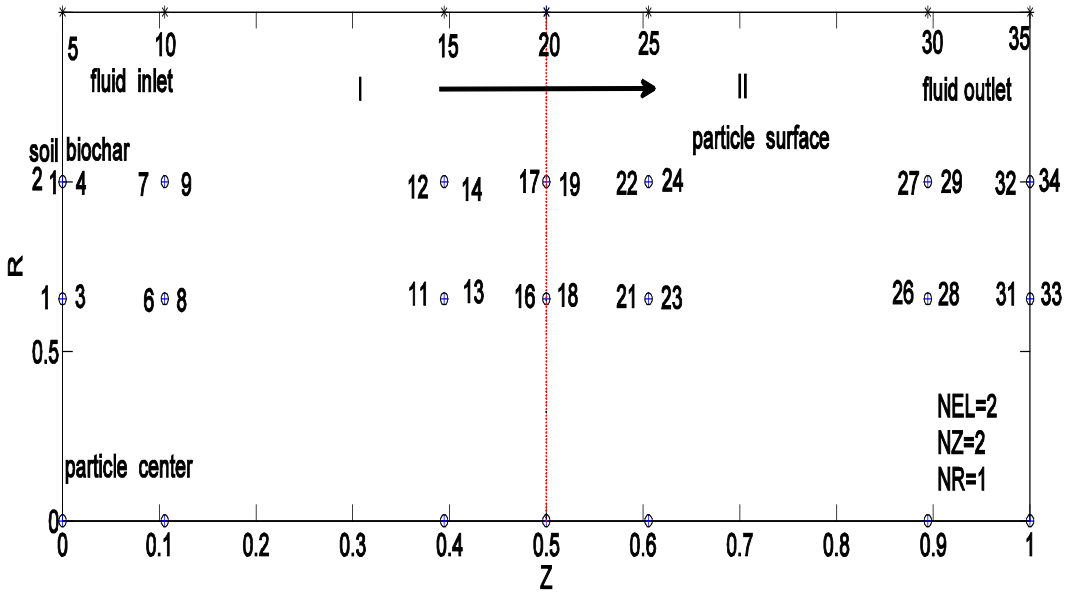

Figure 5.3 Grid points and numbering for OCFE with Nel=2, NP=2, NR=1 for domain discretization

One concern is that DASSL requires consistent initial values and their derivatives. Therefore, instead of using step change concentration as the boundary conditions, I use the following continuous change of the input concentration as the boundary conditions:

Adsorption: $C_{input} = C_{input} - C_{input} \exp(-10^{10} * \tau)$ (5.70)

Desorption: $C_{input} = C_{input} \exp(-10^{10} * \tau)$ (5.71)

The average concentration throughout the biochar adsorbent particle is defined as:

$$\overline{w_{pc}} = \frac{\int_0^1 \rho^2 [(1-\varepsilon_{pc})\rho_{ac} \frac{q_{mc} b_c C_{pc}}{1+b_c C_{pc}} + \varepsilon_{pc} C_{pc}] d\rho}{\rho_{ac} \int_0^1 \rho^2 d\rho} \tag{5.72}$$

Similarily, the average concentration throughout the soil adsorbent particle is defined as:

$$\overline{w_{ps}} = \frac{\int_0^1 \rho^2 [(1-\varepsilon_{ps})\rho_{as} \frac{q_{ms} b_s C_{ps}}{1+b_s C_{ps}} + \varepsilon_{ps} C_{ps}] d\rho}{\rho_{as} \int_0^1 \rho^2 d\rho} \tag{5.73}$$

The above defined average concentration throughout the biochar/soil adsorbent particle are used to calculate the packed bed capacity.

The packed bed weight capacity per volume is defined as:

$$\overline{W} = \overline{Q_{soil}} + \overline{Q_{char}} + \overline{C} = \overline{W_{soil-particle}} + \overline{W_{biochar-particle}} + \overline{W_{fluid}} \tag{5.74}$$

Adsorbed solute in soil is defined as:

$$\overline{Q_{soil}} = \frac{\mathrm{M_A} * S \int_0^L [(1-\varepsilon_b)\rho_{as} \frac{V_{soil}}{V_{char}+V_{soil}} \overline{q_{ps}}] dx}{S \int_0^L dx} \tag{5.75}$$

Adsorbed solute in biochar is defined as:

$$\overline{Q_{char}} = \frac{\mathrm{M_A} * S\int_0^L [(1-\varepsilon_b)\rho_{ac}\frac{V_{char}}{V_{char}+V_{soil}}\overline{q_{pc}}]dx}{S\int_0^L dx} \tag{5.76}$$

Free solute in the packed bed is defined as:

$$\overline{C} = \frac{\mathrm{M_A} * S\int_0^L [\varepsilon_b C + (1-\varepsilon_b)\rho_{as}\frac{V_{soil}}{V_{char}+V_{soil}}\overline{c_{ps}} + (1-\varepsilon_b)\rho_{ac}\frac{V_{char}}{V_{char}+V_{soil}}\overline{c_{pc}}]dx}{S\int_0^L dx} \tag{5.77}$$

Solute in soil particle is defined as:

$$\overline{W_{soil-particle}} = \frac{\mathrm{M_A} * S\int_0^L [(1-\varepsilon_b)\rho_{as}\frac{V_{soil}}{V_{char}+V_{soil}}(\overline{w_{ps}})]dx}{S\int_0^L dx} \tag{5.78}$$

Solute in biochar particle is defined as:

$$\overline{W_{biochar-particle}} = \frac{\mathrm{M_A} * S\int_0^L [(1-\varepsilon_b)\rho_{ac}\frac{V_{char}}{V_{char}+V_{soil}}(\overline{w_{pc}})]dx}{S\int_0^L dx} \tag{5.79}$$

Solute in bulk fluid of in the packed bed is defined as:

$$\overline{W_{fluid}} = \frac{\mathrm{M_A} * S\int_0^L (\varepsilon_b C)dx}{S\int_0^L dx} \tag{5.80}$$

Total solute in the packed bed is defined as:

$$\overline{W} = \frac{\mathrm{M_A} * S\int_0^L [(1-\varepsilon_b)\rho_{as}\frac{V_{soil}}{V_{char}+V_{soil}}\overline{w_{ps}} + (1-\varepsilon_b)\rho_{ac}\frac{V_{char}}{V_{char}+V_{soil}}\overline{w_{pc}} + \varepsilon_b C]dx}{S\int_0^L dx} \tag{5.81}$$

where $\overline{W}$ is the loading capacity of NH_4NO_3 in the column (kg/m^3), $\overline{Q_{soil}}$ is the loading capacity of NH_4NO_3 in the column soil solid phase (kg/m^3), $\overline{Q_{char}}$ is the loading capacity of

NH_4NO_3 in the column biochar solid phase (kg/m^3), $\overline{C}$ is the loading capacity of NH_4NO_3 in the column pore phase (kg/m^3), $\overline{W_{soil-particle}}$ is the loading capacity of NH_4NO_3 in column soil particle (kg/m^3), $\overline{W_{biochar-particle}}$ is the loading capacity of NH_4NO_3 in column biochar particle (kg/m^3), $\overline{W_{fluid}}$ is the weight percent of NH_4NO_3 in the column bulk pore phase (kg/m^3), M_A is NH_4NO_3 molar mass(g/mol), $\overline{w_{ps}}$ is the average NH_4NO_3 in the soil particle (mol/kg), $\overline{q_{ps}}$ is the average NH_4NO_3 in the soil particle solid phase (mol/kg), $\overline{c_{ps}}$ is the average NH_4NO_3 in the soil particle pore phase (mol/kg), $\overline{w_{pc}}$ is the average NH_4NO_3 in the biochar particle (mol/kg), $\overline{q_{pc}}$ is the average NH_4NO_3 in the biochar particle solid phase (mol/kg), $\overline{c_{pc}}$ is the average NH_4NO_3 in the biochar particle pore phase (mol/kg).

5.1.3 Accuracy of the numerical solution

I solved the previous system of PDEs with different numbers of collocation points to check the accuracy of my numerical solutions. The bulk fluid PDE (equation 5.56-5.61) was discretized using 20 or 40 elements in the axial direction, and 3 or 5 interior collocation points in each element. The PDEs describing intraparticle mass balances (equation 5.62-5.69) were discretized using 1 element in the radial (r) direction with 3 or 5 interior collocation points. The numerical solution does not change when we increase the number of axial finite elements or collocation points (Figure 5.4).

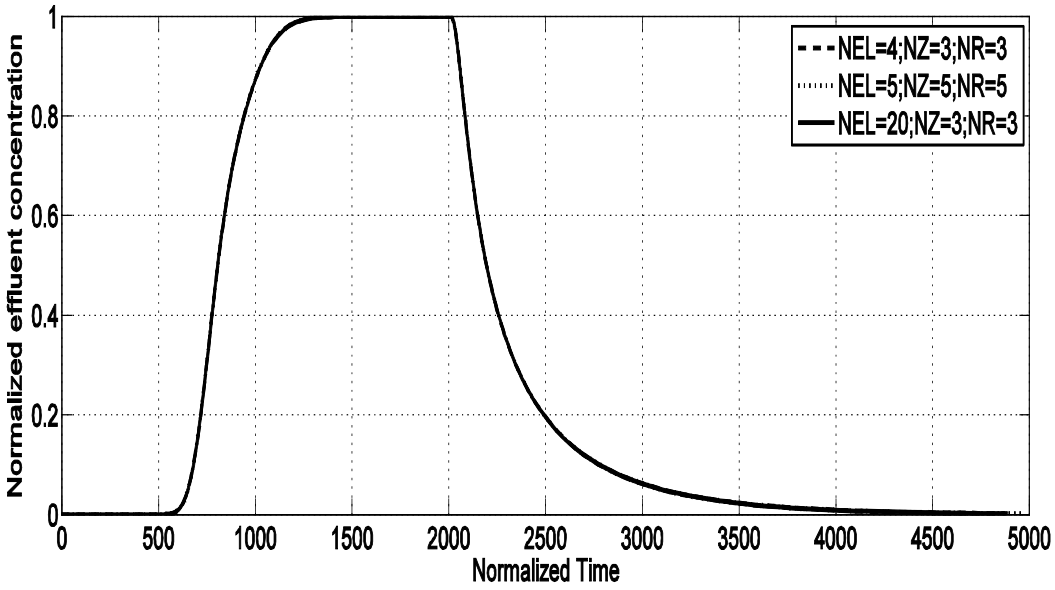

Figure 5.4 Numerical solutions computed with different numbers of collocation points

I also computed the relative error of the mass balance. The mass balance is defined as:

$$\frac{\overline{W}}{M_A} L = \int_0^t F_{input} dt - \int_0^t F_{output} dt = (C_{input} - C_{output}) u_s t \qquad (5.82)$$

The correspondent dimensionless function is:

$$\frac{\overline{W}}{M_A} = (C_{input} - C_{output}) \varepsilon_b \tau$$

where $\overline{W}$ is the loading capacity of NH_4NO_3 in the column (kg/m^3) defined in equation (5.81), C_{input} is the input concentration (mol/m^3), C_{output} is the output concentration (mol/m^3), F_{input} is the input flow rate ($mol/(m^2*s)$), F_{output} is the output flow rate ($mol/(m^2*s)$), u_s (m/s) is the superficial velocity, L (m) is the length of the column.

The relative mass balance error is around 10e-3 (Figure 5.5), which is acceptable. The mass balance check again shows that more elements and/or collocation points improve the numerical

solution accuracy. The relative mass balance errors decrease significantly with increasing the number of axial elements and/or collocation points.

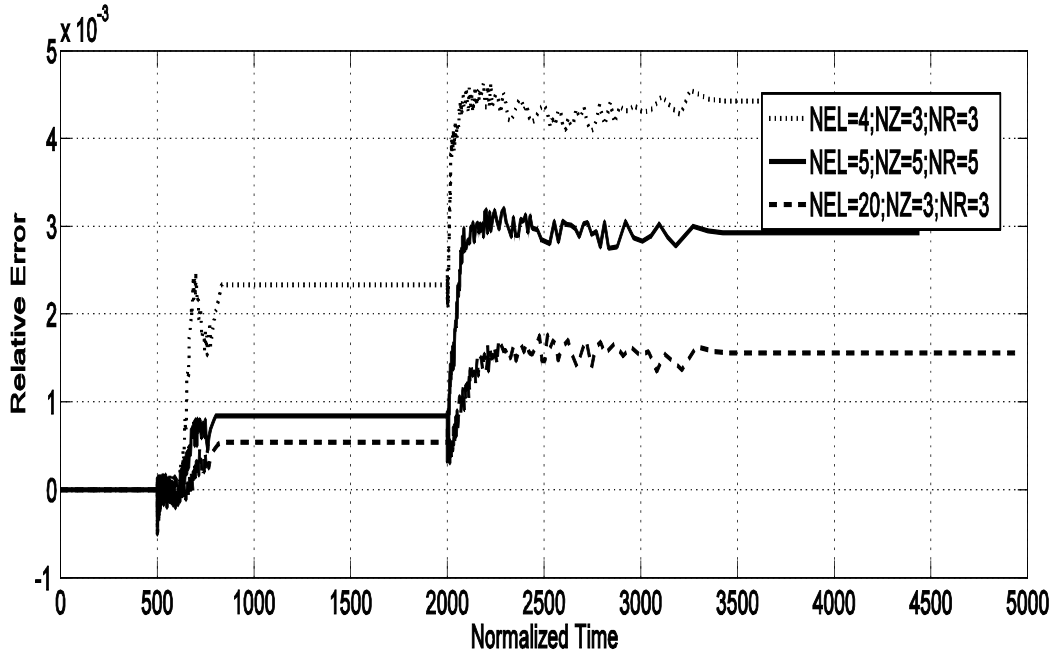

Figure 5.5 Numerical solution relative errors under different number of grid points

5.1.4 Numerical results

The typical adsorption/elution simulation experiment involves a rectangular pulse where the input nutrient concentration increases from zero to the required value, stays constant for certain hours to reach a N application equivalent to 100 kg/ha and drops back to zero after that (Figure 5.6).

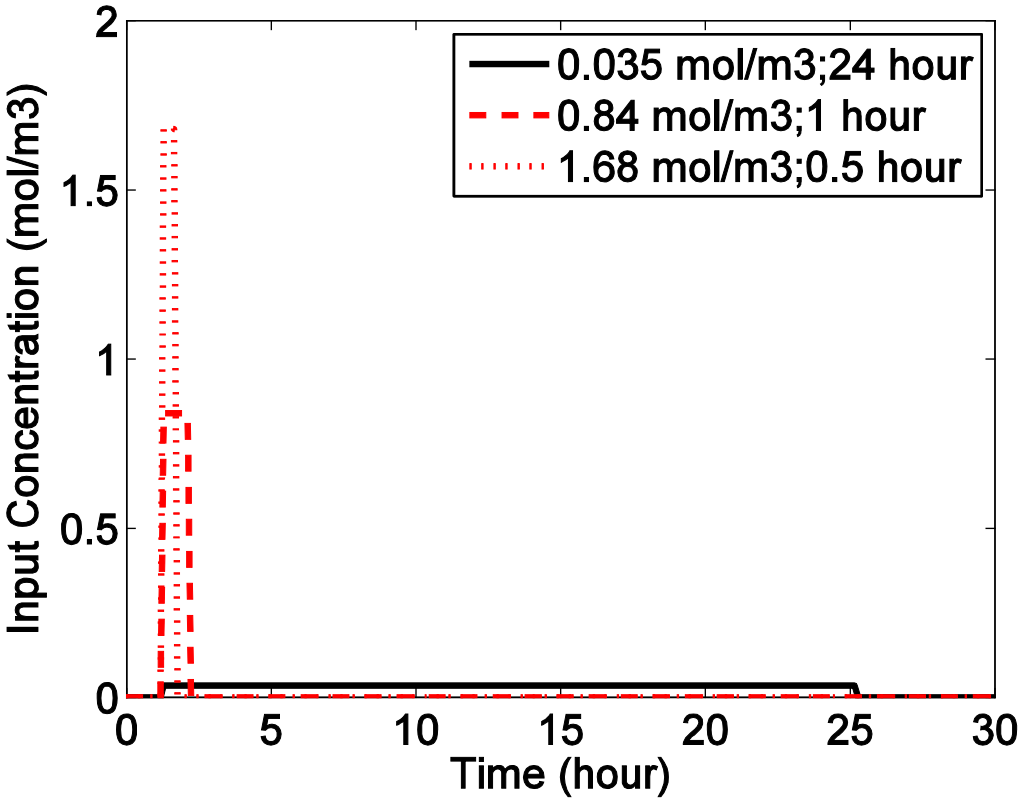

Figure 5.6 The input nutrient concentration

Due to adsorption of the nutrient on the soil, the output concentration (Figure 5.7) lags behind the input one (Figure 5.6). This lag does not become more pronounced when biochar is added to the column (Figure 5.9). This is because of the adsorption capacity of biochar I used is only 3 wt% - 11 wt% and the biochar[156]maxium adsorption capacity is just five times larger than that of the soil [157].Also the elution process starts before biochar fully saturated with nutrients. The elution process follows the same trend. Retardation in breakthrough curves is caused by adsorption of solute in the biochar and soil particles. This breakthrough curves will be compared with experimental breakthrough curves to identify transport parameter in the future (Figure 5.7 and 5.8). It is also interesting to note that low concentration but long input time makes the normalized effluent concentration (breakthrough) history curve nearly equal to one,

which means the column is fully saturated with low concentration solute (Figure 5.8). However, it is opposite for high concentration but short input time cases (Figure 5.8).

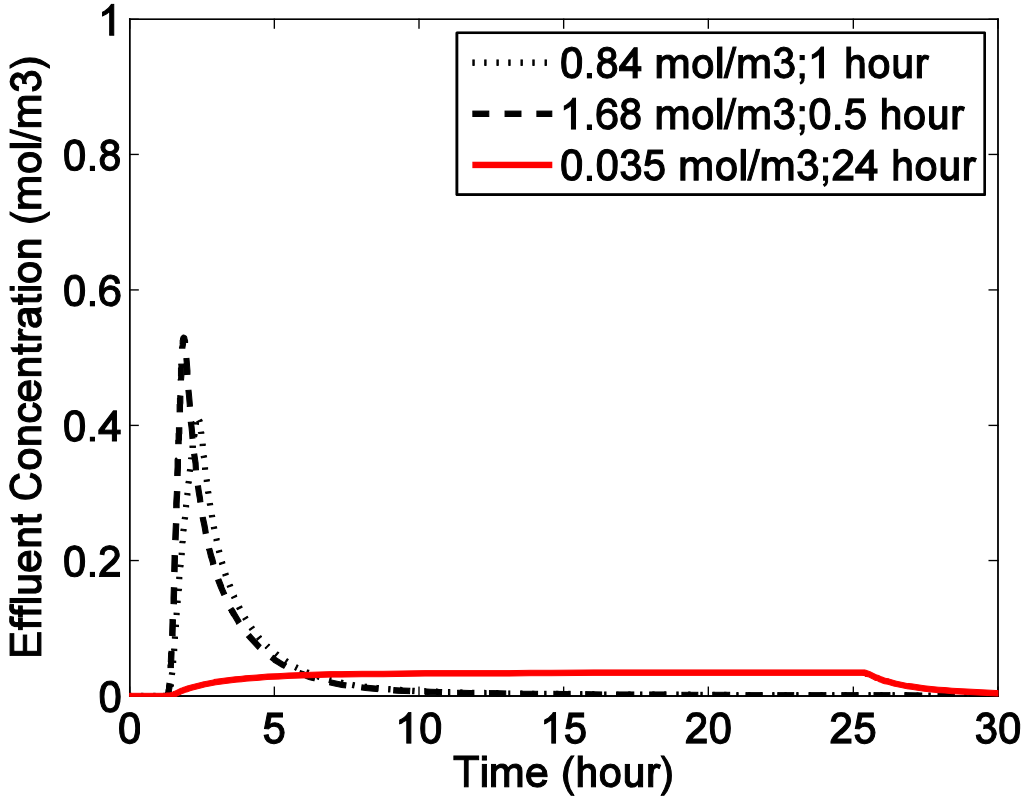

Figure 5.7 Effluent concentration (breakthrough) curve

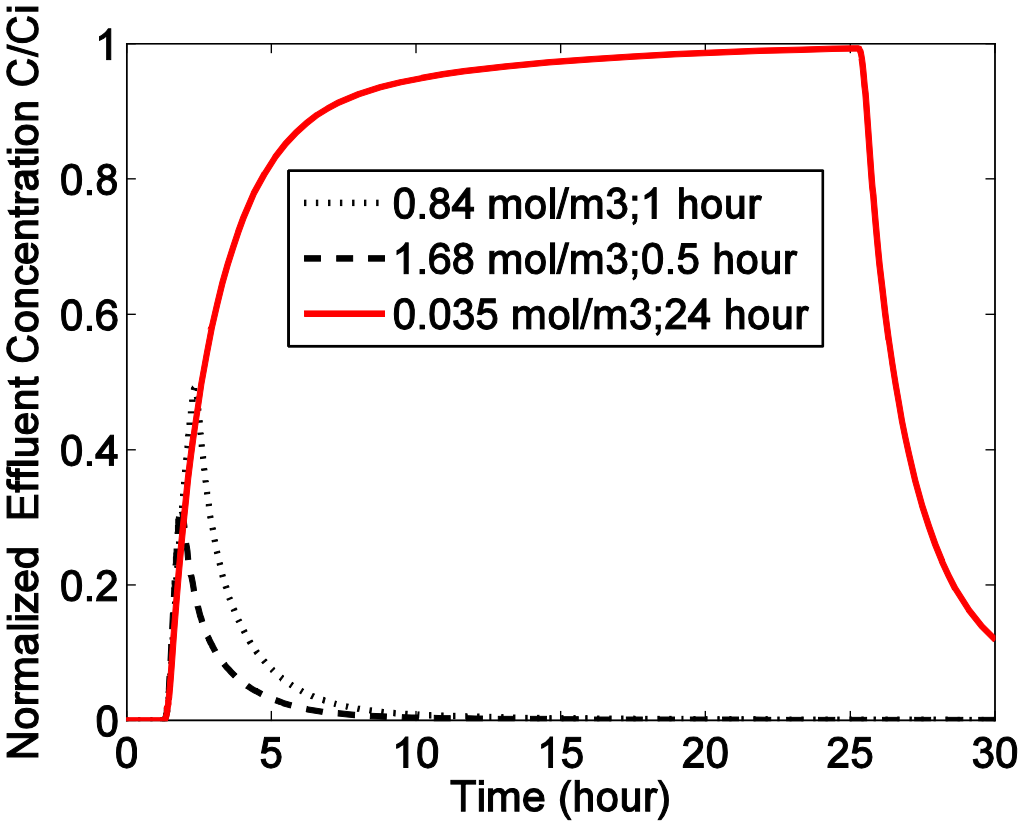

Figure 5.8 Normalized effluent concentration (breakthrough) history curve

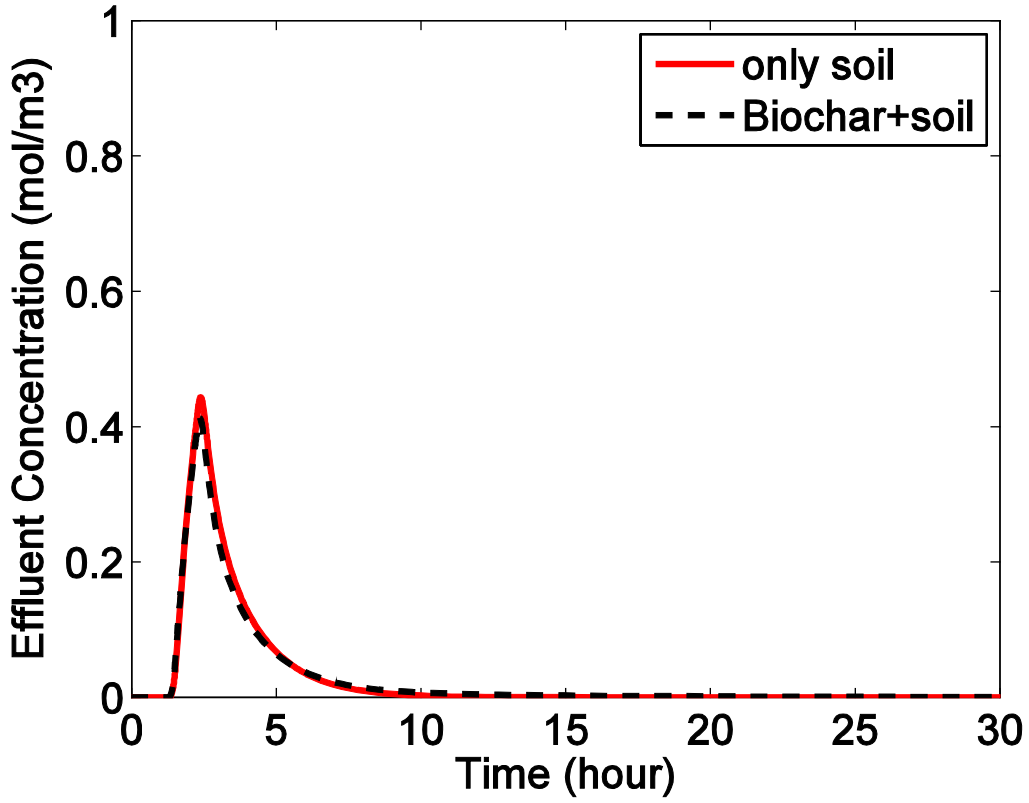

Figure 5.9 **Effluent concentration (breakthrough) curve for soil only (solid line) and and a biochar/soil mixture (dashed line) under 0.84mol/m^3 and 1hour solute input conditions**

During the adsorption phase, the nutrient concentration distribution profile moves from 0 concentration, to the intermediate t1 profile, and finally to maximum partially saturation t2 profile (Figure 5.10(a)). During the elution phase, the profile drops from maximum partially saturation t2 profile to 0 concentration (t6) profile again passing through the intermediate t3, t4and t5 profiles (Figure 5.10(b)). Biochar addition does not lead to longer saturation and elution times, as can be seen in Figure 5.10(c). To reach the same profile above, soil amended with biochar needs the same time compared to non-amended soil.

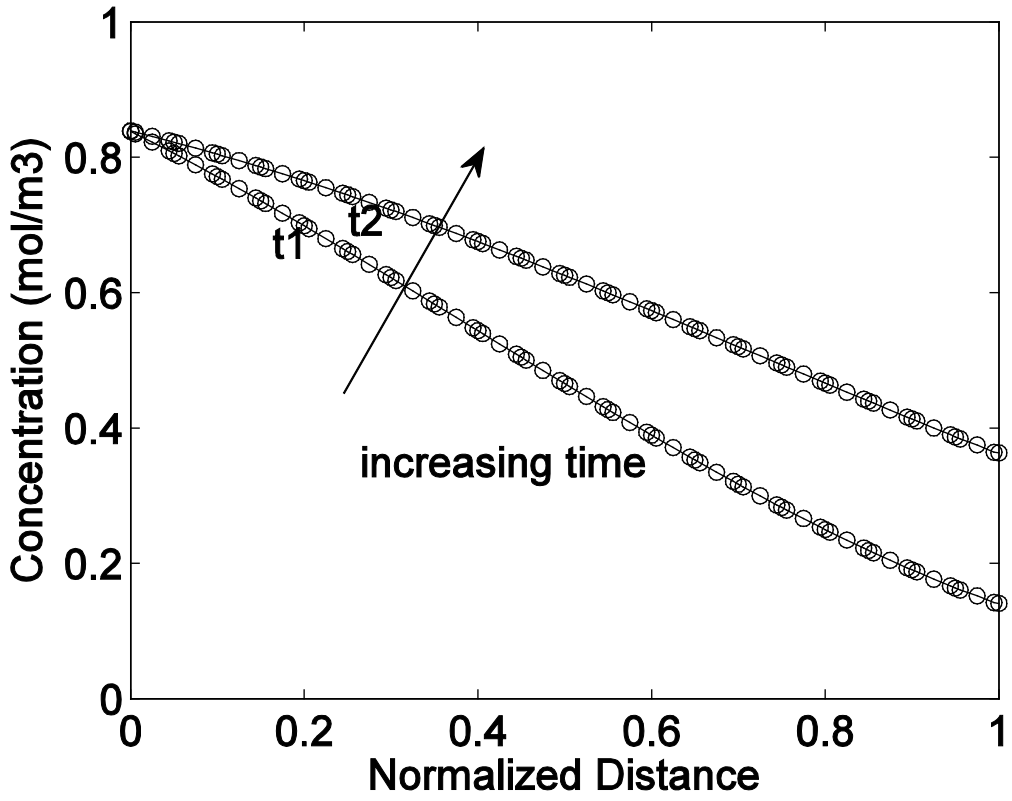

Figure 5.10(a) The concentration distribution profile at different time through the column during the adsorption phase

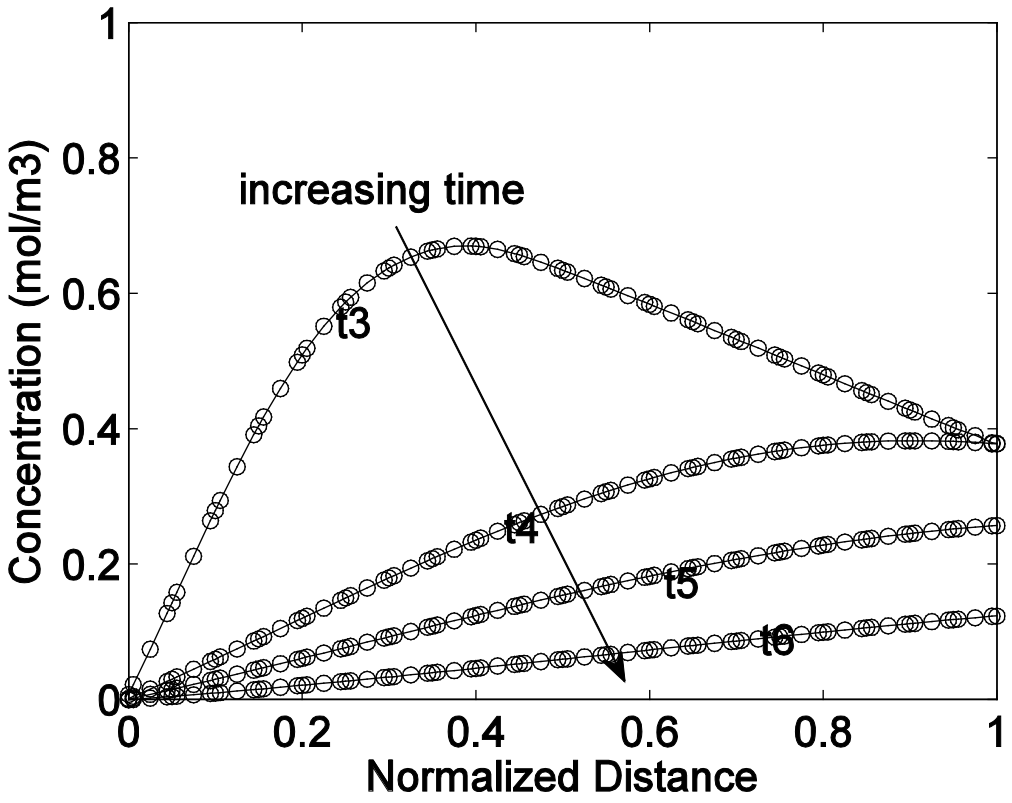

Figure 5.10(b) The concentration distribution profile at different time through the column during the elution phase

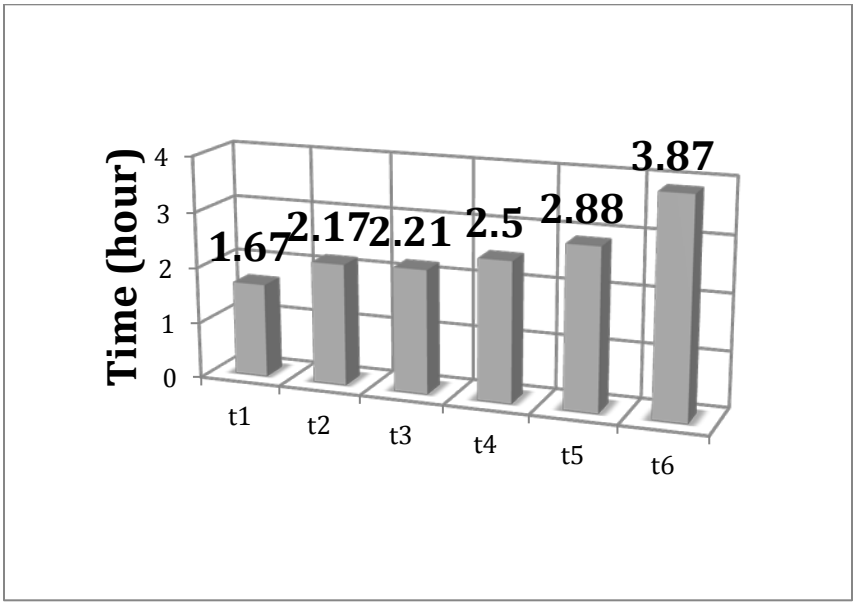

Figure 5.10(c) The correspondent time for different concentration distribution profiles through the column

By integrating along the bed the concentrations of solute in the pores and on the solid adsorbents, we can compute the total amount of nutrient retained in the column, and how it changes with time (Figure 5.11). The amount of nutrient in the liquid filling the pores (equation 5.80) plus that adsorbed on the pore surface of the absorbent (equation 5.78 and equation 5.79) gives the total amount retained in the column (equation 5.81). The plateau is the maximum adsorbate capacity.

A comparison of Figure 5.12 (biochar/soil mixture) to Figure 5.11 (pure soil) shows that the addition of 5wt% of biochar improves the ability of the column to hold nutrients. Furthermore, the soil/biochar mixture releases the adsorbed soil more slowly as indicated by the longer tail of the loding curve of Figure 5.12. Clearly, biochar addition increases the ability of the soil to retain nutrients even when we are below the maximum loading capacity. In both cases shown here (Figure 5.11-5.12), the vast majority of the nutrient is inside the particle and not in the liquid flowing through the interstices of the column. The effluent history of the biochar mixed with the soil is smaller than that of only soil column (Figure 5.13). Therefore, biochar amendment slows down the nutrient elution in soil.

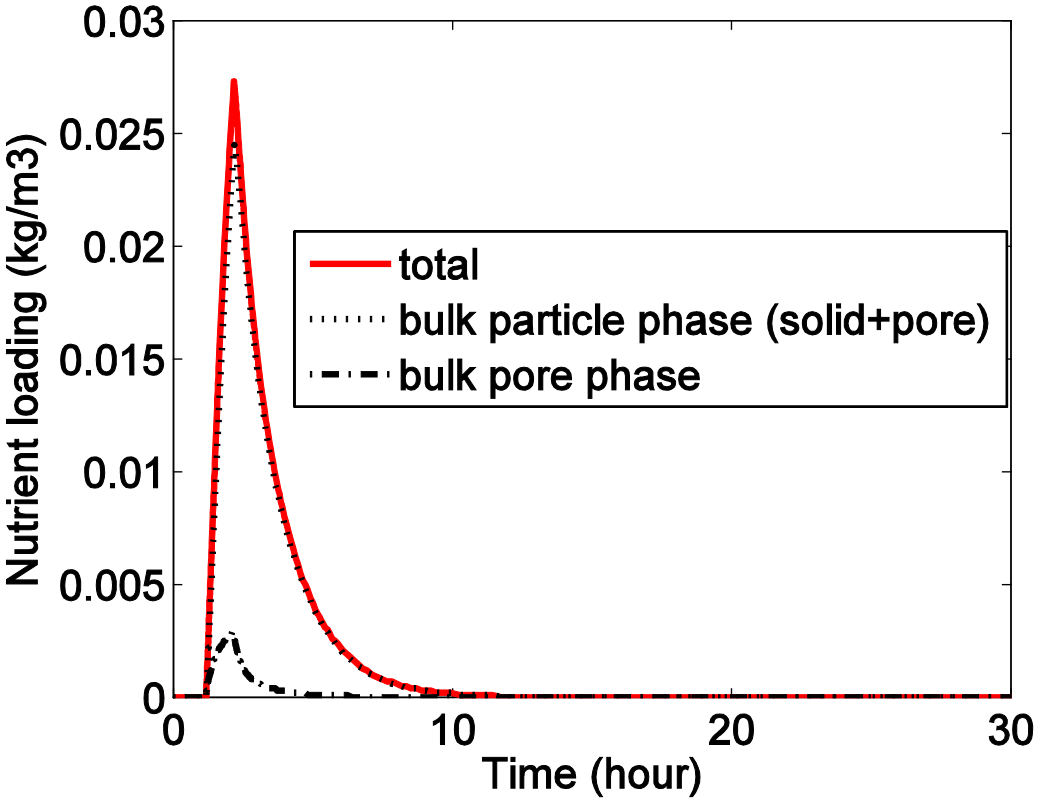

Figure 5.11 Amount of nutrient in the soil column

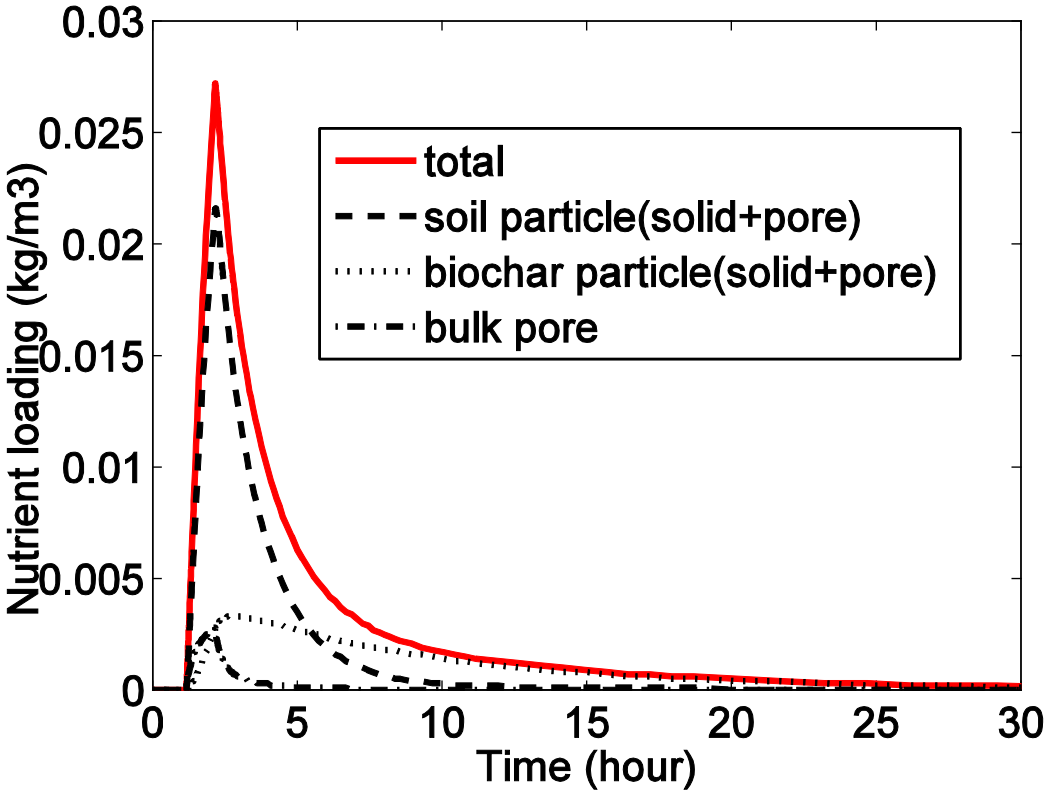

Figure 5.12 Adsorbed capacity (wt%) history of the biochar mixed with the soil column

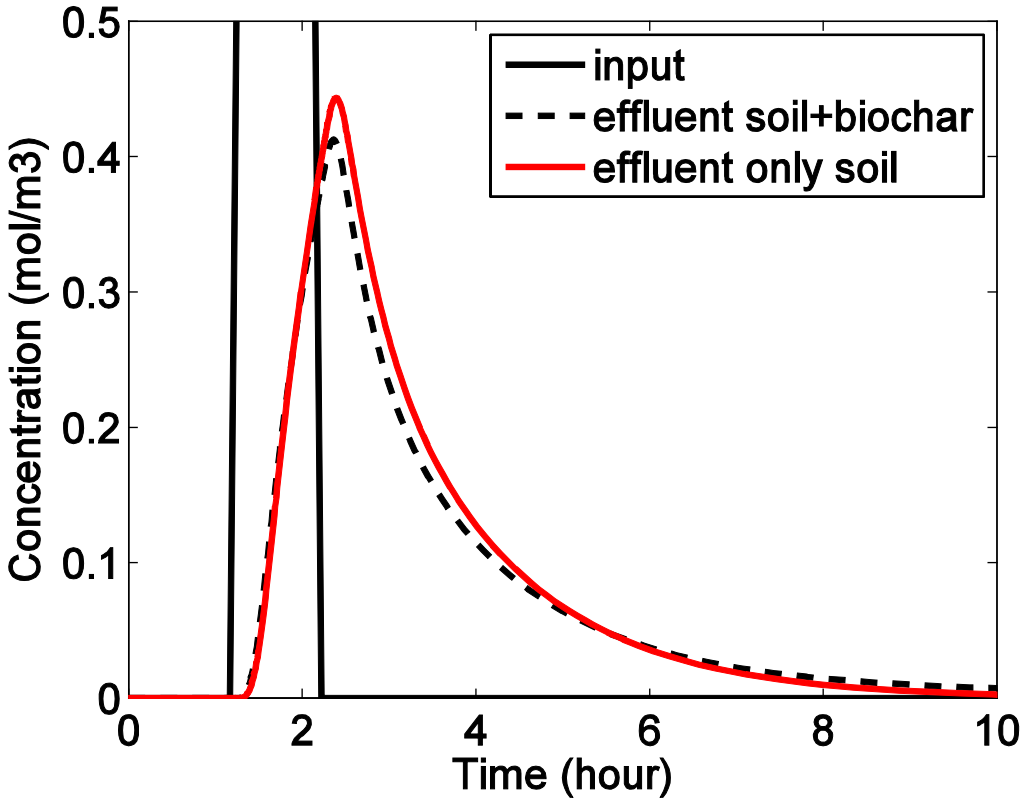

Figure 5.13 Effluent history of the biochar mixed with the soil and only soil column

Table 5.1 shows results from a systematic study aimed to determine whether there is an optimal irrigation pattern for biochar-amended soil that will maximize the amount of adsorbed nutrient. For these simulations, I keep constant the total amount of nutrient applied (equivalent to 100 kg N /ha) and vary the solute input concentration (mol/m^3) and the duration of the fertilization (hour)/(pore volume) (Table 5.1). The amount of nutrient in the liquid filling the pores is negligible compared to the amount observed on the pore surfaces (less than 2 %). By comparing N in solid of biochar per column volume (kg/m^3) and N total per column volume (kg/m^3) at the end of the fertilization pulse, I determine that 0.84mol/m^3 solute input and 1hour irrigation gives the best adsorption performance. The reason is that above this concentration (0.84mol/m^3), N total per column volume increases while N in solid of biochar per column

volume decreases. The increase is due to the N increase in pore fluid, which is not adsorded on soil or biochar surface. For high pore solute concentration, the Langmuir is at the platua stage, therefore, it almost reaches the maxium adsorption capacity. However, below this concentration ($0.84 mol/m^3$), I can not achieve a higher N total per column volume at the same time with higher N in solid of biochar per column volume. When the solute input concentration is too low, even we inject solute for long enough time to reach 100kg/ha. Due to the low pore solute concentration, the adsorbed solute amount is still low based on Langmuir isotherm (Figure 5.2). This optimum may change if we change the parameters of the biochar or the soil.

Table 5.1 Different irrigation effect

Solute input concentration (mol/m^3)	Input Duration (hour)/ (pore volume)	N in bulk fluid per column volume (kg/m^3)	N in soil per column volume (kg/m^3)	N in biochar per column volume (kg/m^3)	N total per column volume (kg/m^3)
8.4	0.1 /0.8548	0.0082	0.0235	0.0017	0.0334
1.68	0.5/ 4.2740	0.0043	0.0246	0.0023	0.0313
0.84	1 /8.548	0.0027	0.0216	0.0028	0.0272
0.28	3 /25.644	0.0011	0.0132	0.003	0.0174
0.14	6 /51.288	0.0006	0.0078	0.0027	0.0112
0.07	12 /102.576	0.0003	0.0041	0.0021	0.0065
0.035	24 /205.152	0.0001	0.0021	0.0013	0.0036

Table 5.2

Values of Key Parameters

PARAMETER	VALUES
Biochar amount (wt % of column)	3%, 5%, 11%
Biochar particle radius (mm)	0.2, 0.5, 1.0
Biochar adsorption affinity b (m^3/mol)	0.4, 2.25, 4.1
Biochar maxium adsorption capacity (mol/kg)	0.01, 0.05, 0.5
Biochar porosity	0.4, 0.6, 0.8

After determining the ideal irrigation conditions (0.84mol/m^3 solute input and 1hour irrigation), I have performed a battery of numerical experiments by varying biochar/soil weight ratio, particle radius, adsorption affinity and maxium adsorption capacity to see their impacts (Table 5.2). By changing the biochar weight ratio from 3-5-11wt%, higher biochar amendment levels lead to longer adsorbate release even it is partially saturated with nutrients (Figure 5.14).

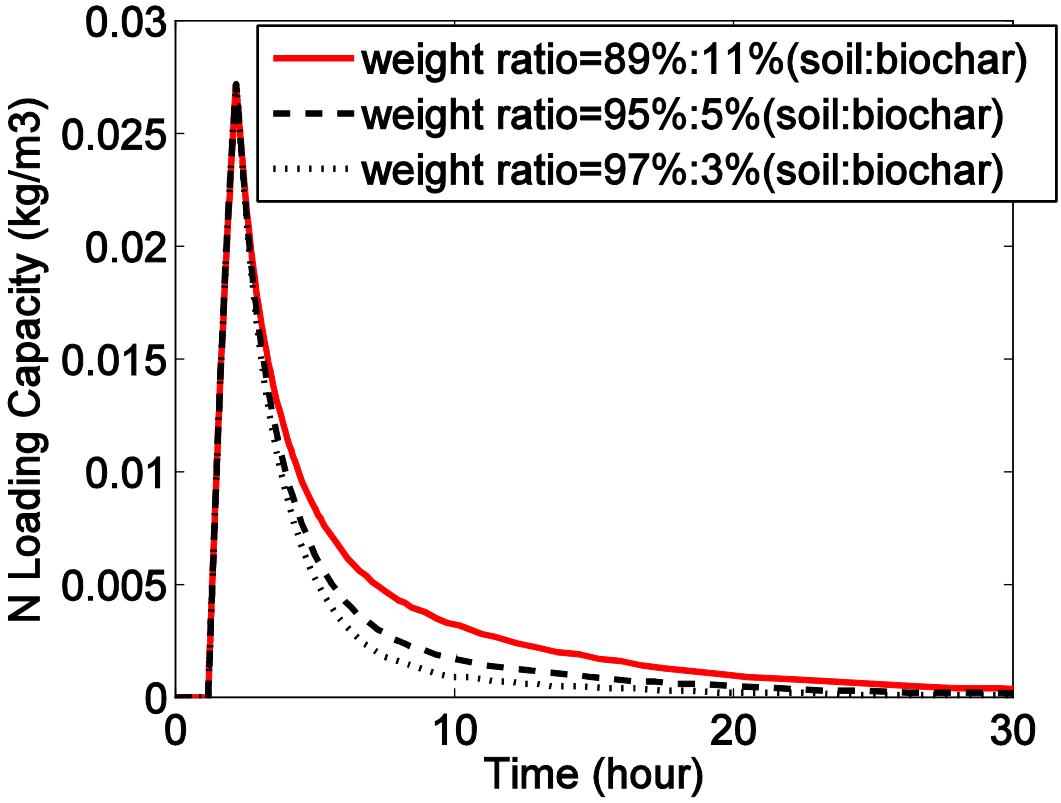

Figure 5.14 Effect of different adsorbents weight ratios on loading capacity (wt%) history of the whole column

By changing the biochar particle size from 0.2mm-0.5mm-1.0mm, smaller biochar particles lead to a more rapid adsorption/desorption process. Larger particles adsorb less N compared with smaller particles before releasing (Figure 5.15-16).

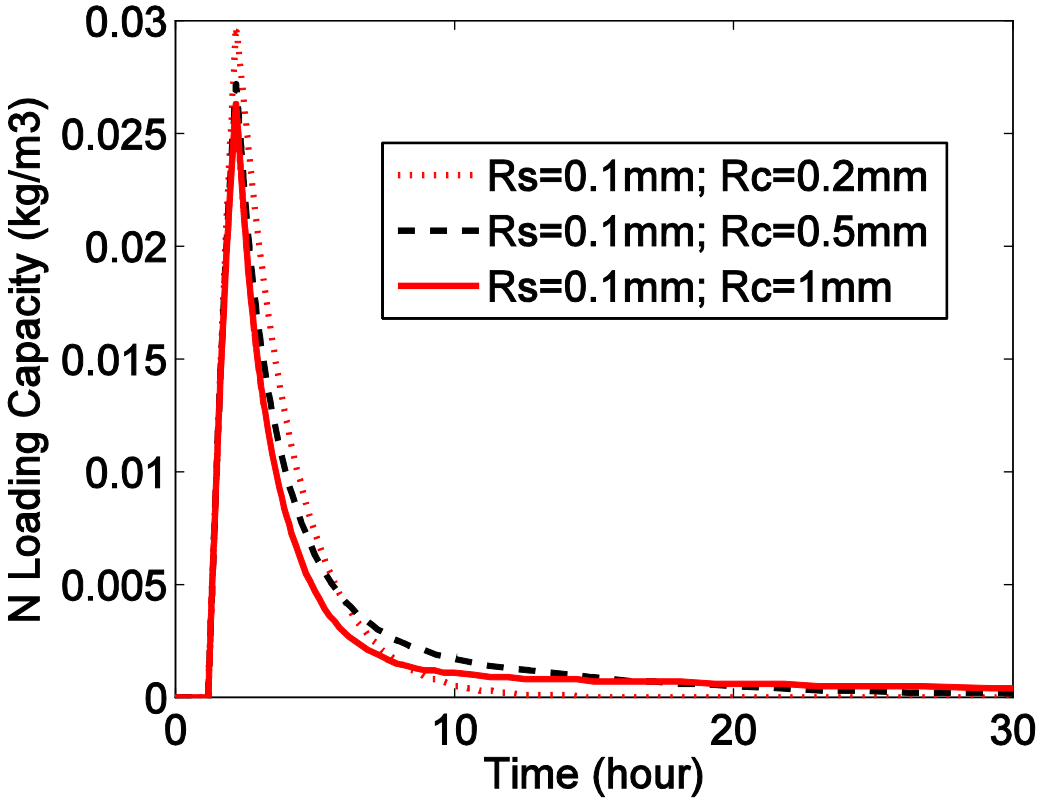

Figure 5.15 Effect of different biochar particle sizes on loading capacity (wt%) history of the whole column

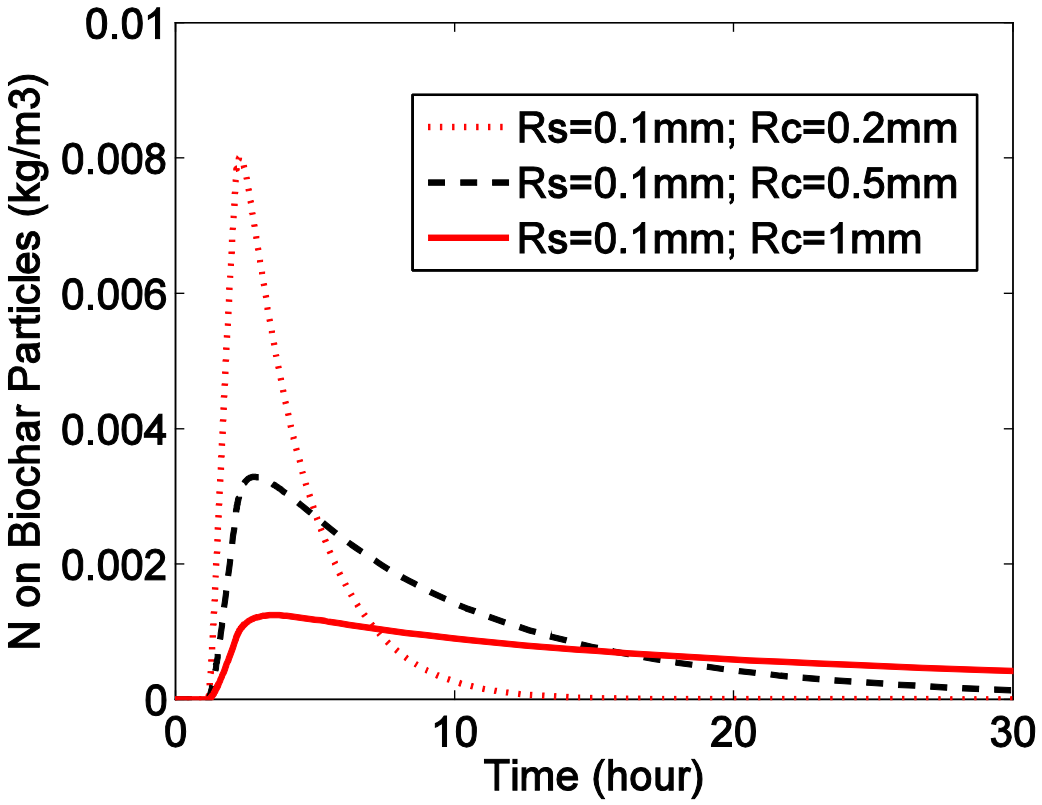

Figure 5.16 Effect of different biochar particle sizes on N on biochar particles (kg/m3) history

I use the Langmuir isotherm to study the relationship between nutrients in the pore phase and in the adsorbed phase of the adsorbent particle. By changing the biochar adsorption affinity (b) to get either the favorable adsorption or less favorable one, the favorable adsorption (the larger adsorption affinity (b)) speeds up adsorption and slows desorption (Figure 5.17). The adsorption rate seems the same because it is not a fully saturated process.

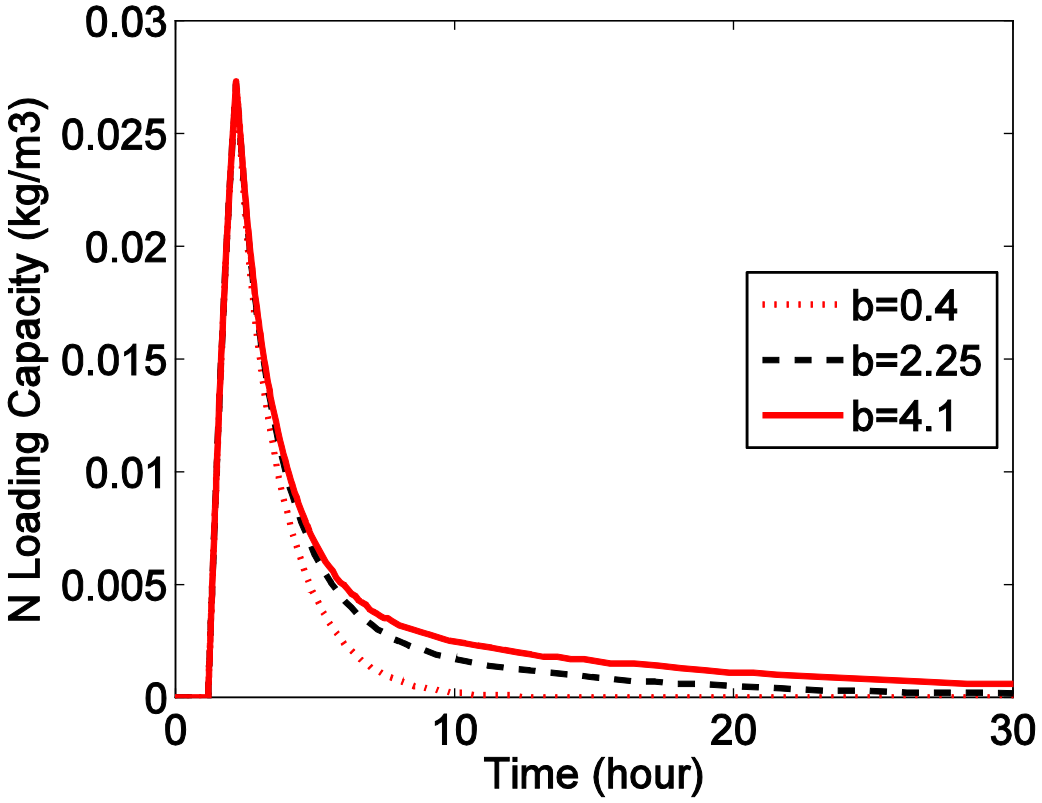

Figure 5.17 Effect of different biochar adsorption affinity (b) on loading capacity (wt%) history of the whole column

Lower porosities lead to smaller intraparticle diffusion coefficients, which leads to slower adsorption (Figure 5.18-19). Also as demonstrated before, the majority contribution to total loading is from the adsorbent particles instead of the pore phase. Therefore, low porosity increases mass adsorbed.

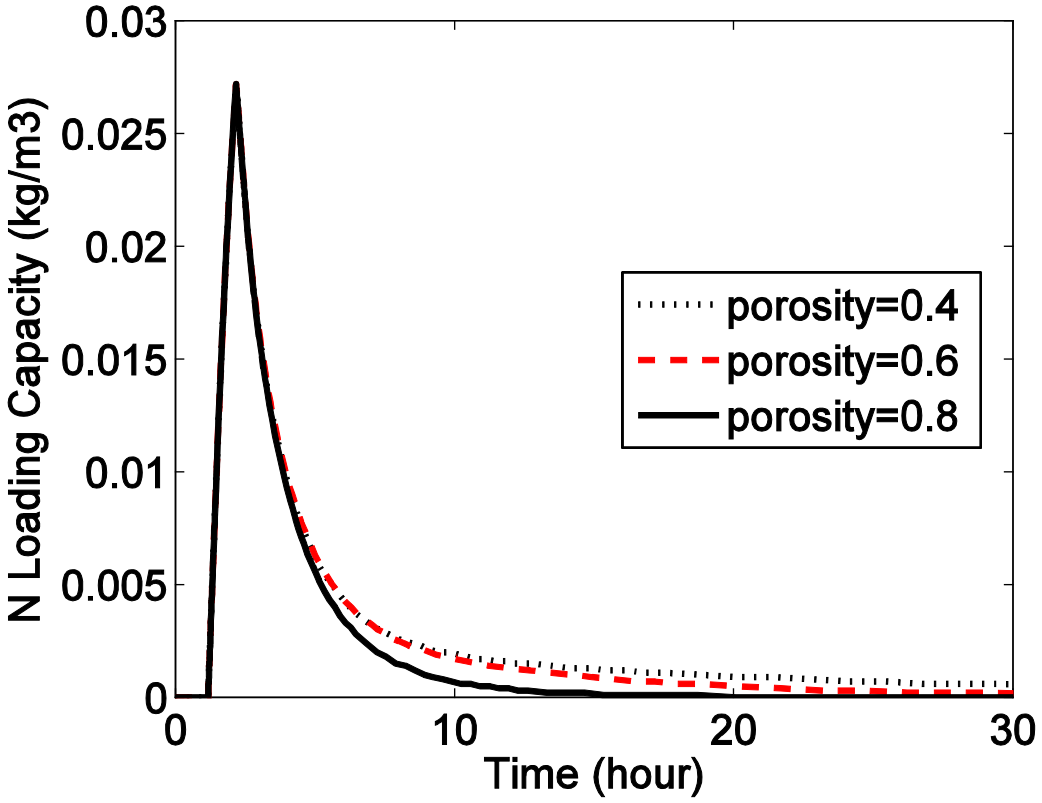

Figure 5.18 Effect of different biochar porosity on loading capacity (wt%) history of the whole column

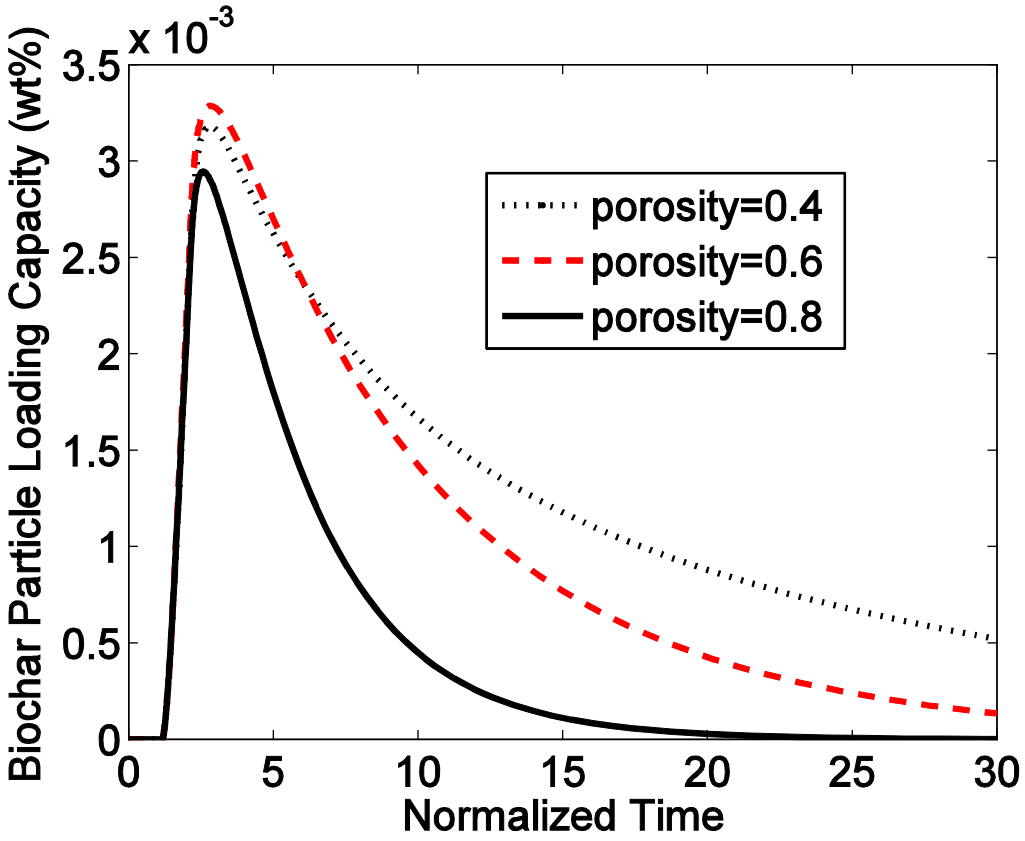

Figure 5.19 Effect of different biochar porosity on loading capacity (wt%) history of the whole column

High biochar maxium adsorption capacity leads to longer release of solute, since it has larger adsorption capacity (Figure 5.20).

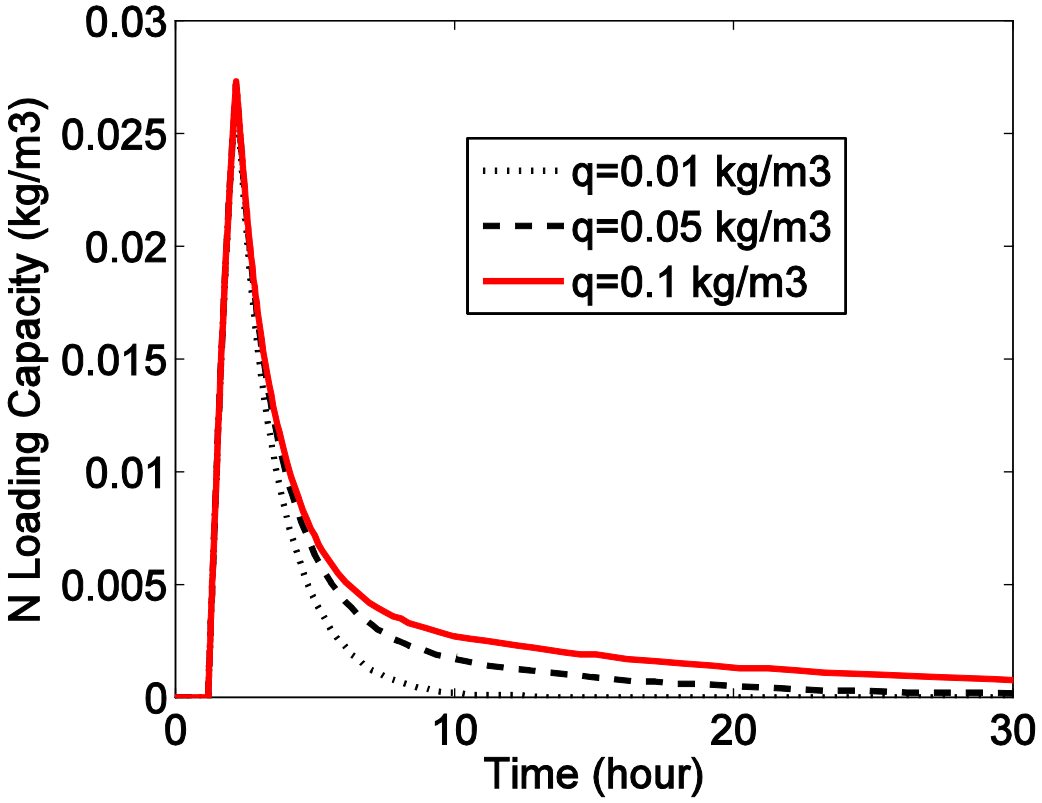

Figure 5.20 Effect of different biochar maxium adsorption capacity on loading capacity (wt%) history of the whole column

Parameter identification and correlations using breakthrough curves (sensitivity analysis)

As discussed above, the breakthrough curves from numerical simulation will be compared with experimental breakthrough curves to identify transport parameters in the future. Here I show an example of the whole process.

Soil Biot number Bi_s (equation 5.33), Peclet number in the bulk phase Pe_b (equation 5.34) and Peclet number of the soil particle Pe_{ps} (equation 5.36) determine the performance of the mass transport model for only the soil adsorbent system, which are functions of k_{fs}, D_{ps}, and D_L. To derive the optimal values of model parameters, an error function $F(p)$, which is defined

as the sum of square deviations of the predicted normalized output concentrations history curve (breakthrough) with respect to the experimental measured ones, was used as the objective function for the optimization [184]:

$$F(p) = \min \sum_{j=1}^{m} [\frac{C_{j,\exp}}{C^o} - \frac{C_{j,\mathrm{mod}}}{C^o}]^2 \tag{5.84}$$

where $C_{j,\exp}$ and $C_{j,\mathrm{mod}}$ are the experimental value and model prediction at point j of the breakthrough curve, respectively. By minimizing $F(p)$, the dimensionless numbers of the (Bi_s), (Pe_b), and Pe_{ps} can be determined. The values of the (k_f), (D_p), and D_L can be determined too. I use the UNLSF subroutine from IMSL® Fortran Numerical Math Library to attain this goal. I list out an example here (Figure 5.21, Table 5.3).

Table 5.3:

Values of Key Parameters

	Initial Parameters	Optimized Parameters
Pe_b	4173	4203
Pe_p	1043	318.8
Bi	0.715	1.379

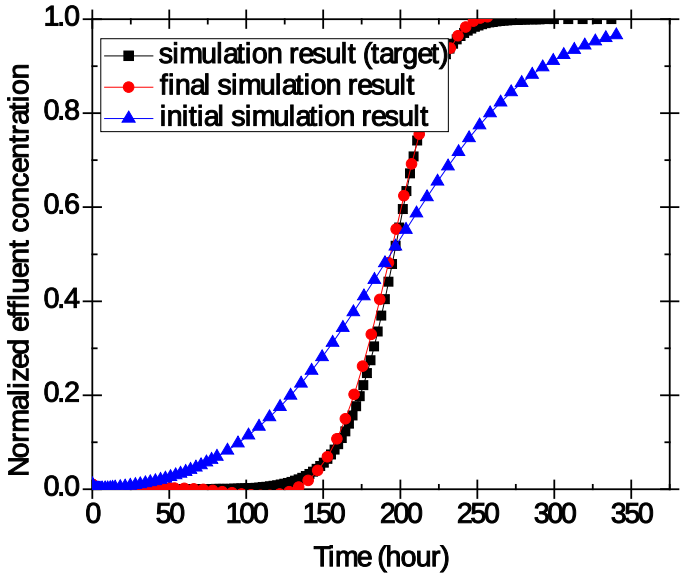

Figure 5.21 Sensitivity analysis of pore diffusion model

5.2 Models for the water flow through biochar/soil mixture porous media

Another of my objectives is to engineer biochars with optimal water holding properties. For this reason, I am developing and testing theoretical models that will help to quantify the effect of biochar properties on the dynamics water flow process of soil/biochar mixtures (Figure 5.99). The properties I consider include the biochar/soil weight ratio, biochar particle size and porosity. I start by considering the simple case of water flow into initially 20% water saturated system to cause concurrent air-water multiphase horizontal flow in bulk/soil porous media. Water is the invading and wetting phase. For the open column, it is a single phase flow problem (Richards' equation) by assuming air pressure does not change to neglect air (displaced phase) movement. As water moves through a packed bed of biochar/soil, the water will be transported from the bulk to the biochar/soil particles.

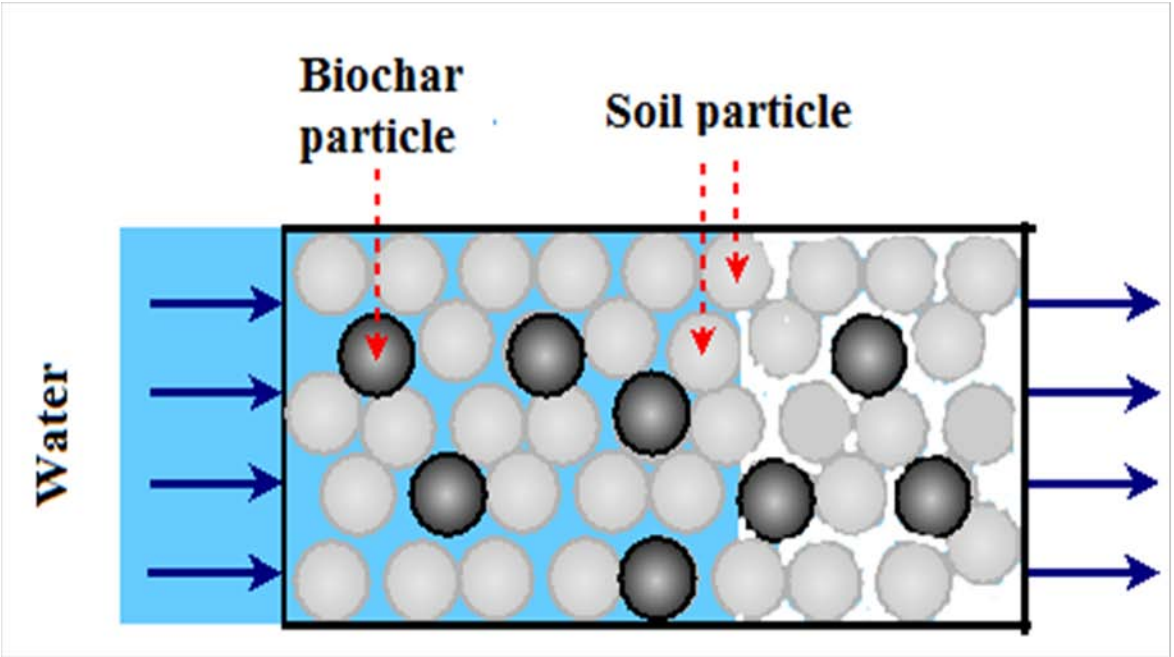

Figure 5.99 Schematic picture of the biochar/soil porous media under water flow conditions

5.2.1 Fluid dynamics model

All experimental capillary pressure data needs to be fitted to a certain model to avoid possible measurement noise. I use the Thomeer model to depict the relation between capillary pressure and water saturation for biochar/soil/bulk (Figure 5.100; Equation 5.101). I use an exponential model to depict the relation between relative permeability and water saturation for biochar/soil/bulk (Figure 5.101; Equation 5.102).

$$S_{i,D} = \frac{S_i - S_{ir}}{1 - S_{dr} - S_{ir}} \tag{5.100}$$

Drop the subscript D, saturation of invading phase $S_{i,D}$ defined by equation (5.100) is the S_i mentioned in this chapter, which avoids the influence from irriducible saturation of invading phase S_{ir} and irriducible saturation of displaced phase S_{dr} . S_b , S_c , S_s is the saturation for bulk/biochar and soil respectively.

$$P_C = C_1 \exp(-\frac{C_2}{\ln(1-S_i)}) \tag{5.101}$$

C_1 and C_2 are different measurable Thomeer model parameters for biochar/soil/bulk.

$$k_{ri} = k_{ri}^o S_i^{ni} \tag{5.102}$$

k_{ri}^o is end-point ($S_i = 1$) k_{ri}, which is different for biochar/soil/bulk.

ni is relative permeability exponent.

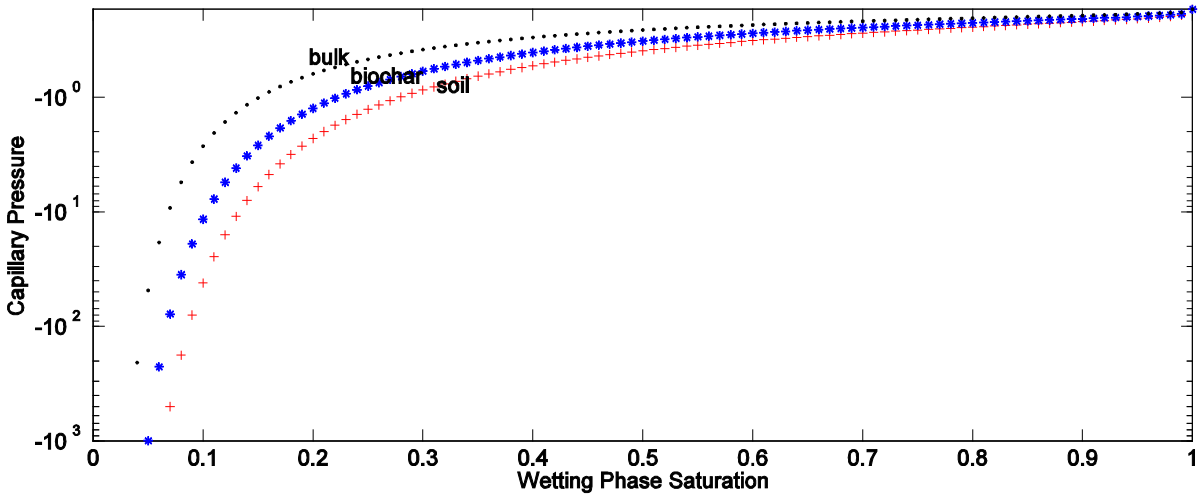

Figure 5.100 Capillary pressure-wetting fluid saturation relationship

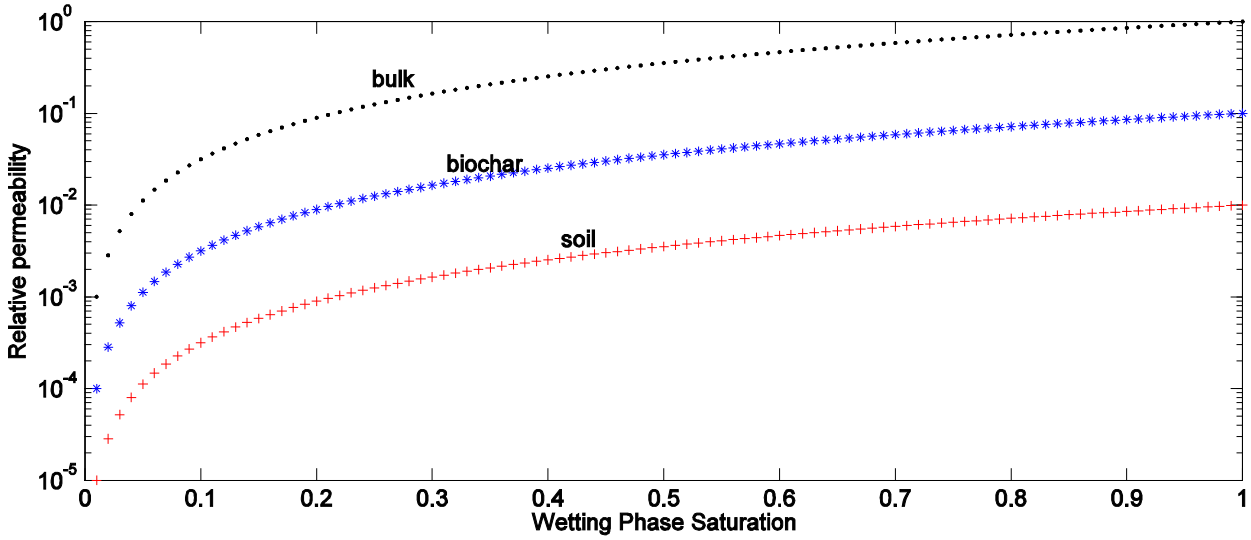

Figure 5.101 Relative permeability-wetting fluid saturation relationship

The derivation of the mass balance equations of our system is the following:

The overall water mass transfer in the column for the process is the following:

Rate of water enter by flow - water consumption = rate of water exit by flow + rate of accumulation of water in the fluid phase:

The resulting partial differential equation is:

Bulk phase:

$$u_b Sw_b\big|_x + A_{bs}\overline{u_{bs}}\big|_{\Delta x} + A_{bc}\overline{u_{bc}}\big|_{\Delta x} = u_b Sw_b\big|_{x+\Delta x} + \frac{\partial S_b}{\partial t}\varepsilon_b \Delta x Sw_b \tag{5.103}$$

Soil phase:

$$u_s Sw_s\big|_x + A_b\,\overline{u_{sb}}\big|_{\Delta x} = u_s Sw_s\big|_{x+\Delta x} + \frac{\partial S_s}{\partial t}\varepsilon_s \Delta x Sw_s \tag{5.104}$$

Biochar phase:

$$u_c Sw_c\big|_x + A_b\,\overline{u_{cb}}\big|_{\Delta x} = u_c Sw_c\big|_{x+\Delta x} + \frac{\partial S_c}{\partial t}\varepsilon_c \Delta x Sw_c \tag{5.105}$$

The “sugar cube” particle mass transfer term has been widely discussed before[185]. Similarily, for spherical particles,

$$q_{bs} = A_{bs}\overline{u_{bs}} = \varepsilon_s \frac{\partial S_s}{\partial t} = -\frac{1}{V_s}\int K_{bs}(h_b, h_s)\frac{\partial h_s}{\partial n}d\ {}_{bs}A = -\frac{1}{V_s}\int K_{bs}(h_b, h_s)\frac{h_s - h_b}{R_s}d\ {}_{bs}A = \frac{3}{R_s^2}K_{bs}(h_b, h_s)(h_b - h_s) \quad (5.106)$$

x is the axial coordinate of the column, S is the cross sectional area of the column, ε_c is the porosity of biochar, ε_s is the porosity of soil, ε_b is the porosity of bulk, w_c is the volumetric weighting factor of biochar, w_s is the volumetric weighting factor of soil, w_b is the volumetric weighting factor of bulk, $K_b = \frac{kk_{rb}\rho_w g}{\mu_w}$ (m/s) is the hydraulic conductvity of bulk, $h_b = \frac{P_b}{\rho_w g}$ (m) is the pressure head of bulk, $K_s = \frac{kk_{rs}\rho_w g}{\mu_w}$ (m/s) is the hydraulic conductvity of soil, $h_s = \frac{P_s}{\rho_w g}$ (m) is the pressure head of soil, $K_c = \frac{kk_{rc}\rho_w g}{\mu_w}$ (m/s) is the hydraulic conductvity of biochar, $h_c = \frac{P_c}{\rho_w g}$ (m) is the pressure head of biochar. u_b, u_s and u_c (m/s) is the superficial velocity of bulk/soil/biochar respectfully, following the Darcy’s law. $\overline{u_{bs}}$ (m/s) is the interchange velocity between bulk and soil. $\overline{u_{bc}}$ (m/s) is the interchange velocity between bulk and soil/biochar. $K_{bs}(h_b, h_s) = \frac{K_s(h_b) + K_s(h_s)}{2}$ (m/s) is the hydraulic interchange conductvity between bulk and soil. $K_{bc}(h_b, h_c) = \frac{K_c(h_b) + K_c(h_c)}{2}$ (m/s) is the hydraulic interchange conductvity between bulk and biochar. A_{bs} (m^2) is the interchange area between bulk and soil. A_{bc} (m^2) is the interchange area between bulk and biochar.I use the following notations for equation (5.106). They are

normally treated as geometric factors to account for the surface area of the soil/biochar particles per unit volume divided by the charactic length associated with the mass interchange between bulk and soil/biochar particles[185].

$$ss = \frac{3}{R_s^2} \; cc = \frac{3}{R_c^2} \tag{5.107}$$

$$u_s = -K_s(S_s)(\frac{\partial h_s}{\partial x}) \; , \; u_c = -K_c(S_c)(\frac{\partial h_c}{\partial x}) \; , \; u_b = -K_b(S_b)(\frac{\partial h_b}{\partial x}) \tag{5.108}$$

Make variables dimensionlized:

$$S_{i,D} = \frac{S_i - S_{ir}}{1 - S_{dr} - S_{ir}} \; , \; x_D = \frac{x}{L} \; , \; t_D = \frac{u_b^{BC} t}{L(1 - S_{dr} - S_{ir})} \; , \; K_{bD} = \frac{K_b(S_b)}{K_b^o} \; , \; K_{sD} = \frac{K_s(S_s)}{K_b^o} \; , \; K_{cD} = \frac{K_c(S_c)}{K_b^o} \; ,$$

$$h_{bD} = \frac{h_b}{h_b^*} \; , \; h_{sD} = \frac{h_s}{h_b^*} \; , \; h_{cD} = \frac{h_c}{h_b^*} \tag{5.109}$$

Charactic pressure is determined to eliminate the parameters from the inlet boundary conditions.

$$h_b^* = \frac{u_b^{BC} L}{K_b^o} \tag{5.110}$$

Drop the above subscript D, the resulting partial differential equation is:

Bulk phase:

$$\frac{\partial S_b}{\partial t} \varepsilon_b w_b = w_b \frac{\partial}{\partial x}(K_b \frac{\partial h_b}{\partial x}) - ssL^2 \frac{K_s(h_s) + K_s(h_b)}{2}(h_b - h_s) - ccL^2 \frac{K_c(h_c) + K_c(h_b)}{2}(h_b - h_c) \tag{5.111}$$

Soil phase:

$$\frac{\partial S_s}{\partial t} \varepsilon_s w_s = w_s \frac{\partial}{\partial x}(K_s \frac{\partial h_s}{\partial x}) - ssL^2 \frac{K_s(h_s) + K_s(h_b)}{2}(h_s - h_b) \tag{5.112}$$

Biochar phase:

$$\frac{\partial S_c}{\partial t} \varepsilon_c w_c = w_c \frac{\partial}{\partial x}(K_c \frac{\partial h_c}{\partial x}) - ccL^2 \frac{K_c(h_c) + K_c(h_b)}{2}(h_c - h_b) \tag{5.113}$$

Initial Conditions:

$$h_b(x,t=0) = h_s(x,t=0) = h_c(x,t=0) = -0.6235 \tag{5.114}$$

An initially uniform pressure head is set throughout bulk/soil/biochar, which means the fluid saturation discontinues among layers of different capillary pressure-water saturation charactics [186]. Under this initially uniform pressure head:

$$S_b(x,t=0) = 0.2; S_c(x,t=0) = 0.29; S_s(x,t=0) = 0.36 \tag{5.115}$$

Boundary Conditions:

$$u_b\big|_{x=0} = K_b^o; u_s\big|_{x=0} = K_s^o; u_c\big|_{x=0} = K_c^o \tag{5.116}$$

$$\frac{\partial h_b}{\partial x}\Big|_{x=0} = \frac{\partial h_s}{\partial x}\Big|_{x=0} = \frac{\partial h_c}{\partial x}\Big|_{x=0} = -1 \tag{5.117}$$

$$h_b\big|_{x=1} = h_s\big|_{x=1} = h_c\big|_{x=1} = 0 \tag{5.118}$$

The reseaon is that the capillary pressure at the outlet boundary is zero and we set the air pressure equal to the atmospheric pressure, which can be set as a constant equal to zero.

I prevent reverse flow of invading water phase by defining $K_b\big|_{x=1} = K_s\big|_{x=1} = K_c\big|_{x=1} = 0$ if

$h_b\big|_{x=1^-} < 0$ or $h_c\big|_{x=1^-} < 0$ or $h_s\big|_{x=1^-} < 0$.

This outlet boundary indicates that the water will never flow out until the potential is greater than zero near the outlet boundary. Therefore, the water fractional flow (so called “water cut”) keeps at zero until then.

5.2.2 Numerical solution method (finite volume)

Since it has been proved that the upstream weighting has better accuracy compared with the midpoint weighting and the downstream weighting[187], I use the one point upstream weighting to evaluate nonlinear coefficients:

$$K_b(h_{b,i}^{n+1}) = K_b(h_{b,i+0.5}^{n+1}) \ , K_b(h_{b,i-1}^{n+1}) = K_b(h_{b,i-0.5}^{n+1}) \ , \ K_s(h_{s,i}^{n+1}) = K_s(h_{s,i+0.5}^{n+1}) \ , K_s(h_{s,i-1}^{n+1}) = K_s(h_{s,i-0.5}^{n+1}) \ ,$$

$$K_c(h_{c,i}^{n+1}) = K_c(h_{c,i+0.5}^{n+1}) \ K_c(h_{c,i-1}^{n+1}) = K_c(h_{c,i-0.5}^{n+1}) \tag{5.119}$$

I use the implicit procedure (backward difference) to caculate h_i^{n+1} . This h_i^{n+1} was used to update $K\ (h_i^{n+1})$ using Equation (5.119). The nonlinear coefficients are dependent on pressure head. I perform the Picard's iteration to update them on each iteration of the pressure equations.

Implicit procedure

Bulk inlet boundary condition ($i = 1$)

$$\begin{aligned} S_b(h_{b,i}^{n+1,k+1}) - S_b(h_{b,i}^{n}) - \frac{\Delta t}{\Delta x \varepsilon_b} = \frac{\Delta t}{w_b \varepsilon_b} \{ & \frac{w_b}{\Delta x^2} K_b(h_{b,i}^{n+1,k}) h_{b,i+1}^{n+1,k+1} \\ & - [\frac{w_b}{\Delta x^2} K_b(h_{b,i}^{n+1,k}) + ssL^2 \frac{K_s(h_{b,i}^{n+1,k}) + K_s(h_{s,i+NZ}^{n+1,k})}{2} + ccL^2 \frac{K_c(h_{b,i}^{n+1,k}) + K_c(h_{c,i+2NZ}^{n+1,k})}{2}] h_{b,i}^{n+1,k+1} \\ & + ssL^2 \frac{K_s(h_{b,i}^{n+1,k}) + K_s(h_{s,i+NZ}^{n+1,k})}{2} h_{s,i+NZ}^{n+1,k+1} \\ & + ccL^2 \frac{K_c(h_{b,i}^{n+1,k}) + K_c(h_{c,i+2NZ}^{n+1,k})}{2} h_{c,i+2NZ}^{n+1,k+1} \} \end{aligned}$$

(5.120)

Bulk inteior ($2 \le i \le NZ - 1$)

$$S_b(h_{b,i}^{n+1,k+1}) - S_b(h_{b,i}^{n}) = \frac{\Delta t}{w_b \varepsilon_b}\{\frac{w_b}{\Delta x^2} K_b(h_{b,i}^{n+1,k}) h_{b,i+1}^{n+1,k+1}$$

$$-[\frac{w_b}{\Delta x^2}(K_b(h_{b,i}^{n+1,k}) + K_b(h_{b,i-1}^{n+1,k})) + ssL^2 \frac{K_s(h_{b,i}^{n+1,k}) + K_s(h_{s,i+NZ}^{n+1,k})}{2} + ccL^2 \frac{K_c(h_{b,i}^{n+1,k}) + K_c(h_{c,i+2NZ}^{n+1,k})}{2}] h_{b,i}^{n+1,k+1}$$

$$+ \frac{w_b}{\Delta x^2} K_b(h_{b,i}^{n+1,k}) h_{b,i-1}^{n+1,k+1}$$

$$+ ssL^2 \frac{K_s(h_{b,i}^{n+1,k}) + K_s(h_{s,i+NZ}^{n+1,k})}{2} h_{s,i+NZ}^{n+1,k+1}$$

$$+ ccL^2 \frac{K_c(h_{b,i}^{n+1,k}) + K_c(h_{c,i+2NZ}^{n+1,k})}{2} h_{c,i+2NZ}^{n+1,k+1}\}$$

(5.121)

Bulk outlet boundary condition ($i = NZ$)

$$S_b(h_{b,i}^{n+1,k+1}) - S_b(h_{b,i}^{n}) = \frac{\Delta t}{w_b \varepsilon_b}\{-[\frac{w_b}{\Delta x^2} K_b(h_{b,i-1}^{n+1,k}) + ssL^2 \frac{K_s(h_{b,i}^{n+1,k}) + K_s(h_{s,i+NZ}^{n+1,k})}{2} + ccL^2 \frac{K_c(h_{b,i}^{n+1,k}) + K_c(h_{c,i+2NZ}^{n+1,k})}{2}] h_{b,i}^{n+1,k+1}$$

$$+ \frac{w_b}{\Delta x^2} K_b(h_{b,i}^{n+1,k}) h_{b,i-1}^{n+1,k+1}$$

$$+ ssL^2 \frac{K_s(h_{b,i}^{n+1,k}) + K_s(h_{s,i+NZ}^{n+1,k})}{2} h_{s,i+NZ}^{n+1,k+1}$$

$$+ ccL^2 \frac{K_c(h_{b,i}^{n+1,k}) + K_c(h_{c,i+2NZ}^{n+1,k})}{2} h_{c,i+2NZ}^{n+1,k+1}\}$$

(5.122)

Soil inlet boundary condition ($i = NZ + 1$)

$$S_s(h_{s,i}^{n+1,k+1}) - S_s(h_{s,i}^{n}) - \frac{\Delta t}{\Delta x \varepsilon_s} = \frac{\Delta t}{w_s \varepsilon_s}\{\frac{w_s}{\Delta x^2} K_s(h_{s,i}^{n+1,k}) h_{s,i+1}^{n+1,k+1}$$

$$-[\frac{w_s}{\Delta x^2} K_s(h_{s,i}^{n+1,k}) + ssL^2 \frac{K_s(h_{s,i}^{n+1,k}) + K_s(h_{b,i-NZ}^{n+1,k})}{2}] h_{s,i}^{n+1,k+1} \quad (5.123)$$

$$+ ssL^2 [\frac{K_s(h_{s,i}^{n+1,k}) + K_s(h_{b,i-NZ}^{n+1,k})}{2}] h_{b,i-NZ}^{n+1,k+1}\}$$

Soil inteior ($NZ + 2 \le i \le 2NZ - 1$)

$$S_s(h_{s,i}^{n+1,k+1}) - S_s(h_{s,i}^{n}) = \frac{\Delta t}{w_s \varepsilon_s}\{\frac{w_s}{\Delta x^2} K_s(h_{s,i}^{n+1,k}) h_{s,i+1}^{n+1,k+1}$$

$$-[\frac{w_s}{\Delta x^2}(K_s(h_{s,i}^{n+1,k}) + K_s(h_{s,i-1}^{n+1,k})) + ssL^2 \frac{K_s(h_{s,i}^{n+1,k}) + K_s(h_{b,i-NZ}^{n+1,k})}{2}] h_{s,i}^{n+1,k+1} \quad (5.124)$$

$$+ \frac{w_s}{\Delta x^2} K_s(h_{s,i-1}^{n+1,k}) h_{s,i-1}^{n+1,k+1}$$

$$+ ssL^2 [\frac{K_s(h_{s,i}^{n+1,k}) + K_s(h_{b,i-NZ}^{n+1,k})}{2}] h_{b,i-NZ}^{n+1,k+1}\}$$

Soil outlet boundary condition ($i = 2NZ$)

$$S_s(h_{s,i}^{n+1,k+1}) - S_s(h_{s,i}^{n}) = \frac{\Delta t}{w_s \varepsilon_s}\{-[\frac{w_s}{\Delta x^2} K_s(h_{s,i-1}^{n+1,k}) + ssL^2 \frac{K_s(h_{s,i}^{n+1,k}) + K_s(h_{b,i-NZ}^{n+1,k})}{2}]h_{s,i}^{n+1,k+1}$$
$$+ \frac{w_s}{\Delta x^2} K_s(h_{s,i-1}^{n+1,k}) h_{s,i-1}^{n+1,k+1}$$
$$+ ssL^2[\frac{K_s(h_{s,i}^{n+1,k}) + K_s(h_{b,i-NZ}^{n+1,k})}{2}]h_{b,i-NZ}^{n+1,k+1}\} \quad (5.125)$$

Biochar inlet boundary condition ($i = 2NZ + 1$)

$$S_c(h_{c,i}^{n+1,k+1}) - S_c(h_{c,i}^{n}) - \frac{\Delta t}{\Delta x \varepsilon_c} = \frac{\Delta t}{w_c \varepsilon_c}\{\frac{w_c}{\Delta x^2} K_c(h_{c,i}^{n+1,k}) h_{c,i+1}^{n+1,k+1}$$
$$-[\frac{w_c}{\Delta x^2} K_c(h_{c,i}^{n+1,k}) + ccL^2 \frac{K_c(h_{c,i}^{n+1,k}) + K_c(h_{b,i-2NZ}^{n+1,k})}{2}]h_{c,i}^{n+1,k+1}$$
$$+ ccL^2[\frac{K_c(h_{c,i}^{n+1,k}) + K_c(h_{b,i-2NZ}^{n+1,k})}{2}]h_{b,i-2NZ}^{n+1,k+1}\} \quad (5.126)$$

Biochar inteior ($2NZ + 2 \le i \le 3NZ - 1$)

$$S_c(h_{c,i}^{n+1,k+1}) - S_c(h_{c,i}^{n}) = \frac{\Delta t}{w_c \varepsilon_c}\{\frac{w_c}{\Delta x^2} K_c(h_{c,i}^{n+1,k}) h_{c,i+1}^{n+1,k+1}$$
$$-[\frac{w_c}{\Delta x^2}(K_c(h_{c,i}^{n+1,k}) + K_c(h_{c,i-1}^{n+1,k})) + ccL^2 \frac{K_c(h_{c,i}^{n+1,k}) + K_c(h_{b,i-2NZ}^{n+1,k})}{2}]h_{c,i}^{n+1,k+1} \quad (5.127)$$
$$+ \frac{w_c}{\Delta x^2} K_c(h_{c,i-1}^{n+1,k}) h_{c,i-1}^{n+1,k+1}$$
$$+ ccL^2[\frac{K_c(h_{c,i}^{n+1,k}) + K_c(h_{b,i-2NZ}^{n+1,k})}{2}]h_{b,i-2NZ}^{n+1,k+1}\}$$

Biochar outlet boundary condition ($i = 3NZ$)

$$S_c(h_{c,i}^{n+1,k+1}) - S_c(h_{c,i}^{n}) = \frac{\Delta t}{w_c \varepsilon_c}\{-[\frac{w_c}{\Delta x^2} K_c(h_{c,i-1}^{n+1,k}) + ccL^2 \frac{K_c(h_{c,i}^{n+1,k}) + K_c(h_{b,i-2NZ}^{n+1,k})}{2}]h_{c,i}^{n+1,k+1}$$
$$+ \frac{w_c}{\Delta x^2} K_c(h_{c,i-1}^{n+1,k}) h_{c,i-1}^{n+1,k+1}$$
$$+ ccL^2[\frac{K_c(h_{c,i}^{n+1,k}) + K_c(h_{b,i-2NZ}^{n+1,k})}{2}]h_{b,i-2NZ}^{n+1,k+1}\} \quad (5.128)$$

Since we want to linearize $S_i^{n+1,k+1}$ in order to solve $h_i^{n+1,k+1}$ using direct instead of iteration method, we use following Newton-Raphson formulation [188].

$$S_i^{n+1,k+1} = S_i^{n+1,k} + \frac{dS_i}{dh}\Big|_{h_i^{n+1,k}} (h_i^{n+1,k+1} - h_i^{n+1,k}) \quad (5.129)$$

Then $\frac{dS_i}{dh}\Big|_{h_i^{n+1,k}} h_i^{n+1,k+1}$ will be put on the other side, thus affecting only the diagonal element of the matrix. This newly calculated $h_i^{n+1,k+1}$ was compared with previously calculated $h_i^{n+1,k}$. The whole procedure was repeated until $\max\left|h_i^{n+1,k+1} - h_i^{n+1,k}\right| < tol$.

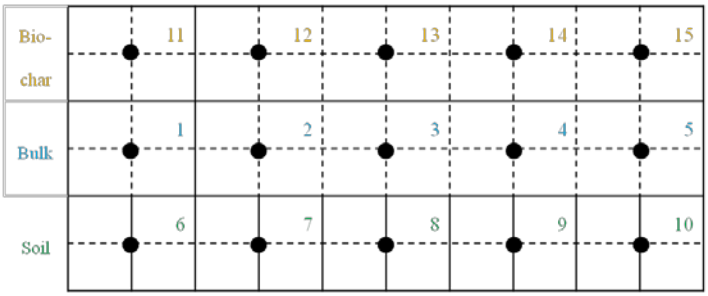

Figure 5.102 Standard row ordering of gridblocks (5*3)

	1	2	3	4	5	6	7	8	9	10	11	12	13	14	15
1	X	X				X					X				
2	X	X	X				X					X			
3		X	X	X				X					X		
4			X	X	X				X					X	
5				X	X					X					X
6	X					X	X								
7		X				X	X	X							
8			X				X	X	X						
9				X				X	X	X					
10					X				X	X					
11	X										X	X			
12		X									X	X	X		
13			X									X	X	X	
14				X									X	X	X
15					X									X	X

Figure 5.103 Shorthand notation for coefficients matrix (5*3)

I use the standard row ordering gridblocks (Figure 5.102)[187]. The pressure head is defined at the center of the grid block. The coefficients are evaluated at the faces between the grid blocks. It is a mass balance formulation. The correspondent matrix structure of bulk-soil-biochar is a heptadiagonal nonsymmetric sparse matrix (Figure 5.103). The correspondent matrix structure of bulk-soil is a pentadiagonal nonsymmetric sparse matrix inside (Figure 5.103). I use the nonsymmetric preconditioned bi-conjugate gradient method to solve it[189].

5.2.3 Numerical solutions verification

To verify the material balance, I calculate the recovery efficiency by two methods:

(a): by calculating the average value of water saturation;

(b): by calculating the cumulative result of air production.

$$(\partial S_b w_b \varepsilon_b + \partial S_s w_s \varepsilon_s + \partial S_c w_c \varepsilon_c) dx = -(w_b \partial u_b + w_s \partial u_s + w_c \partial u_c) dt \quad (5.130)$$

The material balance is guarented, since the absolute error history is within 10^{-4} (Figure 5.104).

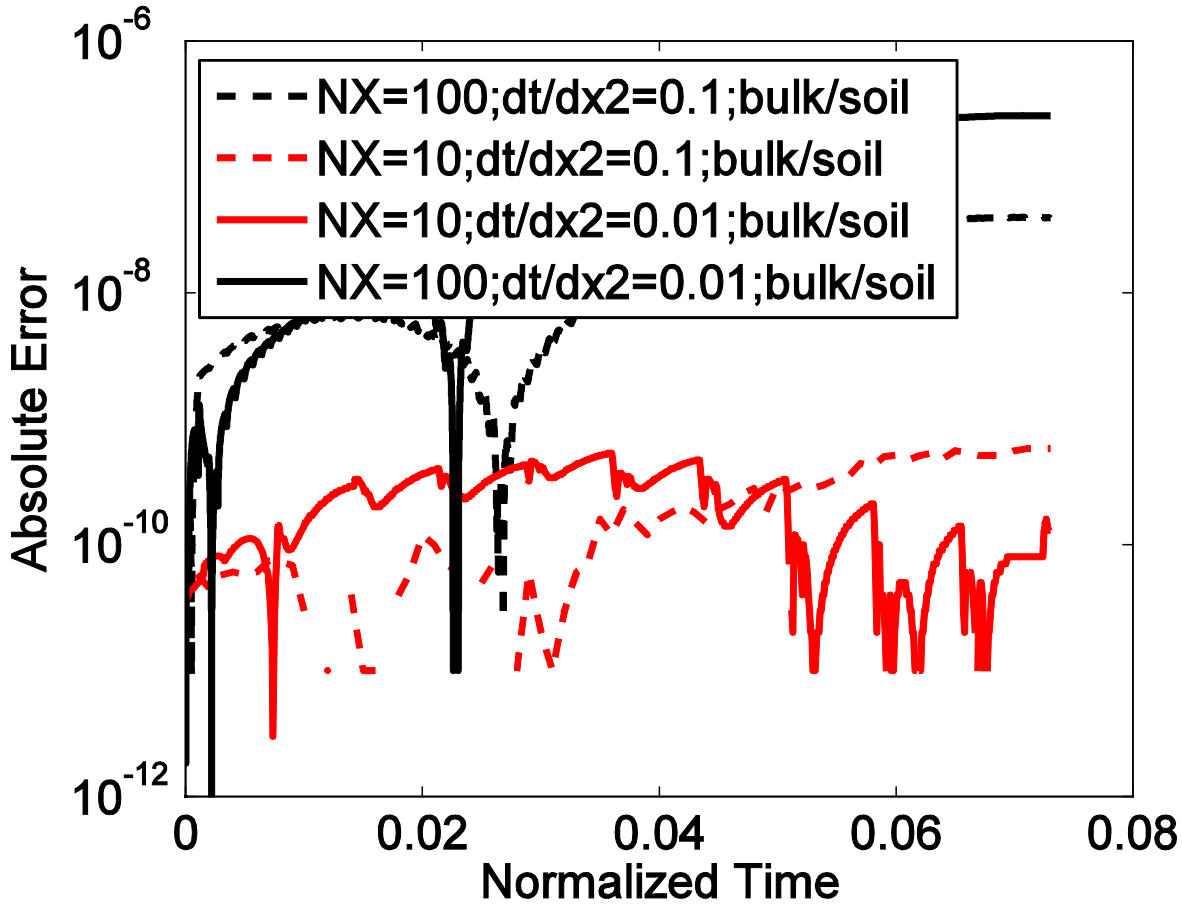

Figure 5.104 Absolute error history

5.2.4 Numerical results

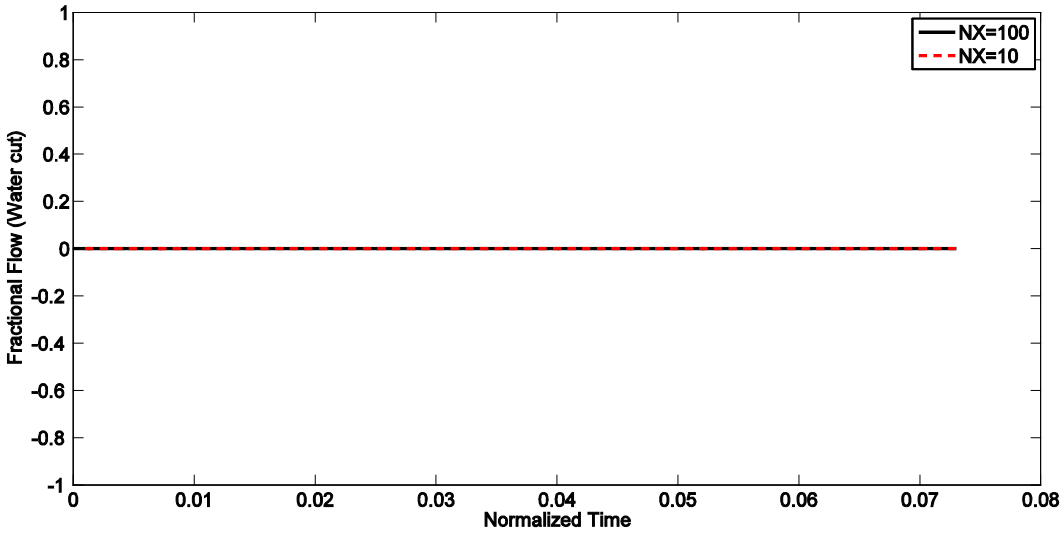

Figure 5.105 Fractional flow history

Since I neglect the capillary pressure end effect, the fractional flow (water cut) history is keeping at zero. The velocity of water as the invading phase is zero at the outlet until water flows to the outlet finally (Figure 5.105).

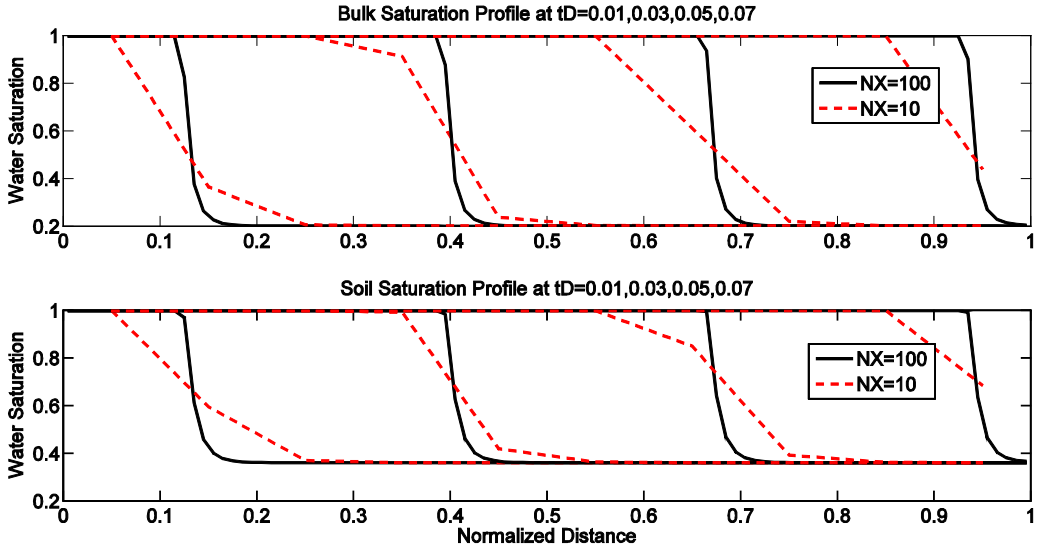

Figure 5.106 Water saturation profile

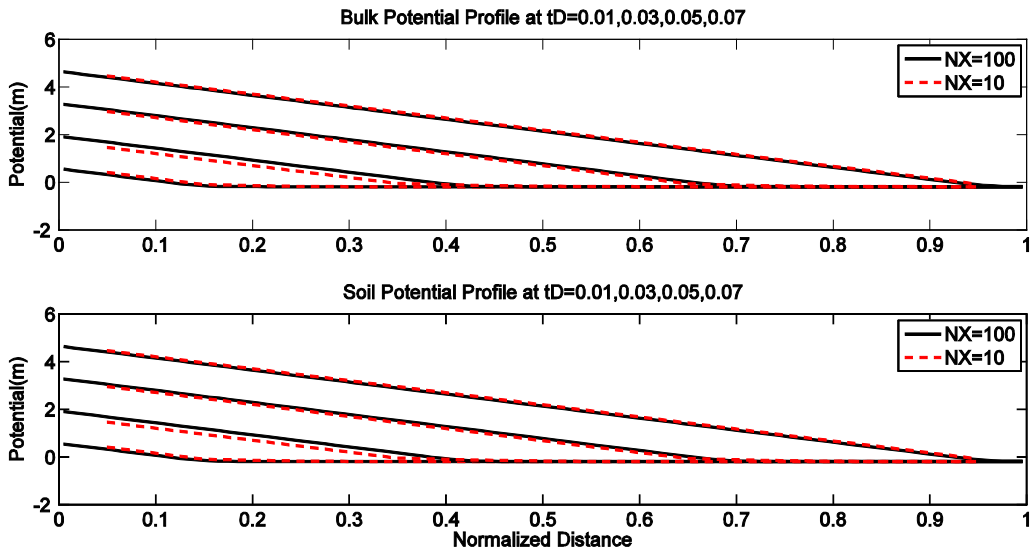

Figure 5.107 Water potential profile

Both the water saturation and potential profile for bulk and soil phase is almost the same (Figure (5.106-5.107)). The reason is that the capillary pressure functions (equation 5.101) I am using do not give a huge pressure difference among biochar, bulk and soil pahses. Using NX=100 causes lots of computational time, but it provides better water wave front. Instead for NX=10, the wavefront is smear out due to numerical dispersion.

It is also interesting to compare the time scale between Chapter 5.1 the nutrient ions mass transfer models and Chapter 5.2 the water fluid mechanics models. The time for water to saturate the whole column is 90s, which is much smaller than that for hours time scale of water flush and nutrients mass transfer from the numerical results I obtained in Chapter 5.1 and 5.2,. Therefore, the assumption we made in Chapter 5.1 that the nutrient mass transfer can be regarded to start after the column is fully saturated with nutrients is valid.

CHAPTER 6

Conclusions and recommendations for the future work

6.1 Conclusions

We report results characterizing the chemical and pore structure of biochars produced from two biomass feedstocks (corn stover or apple wood) using different pyrolysis protocols with two final heat treatment temperatures (450 or 600°C) and exposure times to the final temperature (0 or 60 min), two particle diameters (1.5 mm or 0.25 mm), and two pyrolysis heating rates (0.1 or 1°C/s). All biochars were produced under flowing nitrogen in a computer-controlled fixed bed reactor that allowed us to accurately program the temperature of pyrolyzing biomass samples. While several studies quantifying the effect of pyrolysis conditions on the structure of biochars have appeared in the literature, this is the first study, to our knowledge, to simultaneously test the effects of all these operating conditions using biochars produced under well-defined and highly reproducible temperature protocols. Our main conclusions are:

1. In agreement with earlier literature studies, we found that the biomass feedstock and the final heat treatment temperature (HTT) are major controls on biochar properties. For both wood and grass feedstocks, higher HTT values lead to biochars with higher C/H ratios, larger clusters of aromatic rings, and larger micropore volumes or micropore surface areas.
2. Particle size, pyrolysis heating rate and the duration of the pyrolysis reaction also have significant effects on the chemical composition, aromaticity and pore structure of biochars. Moreover, the pyrolysis conditions did not always have the same effect on the properties of biochars produced from corn stover or apple wood. For both feedstocks, the size of aromatic ring clusters and the microporosity increased with decreasing particle size. However, a slower heating rate led to larger aromatic ring clusters and larger microporosities for apple

wood biochars, while the opposite effect of heating rate was observed for biochars produced from corn stover.

3. Our results reveal that the chemical and pore structure of biochars are controlled by a complex interplay between the pyrolysis conditions and the chemistry of the original biomass feedstock that determines the reaction kinetics. Clearly, detailed pyrolysis protocols must be defined and followed in order to produce biochars with specific and reproducible chemical and physical properties. Our results also underscore the difficulties in comparing results from literature studies that use different reactors and operating conditions, even when these studies use the same feedstocks and final heat treatment temperatures.
4. We demonstrate how thermogravimetric data and pore structure models can be used to probe the multiscale pore structure of biochars. This approach has the potential to overcome some of the major challenges encountered in characterizing the complex pore structure of biochars. We are currently working on extending the pore models available in the literature so that they can incorporate all the available information about the multiple interconnected networks and the spatial distribution of the micropores, mesopores and macropores present in biochars.
5. The temperature history of biomass particles will deviate from the temperature program of the reactor (that is the temperature of the particle surroundings). Integration of the material and energy balances yields the temperature lags when biomass particles of different sizes are heated to 600 °C at two different heating rates. Even though the temperature lags of small particles will diminish as the heating rate slows down, large particle sizes can exhibit significant temperature lags even when heated at low heating rates. The main conclusion of our study is that the final chemical and pore structure of the biochar produced depends upon the complete temperature history $T_p(t)\Big|_0^{t_f}$ of the biomass particles, from t=0 when heating

begins until the final time t_f when the particle temperature has cooled down again and all reactions have stopped. As previously mentioned, size can affect the temperature history of pyrolyzing biomass particles. This is true not only for fast heating rates [143], but also for slow heating rates when large particles are used.

6. Biochars have polydisperse pore structure that complicates the analysis of intraparticle diffusion, adsorption/desorption and, in general, their interactions with soil ecosystems. Theoretical models can provide a valuable tool for engineering biochars with optimal environmental properties. Simulations can help us tune key properties of biochar and soil/biochar mixtures in order to maximize solute loadings or optimize the dynamics of adsorption/desorption processes. These properties include biochar loadings, porosities and particle sizes, as well as the chemical characteristics of biochars that will determine the solute equilibrium isotherms.

6.2 Recommendations for the future work

In this study, we have demonstrated the correlation between the biomass pyrolysis process conditions and biochar physical and chemical properties. However, the experiments were primarily conducted under pure N_2 conditions. In next steps, we will pyrolyze the biomass under 1% O_2-99% N_2 conditions. Instead of slowly oxidized by soil amendment using fresh biochar, partially-oxidized biochar has higher nutrients adsorption capacity and water holding capacity. I have performed several runs of static NH_4NO_3 adsorption on freshly made biochar in batch, there is negligible adsorption. Necessary oxidiation will become a vital step before running any adsorption experiments in the future.

We are also preparing the dynamic adsorption experiments of ammonium in columns packed with soil/biochar mixtures to determine the adsorption isotherms and kinetics (Figure 6.1). We will change the column parameters, such as flow rate, aqueous ammonium concentration to see the effects. We will use the established models to tune key biochar and column properties (like biochar loadings, porosities, particle sizes, or solute equilibrium isotherms) in order to maximize solute loadings in the column. We will determine the established key model parameters by comparing experimental breakthrough curves with model predicted ones.

Similarily, I am extending models for the water horizationlly flow through biochar/soil mixture porous media to vertical gravity drainage and imbibition. Biochar/soil hydraulic conductivities and capillary pressure curves will be obtained through experimental measurements.

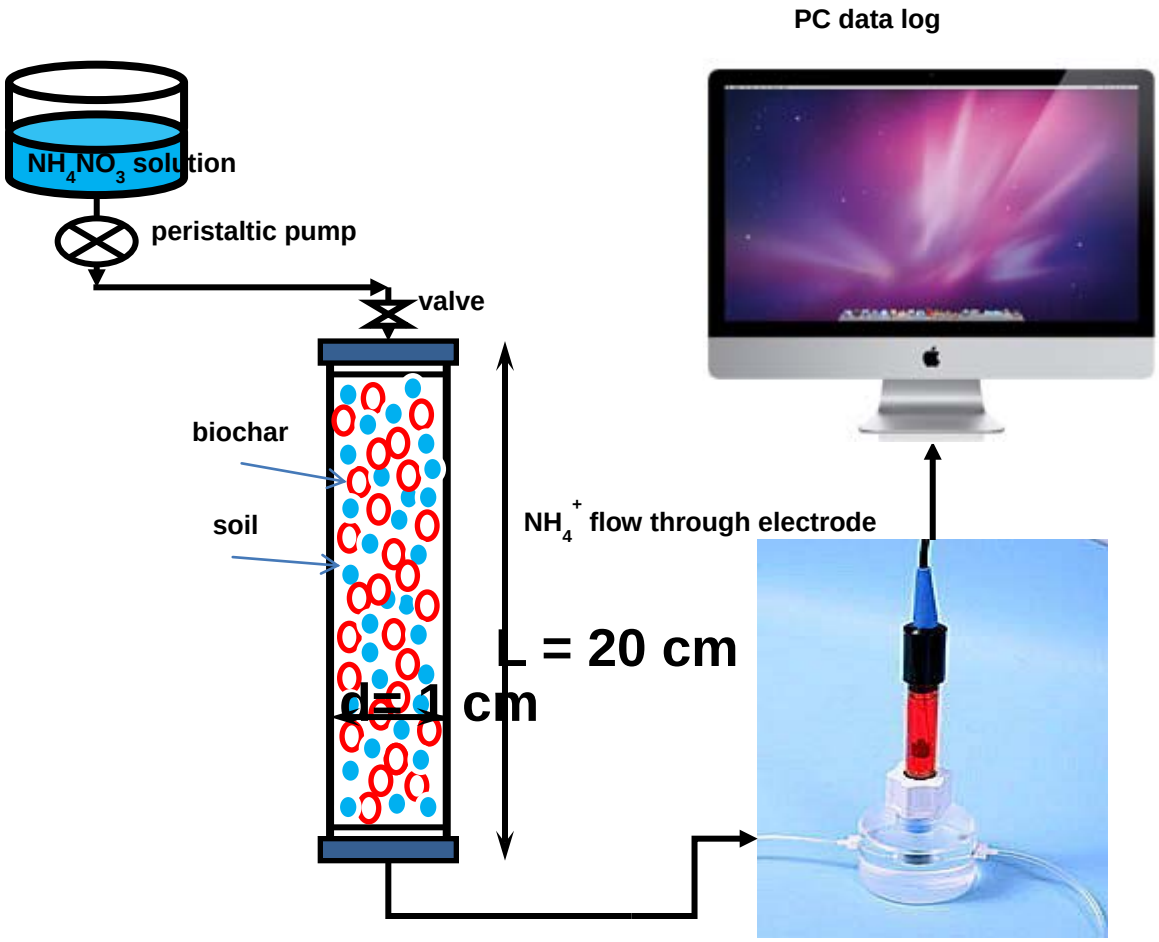

Figure 6.1 Experimental setup used for ammonium transport study

References

1. *Carbon Dioxide Information Analysis Center*. 2012 http://cdiac.ornl.gov/.

2. Pacala, S. and R. Socolow, *Stabilization wedges: Solving the climate problem for the next 50 years with current technologies.* Science, 2004. **305**(5686): p. 968-972.

3. Trumbore, S., *Radiocarbon and Soil Carbon Dynamics.* Annual Review of Earth and Planetary Sciences, 2009. **37**: p. 47-66.

4. Lehmann, J., J. Gaunt, and M. Rondon, *Bio-char sequestration in terrestrial ecosystems: A review.* Mitigation and adaptation strategies for global change, 2006. **11**(2): p. 395-419.

5. Molina, M., et al., *Reducing abrupt climate change risk using the Montreal Protocol and other regulatory actions to complement cuts in CO2 emissions.* Proc Natl Acad Sci U S A, 2009. **106**(49): p. 20616-21.

6. Lehmann, J., *A handful of carbon.* Nature, 2007. **447**(7141): p. 143-144.

7. Czimczik, C.I. and C.A. Masiello, *Controls on black carbon storage in soils.* Global Biogeochemical Cycles, 2007. **21**(3): p. 8.

8. Masiello, C.A., *New directions in black carbon organic geochemistry.* Marine Chemistry, 2004. **92**(1-4): p. 201-213.

9. Neves, E.G., et al., *Timing of Terra Preta Formation in Central Amazon: New Data from Three Sites in the Central Amazon*, in *Amazonian Dark Earths: Explorations in Space and Time*, B. Glaser and W.I. Woods, Editors. 2004, Springer.

10. Glaser, B., et al., *The' Terra Preta' phenomenon: a model for sustainable agriculture in the humid tropics.* Naturwissenschaften, 2001. **88**(1): p. 37-41.

11. Erickson, C., *Historical ecology and future explorations*, in *Amazonian Dark Earths: Origin, properties and Management*, J. Lehmann, Editor. 2003, Kluwer Academic Publishers: Dordrecht; Boston. p. 455-500.

12. Woolf, D., et al., *Sustainable biochar to mitigate global climate change.* Nature Communications, 2010. **1**: p. -.

13. Woolf, D., et al., *Sustainable biochar to mitigate global climate change.* Nature Communications, 2010. **1**(5): p. 1-9.

14. Glaser, B., J. Lehmann, and W. Zech, *Ameliorating physical and chemical properties of highly weathered soils in the tropics with charcoal - a review.* Biology and Fertility of Soils, 2002. **35**(4): p. 219-230.

15. Kinney, T.J., et al., *Hydrologic Properties of Biochars Produced at Different Temperatures.* Environmental Progress and Sustainable Energy 2012. **(in preparation)**.

16. Lehmann, J., J. Kinyangi, and D. Solomon, *Organic matter stabilization in soil microaggregates: implications from spatial heterogeneity of organic carbon contents and carbon forms.* Biogeochemistry, 2007. **85**(1): p. 45-57.

17. Steiner, C., et al., *Nitrogen retention and plant uptake on a highly weathered central Amazonian Ferralsol amended with compost and charcoal.* Journal of Plant Nutrition and Soil Science-Zeitschrift Fur Pflanzenernahrung Und Bodenkunde, 2008. **171**(6): p. 893-899.

18. Chan, K.Y., et al., *Agronomic values of greenwaste biochar as a soil amendment.* Australian Journal of Soil Research, 2007. **45**(8): p. 629-634.

19. Chan, K.Y., et al., *Using poultry litter biochars as soil amendments.* Australian Journal of Soil Research, 2008. **46**(5): p. 437-444.

20. Major, J., et al., *Maize yield and nutrition during 4 years after biochar application to a Colombian savanna oxisol.* Plant and Soil, 2010. **333**(1-2): p. 117-128.

21. Hossain, M.K., et al., *Agronomic properties of wastewater sludge biochar and bioavailability of metals in production of cherry tomato (Lycopersicon esculentum).* Chemosphere, 2010. **78**(9): p. 1167-1171.

22. Beesley, L., E. Moreno-JimÃ©nez, and J.L. Gomez-Eyles, *Effects of biochar and greenwaste compost amendments on mobility, bioavailability and toxicity of inorganic and organic contaminants in a multi-element polluted soil.* Environmental Pollution. **158**(6): p. 2282-2287.

23. Wardle, D.A., M.C. Nilsson, and O. Zackrisson, *Fire-derived charcoal causes loss of forest humus.* Science, 2008. **320**(5876): p. 629-629.

24. Zimmerman, A.R., B. Gao, and M.Y. Ahn, *Positive and negative carbon mineralization priming effects among a variety of biochar-amended soils.* Soil Biology & Biochemistry, 2011. **43**(6): p. 1169-1179.

25. Jones, D.L., et al., *Short-term biochar-induced increase in soil CO(2) release is both biotically and abiotically mediated.* Soil Biology & Biochemistry, 2011. **43**(8): p. 1723-1731.

26. Li, D., et al., *Earthworm avoidance of biochar can be mitigated by wetting.* Soil Biology & Biochemistry, 2011. **43**(8): p. 1732-1737.

27. Lehmann, J., et al., *Biochar effects on soil biota - A review.* Soil Biology & Biochemistry, 2011. **43**(9): p. 1812-1836.

28. Bell, M.J. and F. Worrall, *Charcoal addition to soils in NE England: A carbon sink with environmental co-benefits?* Science of the Total Environment, 2011. **409**(9): p. 1704-1714.

29. Gaskin, J.W., et al., *Effect of Peanut Hull and Pine Chip Biochar on Soil Nutrients, Corn Nutrient Status, and Yield.* Agronomy Journal, 2010. **102**(2): p. 623-633.

30. Czernik, S. and A.V. Bridgwater, *Overview of applications of biomass fast pyrolysis oil.* Energy & Fuels, 2004. **18**(2): p. 590-598.

31. Zhang, X., et al., *Study on biomass pyrolysis kinetics.* Journal of engineering for gas turbines and power, 2006. **128**: p. 493.

32. Demirbas, A., *Effects of temperature and particle size on bio-char yield from pyrolysis of agricultural residues.* Journal of analytical and applied pyrolysis, 2004. **72**(2): p. 243-248.

33. Lehmann, J., *Bio-energy in the black.* Frontiers in Ecology and the Environment, 2007. **5**(7): p. 381-387.

34. Yanik, J., et al., *Fast pyrolysis of agricultural wastes: Characterization of pyrolysis products.* Fuel Processing Technology, 2007. **88**(10): p. 942-947.

35. Yanik, J., et al., *Fast pyrolysis of agricultural wastes: Characterization of pyrolysis products.* Fuel Processing Technology, 2007. **88**(10): p. 942-947.

36. Scott, D.S., et al., *The role of temperature in the fast pyrolysis of cellulose and wood.* Industrial & Engineering Chemistry Research, 1988. **27**(1): p. 8-15.

37. Boateng, A.A., *Characterization and thermal conversion of charcoal derived from fluidized-bed fast pyrolysis oil production of switchgrass.* Industrial & Engineering Chemistry Research, 2007. **46**(26): p. 8857-8862.

38. Karhu, K., et al., *Biochar addition to agricultural soil increased CH4 uptake and water holding capacity – Results from a short-term pilot field study.* Agriculture, Ecosystems and Environment, 2011. **140**: p. 309-313.

39. Karaosmanoglu, F., A. Isigigarergadenler, and A. Sever, *Biochar from the straw-stalk of rapeseed plant.* Energy & Fuels, 2000. **14**(2): p. 336-339.

40. Baldock, J.A. and R.J. Smernik, *Chemical composition and bioavailability of thermally altered Pinus resinosa (Red pine) wood.* Organic Geochemistry, 2002. **33**(9): p. 1093-1109.

41. Di Blasi, C., et al., *Product distribution from pyrolysis of wood and agricultural residues.* Industrial and Engineering Chemistry Research, 1999. **38**: p. 2216-2224.

42. Preston, C.M. and M.W.I. Schmidt, *Black (pyrogenic) carbon: a synthesis of current knowledge and uncertainties with special consideration of boreal regions.* Biogeosciences, 2006. **3**(4): p. 397-420.

43. Knicker, H., et al., *Condensation degree of burnt peat and plant residues and the reliability of solid-state VACP MAS 13C NMR spectra obtained from pyrogenic humic material.* Organic Geochemistry, 2005. **36**(10): p. 1359-1377.

44. Czimczik, C.I., et al., *Effects of charring on mass, organic carbon, and stable carbon isotope composition of wood.* Organic Geochemistry, 2002. **33**(11): p. 1207-1223.

45. Knicker, H., et al., *A new conceptual model for the structural properties of char produced during vegetation fires.* Organic Geochemistry, 2008. **39**(8): p. 935-939.

46. Antal, M.J., *Effects of reactor severity on the gas-phase pyrolysis of cellulose- and kraft lignin-derived volatile matter*. Industrial & Engineering Chemistry Product Research and Development, 1983. **22**(2): p. 366-375.

47. Mok, W.S.L., et al., *Formation of charcoal from biomass in a sealed reactor.* Industrial & Engineering Chemistry Research, 1992. **31**(4): p. 1162-1166.

48. Raveendran, K., A. Ganesh, and K.C. Khilar, *Pyrolysis characteristics of biomass and biomass components.* Fuel, 1996. **75**(8): p. 987-998.

49. Antal Jr, M.J., et al., *Attainment of the theoretical yield of carbon from biomass.* Ind. Eng. Chem. Res, 2000. **39**(11): p. 4024-4031.

50. Antal, M.J. and M. Grønli, *The Art, Science, and Technology of Charcoal Production†*. Industrial & Engineering Chemistry Research, 2003. **42**(8): p. 1619-1640.

51. Michael, J.A., Eric, C., Xiangfeng Dai,et. al, *High-Yield Biomass Bio-char*. Energy & Fuels, 1996. **19**(652-658).

52. Xiaodong Zhang, M.X., Rongfeng Sun,et. al, *Study on Biomass Pyrolysis Kinetics.* Journal of Engineering for Gas Turbines and Power, 2006. **128**: p. 493-496.

53. A.E. Putun, O.M.K., S. Yorgun, et.al, *Fuel Process.* Technol, 1996. **46**: p. 49.

54. S. Senso¨z, D.A., S. Yorgun, *Biomass Bioenergy.* 2000. **19**: p. 271.

55. Funazukuri, T., Hudgins,R.R.,Silveston,P.L., J. Anal. Appl. Pyrolysis, 1986. **9**(139).

56. Haykiri-Acma, H., *The role of particle size in the non-isothermal pyrolysis of hazelnut shell.* Journal of analytical and applied pyrolysis, 2006. **75**(2): p. 211-216.

57. Zanzi, R., K. Sjostrom, and E. Bjornbom, *Rapid pyrolysis of agricultural residues at high temperature.* Biomass and Bioenergy, 2002. **23**(5): p. 357-366.

58. Glaser, B., et al., *Black carbon in density fractions of anthropogenic soils of the Brazilian Amazon region.* Organic Geochemistry, 2000. **31**(7-8): p. 669-678.

59. Bourke, J., et al., *Do All Carbonized Charcoals Have the Same Chemical Structure? 2. A Model of the Chemical Structure of Carbonized Charcoal†*. Industrial & Engineering Chemistry Research, 2007. **46**(18): p. 5954-5967.

60. Mészáros, E., et al., *Do All Carbonized Charcoals Have the Same Chemical Structure? 1. Implications of Thermogravimetry−Mass Spectrometry Measurements.* Ind. Eng. Chem. Res., 2007. **46**(18): p. 5943-5953.

61. Keiluweit, M., et al., *Dynamic Molecular Structure of Plant Biomass-Derived Black Carbon (Biochar).* Environmental Science & Technology, 2010. **44**: p. 1247-1253.

62. Uchimiya, M., et al., *Influence of Pyrolysis Temperature on Biochar Property and Function as a Heavy Metal Sorbent in Soil.* Journal of Agricultural and Food Chemistry, 2011. **59**(6): p. 2501-2510.

63. McBeath, A.V. and R.J. Smernik, *Variation in the degree of aromatic condensation of chars.* Organic Geochemistry, 2009. **40**(12): p. 1161-1168.

64. Brewer, C.E., et al., *Characterization of biochar from fast pyrolysis and gasification systems.* Environmental Progress & Sustainable Energy, 2009. **28**(3): p. 386-396.

65. Laird, D.A., et al., *Review of the pyrolysis platform for coproducing bio-oil and biochar.* Biofuels Bioproducts & Biorefining-Biofpr, 2009. **3**(5): p. 547-562.

66. Aguado, R., et al., *Pyrolysis of sawdust in a conical spouted bed reactor. Yields and product composition.* Ind. Eng. Chem. Res, 2000. **39**(6): p. 1925-1933.

67. Aguado, R., et al., *Char formation kinetics in the pyrolysis of sawdust in a conical spouted bed reactor.* Journal of Chemical Technology & Biotechnology, 2000. **75**(7): p. 583-588.

68. Guerrero, M., et al., *Pyrolysis of eucalyptus at different heating rates: studies of char characterization and oxidative reactivity.* Journal of analytical and applied pyrolysis, 2005. **74**(1-2): p. 307-314.

69. Daud, W.M.A.W., W.S.W. Ali, and M.Z. Sulaiman, *Effect of carbonization temperature on the yield and porosity of char produced from palm shell.* Journal of Chemical Technology & Biotechnology, 2001. **76**(12): p. 1281-1285.

70. Bird, M.I., et al., *X-ray microtomographic imaging of charcoal.* Journal of Archaeological Science, 2008. **35**(10): p. 2698-2706.

71. Laine, J. and S. Yunes, *Effect of the preparation method on the pore size distribution of activated carbon from coconut shell.* Carbon, 1992. **30**(4): p. 601-604.

72. Lamond, T. and H. Marsh, *The surface properties of carbon-II the effect of capillary condensation at low relative pressures upon the determination of surface area* Carbon, 1964. **1**(3): p. 281-292.

73. Nguyen, B.T., et al., *Temperature Sensitivity of Black Carbon Decomposition and Oxidation.* Environmental Science & Technology, 2010. **44**(9): p. 3324-3331.

74. Wildman, J. and F. Derbyshire, *Origins and functions of macroporosity in activated carbons from coal and wood precursors.* Fuel, 1991. **70**(5): p. 655-661.

75. Dubinin, M., *Fundamentals of the theory of adsorption in micropores of carbon adsorbents: characteristics of their adsorption properties and microporous structures.* Carbon, 1989. **27**(3): p. 457-467.

76. Gregg, S.J. and K.S.W. Sing, *Adsorption, surface area, and porosity*. 1983, New York, NY: Academic Press.

77. Sing, K.S.W., et al., *Reporting Physisorption Data for Gas/Solid Systems with Special Reference to the Determination of Surface Area and Porosity.* Pure and Applied Chemistry, 1985. **57**(4): p. 603-619.

78. Zygourakis, K. and C.W. Sandmann, *Discrete Structural Models and Their Application to Gas-Solid Reacting Systems.* Aiche Journal, 1988. **34**(12): p. 2030-2040.

79. Fu, P., et al., *Pyrolysis of Maize Stalk on the Characterization of Chars Formed under Different Devolatilization Conditions.* Energy Fuels, 2009. **23**(9): p. 4605-4611.

80. Haghseresht, F., G.Q. Lu, and A.K. Whittaker, *Carbon structure and porosity of carbonaceous adsorbents in relation to their adsorption properties.* Carbon, 1999. **37**(9): p. 1491-1497.

81. Cao, N., et al., *Thermogravimetric study on the steam activation of charcoals obtained by vacuum and atmospheric pyrolysis of softwood bark residues.* Carbon, 2002. **40**(4): p. 471-479.

82. Ehrburger-Dolle, F., A. Lavanchy, and F. Stoeckli, *Determination of the surface fractal dimension of active carbons by mercury porosimetry.* Journal of Colloid and Interface Science, 1994. **166**(2): p. 451-461.

83. Jones, A.C., et al., *The correlation of pore morphology, interconnectivity and physical properties of 3D ceramic scaffolds with bone ingrowth.* Biomaterials, 2009. **30**(7): p. 1440-1451.

84. Hou, L., et al., *Imaging the microstructure of low rank coals: A study combining nuclear magnetic resonance, scanning electron and optical microscopic imaging.* Fuel, 1994. **73**(2): p. 199-203.

85. Tryon, E.H., *Effect of Charcoal on Certain Physical, Chemical, and Biological Properties of Forest Soils.* Ecological Monographs, 1948. **18**(1): p. 81-115.

86. Brockhoff, S.R., et al., *Physical and Mineral-Nutrition Properties of Sand-Based Turfgrass Root Zones Amended with Biochar.* Agronomy Journal, 2010. **102**(6): p. 1627-1631.

87. Piccolo, A., G. Pietramellara, and J.S.C. Mbagwu, *Effects of coal derived humic substances on water retention and structural stability of Mediterranean soils.* Soil Use and Management, 1996. **12**(4): p. 209-213.

88. Pietikainen, J., O. Kiikkila, and H. Fritze, *Charcoal as a habitat for microbes and its effect on the microbial community of the underlying humus.* Oikos, 2000. **89**(231-242).

89. Renck, A. and J. Lehmann, *Rapid water flow and transport of inorganic and organic nitrogen in a highly aggregated tropical soil.* Soil Science, 2004. **169**(5): p. 330-341.

90. Steiner, C., et al., *Long term effects of manure, charcoal and mineral fertilization on crop production and fertility on a highly weathered Central Amazonian upland soil.* Plant and Soil, 2007. **291**(1-2): p. 275-290.

91. Downie, A., A. Crosky, and P. Munroe, *Physical Properties of Biochar,* in *Biochar for Environmental Management: Science and Technology*, J. Lehman and S. Joseph, Editors. 2009, Earthscan: London, UK. p. 13-32.

92. Saito, M., *Charcoal as a Micro-habitat for VA Mycorrhizal Fungi and its practical implication.* Agriculture, Ecosystems and Environment,, 1989. **29**: p. 341-344.

93. Saito, M. and T. Marumoto, *Inoculation with arbuscular mycorrhizal fungi: the status quo in Japan and the future prospects.* Plant and Soil, 2002. **244**(1-2): p. 273-279.

94. Warnock, D.D., et al., *Mycorrhizal responses to biochar in soil - concepts and mechanisms.* Plant and Soil, 2007. **300**(1-2): p. 9-20.

95. Warnock, D.D., et al., *Influences of non-herbaceous biochar on arbuscular mycorrhizal fungal abundances in roots and soils: Results from growth-chamber and field experiments.* Applied Soil Ecology, 2010. **46**(3): p. 450-456.

96. Liang, B., et al., *Black Carbon increases cation exchange capacity in soils.* Soil Science Society of America Journal, 2006. **70**(5): p. 1719-1730.

97. Lehmann, J., et al., *Nutrient availability and leaching in an archaeological Anthrosol and a Ferralsol of the Central Amazon basin: fertilizer, manure and charcoal amendments.* Plant and Soil, 2003. **249**(2): p. 343-357.

98. Cheng, C.H., et al., *Oxidation of black carbon by biotic and abiotic processes.* Organic Geochemistry, 2006. **37**(11): p. 1477-1488.

99. Burkart, M.R. and D.E. James, *Agricultural-nitrogen contributions to hypoxia in the Gulf of Mexico.* Journal of Environmental Quality, 1999. **28**(3): p. 850-859.

100. Carpenter, S.R., et al., *Nonpoint pollution of surface waters with phosphorus and nitrogen.* Ecological Applications, 1998. **8**(3): p. 559-568.

101. Wang, J.J. and D.L. Harrell, *Effect of ammonium, potassium, and sodium cations and phosphate, nitrate, and chloride anions on zinc sorption and lability in selected acid and calcareous soils.* Soil Science Society of America Journal, 2005. **69**(4): p. 1036.

102.Liu, Y., et al., *Long-Term Fertilization Influences on Clay Mineral Composition and Ammonium Adsorption in a Rice Paddy Soil.* Soil Science Society of America Journal, 2008. **72**(6): p. 1580.

103.Singh, B., B.P. Singh, and A.L. Cowie, *Characterisation and evaluation of biochars for their application as a soil amendment.* Australian Journal of Soil Research, 2010. **48**(7): p. 516-525.

104.Van Zwieten, L., et al., *Effects of biochar from slow pyrolysis of papermill waste on agronomic performance and soil fertility.* Plant and Soil, 2010. **327**(1): p. 235-246.

105.Nguyen, B.T. and J. Lehmann, *Black carbon decomposition under varying water regimes.* Organic Geochemistry, 2009. **40**(8): p. 846-853.

106.Novak, J.M., et al., *Impact of biochar amendment on fertility of a southeastern coastal plain soil.* Soil Science, 2009. **174**(2): p. 105.

107.Gaskin, J.W., et al., *Effect of low-temperature pyrolysis conditions on biochar for agricultural use.* Transactions of the Asabe, 2008. **51**(6): p. 2061-2069.

108.Aris, R., *The mathematical theory of diffusion and reaction in permeable catalysts: The theory of the steady state*. Vol. 1. 1975, London, UK: Clarendon Press - Oxford.

109.Ballal, G. and K. Zygourakis, *Evolution of Pore Surface-Area during Noncatalytic Gas Solid Reactions .1. Model Development.* Industrial & Engineering Chemistry Research, 1987. **26**(5): p. 911-921.

110.Sotirchos, S.V., *On a Class of Random Pore and Grain Models for Gas Solid Reactions.* Chemical Engineering Science, 1987. **42**(5): p. 1262-1265.

111.Sahimi, M., G.R. Gavalas, and T.T. Tsotsis, *Statistical and continuum models of fluid-solid reactions in porous media.* Chemical Engineering Science, 1990. **45**(6): p. 1443-1502.

112.Jellali, S., et al., *Dynamic sorption of ammonium by sandy soil in fixed bed columns: Evaluation of equilibrium and non-equilibrium transport processes.* Journal of environmental management, 2010. **91**(4): p. 897-905.

113.Touma, J. and M. Vauclin, *Experimental and numerical analysis of two-phase infiltration in a partially saturated soil.* Transport in Porous Media, 1986. **1**(1): p. 27-55.

114.Celia, M.A. and P. Binning, *A mass conservative numerical solution for two-phase flow in porous media with application to unsaturated flow.* Water Resources Research, 1992. **28**(10): p. 2819-2828.

115.Gwo, J.P., et al., *A multiple-pore-region concept to modeling mass transfer in subsurface media.* Journal of Hydrology, 1995. **164**(1-4): p. 217-237.

116.Gerke, H.H. and M.T. Van Genuchten, *A dual-porosity model for simulating the preferential movement of water and solutes in structured porous media.* Water Resources Research, 1993. **29**: p. 305-305.

117.Gwo, J.P., et al., *Using a multiregion model to study the effects of advective and diffusive mass transfer on local physical nonequilibrium and solute mobility in a structured soil.* Water Resources Research, 1996. **32**(3): p. 561-570.

118.Zygourakis, K. and M.W. Glass, *Macropore Size Analysis Using Digital Image-Processing and a Stereological Model.* Chemical Engineering Communications, 1988. **70**: p. 39-55.

119.Cai, Y., *The Effects of Process Conditions on Char Reactivity: Experimental Studies and Mathematical Modeling*, in *Chemical Engineering*. 2001, Rice University: Houston.

120.Glass, M.W. and Kyriacos Zygourakis, *Computerized microreactor and video microscopy system for coal pyrolysis studies.* Rev. Sci. Instrum., 1988. **59**(4): p. 580-587.

121.Bequette, B.W., *Process control: modeling, design, and simulation*. 2003: Prentice Hall.

122.Botto, R.E., *Optimization of sensitivity in pulsed ^{13}C NMR of coals.* Energy Fuels, 2002. **16**(4): p. 925-927.

123.Smernik, R.J. and J.M. Oades, *Background Signal in Solid State ^{13}C NMR Spectra of Soil Organic Matter (SOM)--Quantification and Minimization.* Solid State Nuclear Magnetic Resonance, 2001. **20**(1-2): p. 74-84.

124.Solum, M.S., R.J. Pugmire, and D.M. Grant, *^{13}C solid-state NMR of argonne premium coals.* Energy & Fuels, 1989. **3**(2): p. 187-193.

125.Baldock, J.A., et al., *Cycling and composition of organic matter in terrestrial and marine ecosystems.* Marine Chemistry, 2004. **92**(1-4): p. 39-64.

126.Mao, J.D. and K. Schmidt-Rohr, *Accurate quantification of aromaticity and nonprotonated aromatic carbon fraction in natural organic matter by 13C solid-state nuclear magnetic resonance.* Environ. Sci. Technol, 2004. **38**(9): p. 2680-2684.

127.Ishimaru, K., et al., *Spectroscopic analysis of carbonization behavior of wood, cellulose and lignin.* Journal of Materials Science, 2007. **42**(1): p. 122-129.

128.Bourke, J., et al., *Do All Carbonized Charcoals Have the Same Chemical Structure? 2. A Model of the Chemical Structure of Carbonized Charcoal?* Ind. Eng. Chem. Res, 2007. **46**(18): p. 5954-5967.

129.Naizhen Cao, e.a., *Thermogravimetric study on the steam activation of bio-chars obtained by vacuum and atmospheric pyrolysis of softwood bark residues.* Carbon, 2002. **40**: p. 471-479.

130.de Boor, C., *A Practical Guide to Splines*. Applied Mathematical Sciences. 1978, New York, NY: Springer-Verlag.

131.Di Blasi, C., *Modeling chemical and physical processes of wood and biomass pyrolysis.* Progress in Energy and Combustion Science, 2008. **34**(1): p. 47-90.

132.Antal, M.J.J. and G. Varhegyi, *Cellulose pyrolysis kinetics: the current state of knowledge.* Industrial & Engineering Chemistry Research, 1995. **34**(3): p. 703-717.

133.Scott, S.A., et al., *Thermogravimetric measurements of the kinetics of pyrolysis of dried sewage sludge.* Fuel, 2006. **85**(9): p. 1248-1253.

134.Park, W.C., A. Atreya, and H.R. Baum, *Experimental and theoretical investigation of heat and mass transfer processes during wood pyrolysis.* Combustion and Flame, 2010. **157**(3): p. 481-494.

135.Turner, I., et al., *An experimental and theoretical investigation of the thermal treatment of wood (Fagus sylvatica L.) in the range 200-260° C.* International Journal of Heat and Mass Transfer, 2010. **53**(4): p. 715-725.

136.Ratte, J., et al., *Mathematical modelling of slow pyrolysis of a particle of treated wood waste.* Journal of Hazardous Materials, 2009. **170**(2): p. 1023-1040.

137.Lin, Y.C., et al., *Kinetics and mechanism of cellulose pyrolysis.* The Journal of Physical Chemistry C, 2009. **113**(46): p. 20097-20107.

138.Stenseng, M., A. Jensen, and K. Dam-Johansen, *Investigation of biomass pyrolysis by thermogravimetric analysis and differential scanning calorimetry.* Journal of analytical and applied pyrolysis, 2001. **58**: p. 765-780.

139.Narayan, R. and M.J. Antal, *Thermal Lag, Fusion, and the Compensation Effect during Biomass Pyrolysis†.* Industrial & Engineering Chemistry Research, 1996. **35**(5): p. 1711-1721.

140.Elyounssi, K., J. Blin, and M. Halim, *High-yield charcoal production by two-step pyrolysis.* Journal of analytical and applied pyrolysis, 2010. **87**(1): p. 138-143.

141.Hammes, K., et al., *Characterisation and evaluation of reference materials for black carbon analysis using elemental composition, colour, BET surface area and 13C NMR spectroscopy.* Applied Geochemistry, 2008. **23**(8): p. 2113-2122.

142.Ascough, P.L., et al., *Influence of production variables and starting material on charcoal stable isotopic and molecular characteristics.* Geochimica Et Cosmochimica Acta, 2008. **72**(24): p. 6090-6102.

143.Antal, M.J., G. Várhegyi, and E. Jakab, *Cellulose Pyrolysis Kinetics: Revisited.* Industrial & Engineering Chemistry Research, 1998. **37**(4): p. 1267-1275.

144.Cheng, C.H., J. Lehmann, and M.H. Engelhard, *Natural oxidation of black carbon in soils: Changes in molecular form and surface charge along a climosequence.* Geochimica Et Cosmochimica Acta, 2008. **72**(6): p. 1598-1610.

145.Kercher, A.K. and D.C. Nagle, *Microstructural evolution during charcoal carbonization by X-ray diffraction analysis.* Carbon, 2003. **41**: p. 15-27.

146.Russell, B.P. and M.D. Levan, *Pore size distribution of BPL activated carbon determined by different methods.* Carbon, 1994. **32**(5): p. 845-855.

147.Lua, A.C., T. Yang, and J. Guo, *Effects of pyrolysis conditions on the properties of activated carbons prepared from pistachio-nut shells.* Journal of analytical and applied pyrolysis, 2004. **72**(2): p. 279-287.

148.Liu, H., et al., *Mineral reaction and morphology change during gasification of coal in CO2 at elevated temperatures.* Fuel, 2003. **82**(5): p. 523-530.

149.Clarke, A., et al., *Spreading and Imbibition of Liquid Droplets on Porous Surfaces.* Langmuir, 2002. **18**: p. 2980-2984.

150.Frederick, W.J., Jr. and E.G. Bobalek, *The Dynamics of Chemically Reacting Liquid Drops on Porous Surfaces.* Ind. Eng. Chem. Fundam., 1975. **14**(1): p. 40-46.

151.Cai, Y.W. and K. Zygourakis, *A multiscale transient model for combustion of highly porous chars.* Industrial & Engineering Chemistry Research, 2003. **42**(12): p. 2746-2755.

152.Ballal, G. and K. Zygourakis, *Gasification of Coal Chars with Carbon-Dioxide and Oxygen.* Chemical Engineering Communications, 1986. **49**(1-3): p. 181-195.

153.Martinez, M.L., et al., *Preparation and characteristics of activated carbon from olive stones and walnut shells.* Industrial crops and products, 2006. **23**(1): p. 23-28.

154.Zabaniotou, A., G. Stavropoulos, and V. Skoulou, *Activated carbon from olive kernels in a two-stage process: Industrial improvement.* Bioresource technology, 2008. **99**(2): p. 320-326.

155.Khezami, L., A. Ould-Dris, and R. Capart, *Activated carbon from thermo-compressed wood and other lignocellulosic precursors.* Bioresources, 2007. **2**(2): p. 193-209.

156.Ding, Y., et al., *Evaluation of biochar effects on nitrogen retention and leaching in multi-layered soil columns.* Water, Air, & Soil Pollution. **213**(1): p. 47-55.

157.Xia, K., W.A.R. Fernando, and C.W. Rice, *Sorption and desorption of ammonium from liquid swine waste in soils.* Soil Science Society of America Journal, 2005. **69**(4): p. 1057-1065.

158.Lv, L., et al., *Modeling of the adsorption breakthrough behaviors of Pb2+ in a fixed bed of ETS-10 adsorbent.* Journal of Colloid and Interface Science, 2008. **325**(1): p. 57-63.

159.Ko, D.C.K., J.F. Porter, and G. McKay, *Mass transport model for the fixed bed sorption of metal ions on bone char.* Ind. Eng. Chem. Res, 2003. **42**(14): p. 3458-3469.

160.Dadwhal, M., et al., *Adsorption of arsenic on conditioned layered double hydroxides: column experiments and modeling.* Ind. Eng. Chem. Res, 2009. **48**(4): p. 2076-2084.

161.Latheef, I.M., M.E. Huckman, and R.G. Anthony, *Modeling cesium ion exchange on fixed-bed columns of crystalline silicotitanate granules.* Ind. Eng. Chem. Res, 2000. **39**(5): p. 1356-1363.

162.Liapis, A.I., et al., *"Perfusion chromatography". The effects of intra-particle convective velocity and microsphere size on column performance.* Journal of Chromatography A, 1995. **702**(1-2): p. 45-57.

163.Liapis, A.I. and M.A. McCoy, *Perfusion chromatography: Effect of micropore diffusion on column performance in systems utilizing perfusive adsorbent particles with a bidisperse porous structure.* Journal of Chromatography A, 1994. **660**(1-2): p. 85-96.

164.Li, P., G. Xiu, and A.E. Rodrigues, *Modeling breakthrough and elution curves in fixed bed of inert core adsorbents: analytical and approximate solutions.* Chemical Engineering Science, 2004. **59**(15): p. 3091-3103.

165.Ma, Z., R.D. Whitley, and N.H.L. Wang, *Pore and surface diffusion in multicomponent adsorption and liquid chromatography systems.* AIChE Journal, 1996. **42**(5): p. 1244-1262.

166.Koh, J.H., P.C. Wankat, and N.H.L. Wang, *Pore and surface diffusion and bulk-phase mass transfer in packed and fluidized beds.* Ind. Eng. Chem. Res, 1998. **37**(1): p. 228-239.

167.Roy, S., et al., *Modeling gas flow through microchannels and nanopores.* Journal of applied physics, 2003. **93**: p. 4870.

168.Gilron, J. and A. Soffer, *Knudsen diffusion in microporous carbon membranes with molecular sieving character.* Journal of membrane science, 2002. **209**(2): p. 339-352.

169.Do, D.D., H.D. Do, and I. Prasetyo, *Constant molar flow semi-batch adsorber as a tool to study adsorption kinetics of pure gases and vapours.* Chemical Engineering Science, 2000. **55**(9): p. 1717-1727.

170.Albo, S.E., L.J. Broadbelt, and R.Q. Snurr, *Multiscale modeling of transport and residence times in nanostructured membranes.* Aiche Journal, 2006. **52**(11): p. 3679-3687.

171.Suzuki, M. and J.M. Smith, *Axial dispersion in beds of small particles.* The Chemical Engineering Journal, 1972. **3**: p. 256-264.

172. Lide, D.R., *CRC handbook of chemistry and physics*. 1993: CRC press.

173.Mullin, J.W. and T.P. Cook, *Diffusivity of ammonium dihydrogen phosphate in aqueous solutions.* Journal of Applied Chemistry, 1963. **13**(10): p. 423-429.

174.Mullin, J.W. and M.M. Osman, *Diffusivity, density, viscosity, and refractive index of nickel ammonium sulfate aqueous solutions.* Journal of Chemical and Engineering Data, 1967. **12**(4): p. 516-517.

175. Fogler, H.S., *Elements of chemical reaction engineering*. 1999.

176.Smith, J.M. and H.C. Van Ness, *Chemical engineering kinetics*. Vol. 416. 1970: McGraw-Hill New York.

177.Thibaud, C., *Experimental study and mathematical modeling of sorption and desorption of volatile organic contaminants on soil*, in *Chemical Engineering*. 1993, Texas A&M University: College Station.

178.Finlayson, B.A., *Nonlinear analysis in chemical engineering*. 1980: McGraw-Hill College.

179.Latheef, I.M., *Ion exchange column studies for the selective separation of radionuclides using the hydrous crystalline silicontitanate*, in *chemical engineering*. 1999, Texas A&M University: College Station.

180.Brenan, K.E., et al., *Numerical solution of initial-value problems in differential-algebraic equations*. 1996: Society for Industrial Mathematics.

181.Madras, G., et al., *Modeling of supercritical extraction of organics from solid matrices.* AIChE Journal, 1994. **40**(5): p. 777-785.

182.Thibaud-Erkey, C., et al., *Mathematical modeling of adsorption and desorption of volatile contaminants from soil: influence of isotherm shape on adsorption and desorption profiles.* Environ. Sci. Technol, 1996. **30**(7): p. 2127-2134.

183.Thibaud Catherine, *Experimental study and mathematical modeling of sorption and desorption of volatile organic contaminants on soil*, in *Chemical Engineering*. 1993, Texas A&M University: College Station.

184.Suzuki, M. and J.M. Smith, *Axial dispersion in beds of small particles.* Chem. Eng. J., 1972. **3**: p. 256.

185. Civan, F., *Porous Media Transport Phenomena*: Wiley Online Library.

186. Bear, J., *Dynamics of fluids in porous media*. 1988: Dover publications.

187.Mattax, C. and R. Dalton, *RESERVOIR SIMULATION (includes associated papers 21606 and 21620).* Journal of Petroleum Technology, 1990. **42**(6): p. 692-695.

188.Celia, M.A., E.T. Bouloutas, and R.L. Zarba, *A general mass-conservative numerical solution for the unsaturated flow equation.* Water Resources Research, 1990. **26**(7): p. 1483-1496.

189.Oppe, T.C., W.D. Joubert, and D.R. Kincaid, *NSPCG users' guide, version 1.0: A package for solving large sparse linear systems by various iterative methods*. 1988, Tech. Rep. CNA216, Center for Numerical Analysis, University of Texas at Austin, Austin, TX.